NGU REPORT 2024.011

Hazard and risk assessment of the Skutshorn unstable rock slope above Vangsmjøse (Vang, Innlandet)

GEOLOGY FOR SOCIETY

SINCE 1858

GEOLOGICAL SURVEY OF NORWAY

- NGU -

GEOLOGICAL SURVEY OF NORWAY
- NGU -

NGU REPORT
Geology for society

Geological Survey of Norway
P.O. Box 6315 Torgarden
NO-7491 Trondheim, Norway
Tel. +47 73 90 40 00

Report no.: 2024.011
ISSN: 0800-3416 (print)
ISSN:2387-35150 (digital)
Grading: Open

Title: Hazard and risk assessment of the Skutshorn unstable rock slope above Vangsmjøse (Vang, Innlandet)
Authors: R.L. Hermanns, J. Pullarello, E. Anda, L. Kristensen, K. Indrevær, M. Bredal, B.E. Larsen, P. Snook, J. Bendle, R. Eilertsen, T. Eiken, H. Linge
Client: Norges vassdrags- og energidirektorat
County: Innlandet
Municipality: Vang

Map-sheet name (M=1:250.000):
Map-sheet name (M=1:50.000):
Deposit name and grid-reference:
Numbers of pages:
Price (NOK): 310,-

Map enclosures:
Fieldwork carried out: 2018-2022
Date of report:
Project no.: 333500
Person responsible: Martina Böhme
Keywords: Unstable rock slope, rock slope failure, hazard and risk classification, consequence analysis, displacement wave analysis (tsunami), GNSS, InSAR, ERT, TCN dating

Summary:
Skutshorn is located at an SSE dipping slope north of Vangsmjøse (Vang municipality, Innland county). The unstable rock slope is split into a larger scenario (scenario A) to the east and a smaller scenario (scenario B) to the west, which are separated by a niche of failure related to an earlier rock slope failure. This prehistoric failure had a similar volume to scenario B and the deposit is preserved on the bottom of lake Vangsmjøse.

The unstable rock slope Skutshorn has developed in the hanging wall of an important Caledonian thrust fault, in competent rock of arkose and quartzite composition of the Valdres sparagmite nappe. Both scenarios are marked by well-developed fracture zones outside of which is minimal deformation. The more fragile phyllite of the Vangs nappe, in the footwall of the Caledonian thrust, has only few outcrops and is mostly covered in rock fall scree from the rock slope deformation in the upper nappe. In the phyllite outcrops the rock is strongly cracked, with open fractures several meters wide. However, owing to scree cover, the boundaries of this deformation cannot be accurately mapped.

Scenario A has a well-developed back scarp that separates the main slide body from the surrounding slope with a vertical and horizontal offset. The southeastern flank is free, and the northwestern flank coincides with the back scarp, or is free. A daylighting basal rupture surface was not observed as the foot of the instability is scree covered. The structural geological

configuration of this scenario comprises a well-developed schistosity that dips obliquely out of the slope at ~40 degrees in the upper part of the slide mass. In the central part the schistosity dips more steeply and is more parallel to the slope. In the lower part the schistosity is more folded and almost vertical. A total of six joint sets were mapped; five of them are vertical or sub-vertical and the last dips into the slope. Based on these data, planar and wedge sliding is possible in the upper and central part of the slide mass, but not at the foot. Toppling failure is feasible over the entire slope along the joint sets.

Rockslide velocities were measured using dGNSS on installed bolts, together with ground based (GB) InSAR and satellite based InSAR, the latter using both natural outcrops and man-made corner reflectors. The measured slide velocities are consistent between methods in the upper and central part of the slide mass. Here, they mimic the structural configuration by showing slide vectors parallel to the azimuth of the slope and at an angle similar to the slope in the upper part (indicating wedge sliding is likely) and steeper than the slope in the central part. In the upper and central part, slide velocities are in the range of 1 – 2 cm/yr except at a few locations that are strongly broken up. Slide velocities in these heavily fractured areas can reach up to 4 cm/yr. Deformation measurements on the steep foot of the slide mass are limited due to access and shadow effects from the view of the satellite. GB InSAR suggest much lower velocities at the foot and no movement at the boundary between the foot and the scree. The unstable rock slope has very high rockfall activity. Surface exposure dating of rockfall boulders indicate that this activity has occurred for at least for one and a half millennia.

Due to the scree deposits, the lower limit of the scenario is difficult to define. We thus used the velocity distribution to define the lower boundary. We infer that the lack of deformation at the foot indicates that the thrust fault is that boundary. The delimiting structures result in a rockslide volume of 9.5 million cubic meters. Run-out modelling using DAN3D suggest that a large portion of the rock mass will reach Vangsmjøse should the mass release suddenly. Displacement wave models based on these run-out simulations suggest that large areas around Vangsmjøse would be inundated by the resulting wave.

The overall geological conditions of scenario A are interpreted to represent a high likelihood for a sudden failure and the consequences around lake Vangsmjøse are high. Skutshorn scenario A is thus classified as a high-risk site.

Scenario B has a well-developed back scarp and free flanks. The lower boundary of the scenario cannot be mapped out due to scree cover, therefore, we again infer that the nappe boundary forms the basal failure surface. The structural conditions are similar to the foot of scenario A but a well-developed exfoliation joint was identified here in addition. This structure dips out of the slope and daylights. This structural configuration is therefore critical and allows for planar sliding. Due to the inability to access the slope, slide deformation velocity measurements rely on satellite based InSAR, which indicates velocities of up to 4.5 mm/yr.

The volume of scenario B was estimated at ~150,000 cubic meters. Run-out modelling using DAN3D suggests that in an event of a sudden failure a large portion of the mass would reach lake Vangsmjøse. Displacement wave modelling using the SPLASH formula indicates local run-up heights of ca. 4-m. Such a wave could result in the loss of lives, but fewer than related to a failure of scenario A. Based on the geological conditions scenario B is interpreted to have a medium likelihood of failure, which together with potential lives lost results in a medium to high risk.

Deformation in the phyllite of the Vangs nappe along Vangsmjøse was mapped in the form of open cracks. Rock fall has historically also been sourced from bedrock outcrops here. dGNSS measurements were performed over a period of 3 years on two measurement bolts. Both showed a strong deformation in the first measurement interval. This was reversed on one of the bolts in the

following measurement interval, while the direction of displacement changed strongly on the other. GB InSAR did not detect any deformation on the phyllite outcrops while satellite based InSAR suggests slide velocities of ~1 cm/yr locally. No deformation was mapped on the bathymetric data on the slope under water. An electric resistivity profile was taken along the road along Vangsmjøse. This road lies on scree from the unstable slope and partly on the phyllitic bedrock. The results are interpreted as a transition from scree to fractured water saturated bedrock to unfractured bedrock in the subsurface. Thus, currently it is not feasible to determine the limitations of deformation in the phyllitic bedrock.

Table of contents

1. INTRODUCTION

In the 20th century, Norway experienced ten rock slope failures of rock avalanche size (Furseth, 2006; Hermanns et al., 2021), the highest number of any European country. Moreover, Norway experienced the second highest loss of life related to such landslides and associated displacement waves (tsunami waves triggered by subaerial landslides impacting into a water body) in that century, with a total of 175 people in three events (Hermanns et al., 2012a). Life losses to such phenomena were only exceeded in the 20th century in Italy by the rockslide and subsequent displacement and flood wave at Vajont and Langarone valley in 1963 (Hendron and Patton, 1987).

The Geological Survey of Norway (NGU) has been involved in the study of such events and unstable rock slopes since the beginning of the 20th century (Reusch, 1907). It has carried out mapping of unstable rock slopes since the end of the last century (Blikra et al. 1999). This work became systematic in Møre og Romsdal and Troms counties (today part of Troms og Finnmark county) in 2005 and in Sogn og Fjordane (today part of Vestland county) in 2007. Systematic mapping started in Rogaland county in 2015 and in Hordaland county (today part of Vestland county) in 2017. These counties were selected as life losses due to historical events have been highest there (Blikra et al., 2006; Furseth, 2006; Devoli et al., 2011; Øydvin et al, 2011). However, future events do not necessarily follow historical trends, and might occur in mountainous regions where historical loss events have to date been minor or absent. To deal with potentially critical rock slopes in other parts of Norway, which are not covered by a county project, the “rest Norge” project was initiated in 2010 and potentially critical slopes have typically been reported to NVE /NGU by respective county geologists.

Skutshorn was instead discovered and inspected from the road E16 (Figure 1) by Einar Anda while travelling on E16 in 2017 and as it showed signs of being potentially critical, mapping started in 2018. However, this mapping activity was overshadowed in the first year by an accident in the field with a rock falling out of the slope along the back scarp and hitting a member of the field party. Thus, mapping results were limited in that year. In the 20th century, Norway experienced ten rock slope failures of rock avalanche size, the highest number of any European country. InSAR Norway (www.insar.ngu.no) was launched in autumn 2018 and provided for the first time a nationwide dataset of satellite InSAR data documenting ground displacements (Dehls et al., 2019) and in only a few weeks more than hundred previously unknown unstable rock slopes were discovered (Hermanns et al., 2021). This dataset suggested that displacement rates of the unstable part of Skutshorn were up to 4 cm/year. This knowledge concentrated efforts on that slope in the following years.

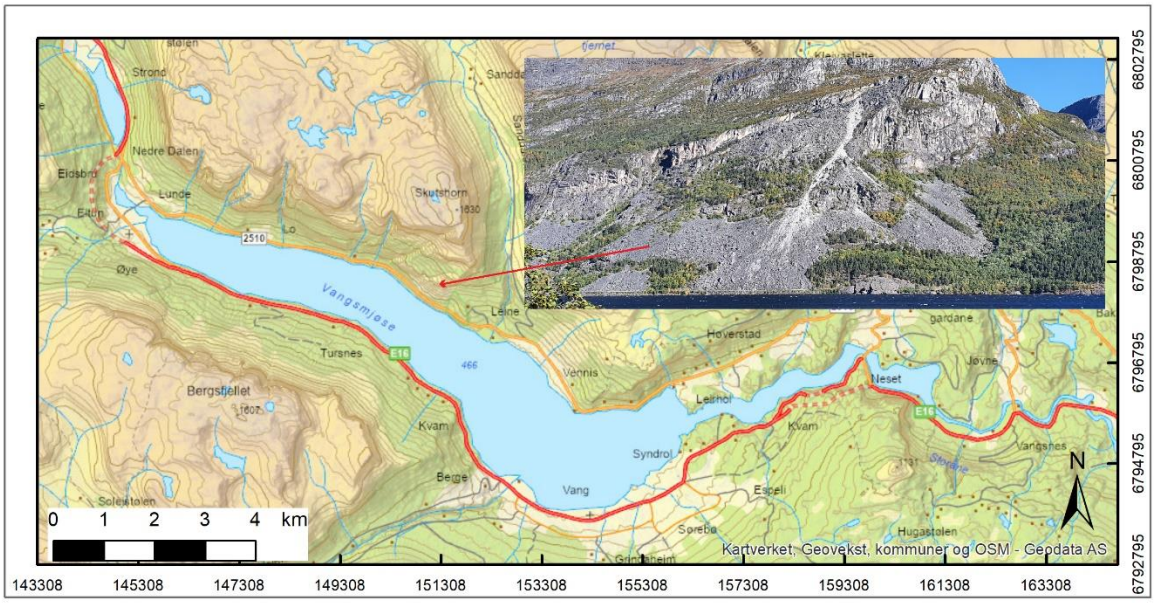

Figure 1) Overview map of Vangsmjøse with photo of Skutshorn as seen from the E16.

2. GEOLOGY

2.1 Location

Skutshorn (top at 1630 m a.s.l.) is located over the central part of lake Vangmjøse (at 466 m a.s.l.) along its northern shoreline, in Vang municipality, Innlandet county. The Norwegian noun “skudd” (English: “shot”) and the Norwegian verb “skyte” (English: “to shoot”) may relate to the rock fall often heard from that site and thus describes its nature as a source of sudden landslides. Photographic documentation reaching back to the beginning of last century shows traces of fresh rockfall activity. The lowermost 400 m of the mountain slope facing towards Vangsmjøse and towards the east is dominated by coarse scree deposits that consist nearly entirely of boulders (grain size > 256 mm). This lower portion has the characteristic field name “Kviture” in Norwegian, translating to “white boulder field”. Historic and modern photos suggest that rockfalls do not source from the 35° to vertical walls of the uppermost slope above 1100 m a.s.l. but instead from the 35-65° rock slopes lying between 1050 and 650 m a.s.l. In this slope section, the upper limit of the rock slope instability is easily visible as near vertical fracture with WSW-ENE orientation in the west and NW-SE orientation in the east, and which represents the back scarp of Skutshorn (Figure 3). This back scarp separates the almost intact bedrock from outside the instability from the strongly broken bedrock within the instability. Below we outline the bedrock and Quaternary geology of the area.

Figure 2) Historic photo of Skutshorn taken by photographer Jens Embertsen Robøle (1850-1932, year of photography is unkown). (Skutshorn i Vang. Vangsmjøsa i forgrunnen. - Valdres Folkemuseum / DigitaltMuseum)

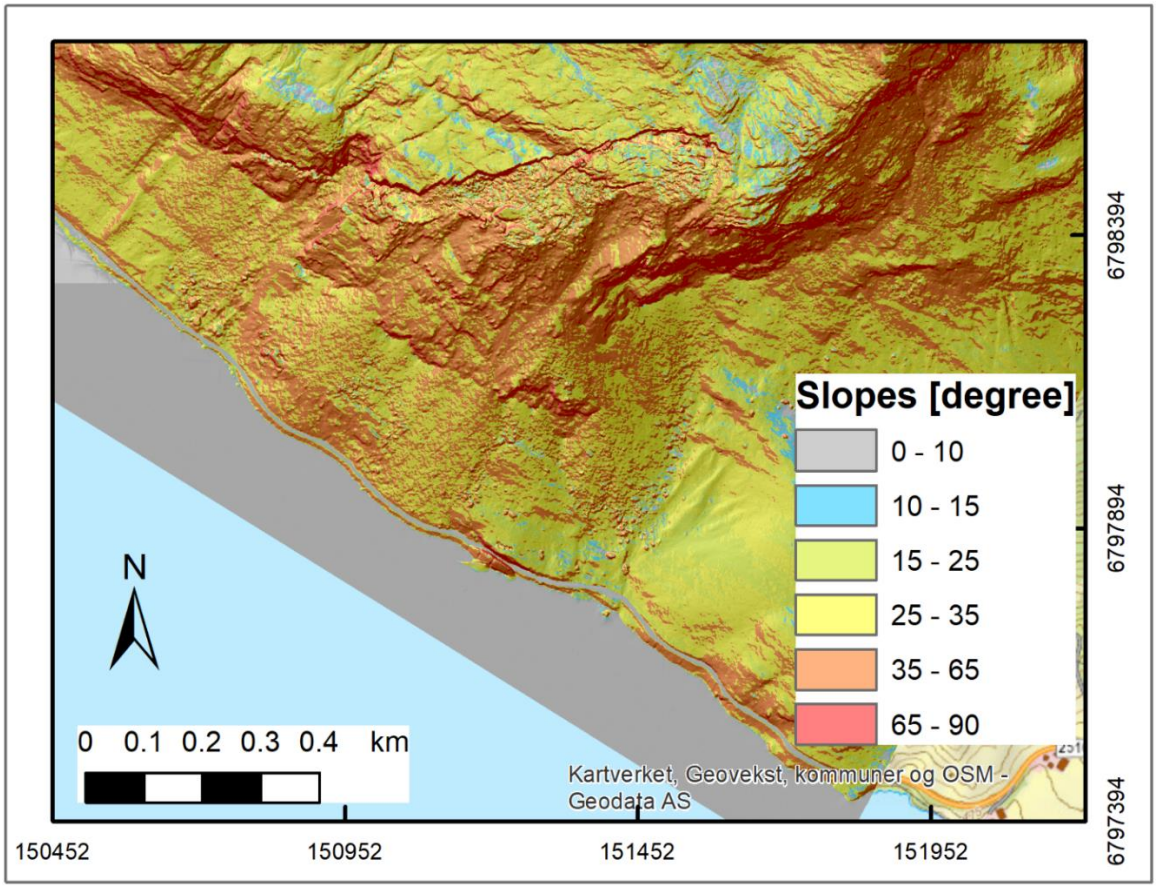

Figure 3) Slope map of the unstable part of Skutshorn at an elevation between 650 and 1050 m a.s.l. The near vertical fracture with a WSW-ENE orientation and representing the back scarp turning into the NW-SE oriented near vertical back scarp separates the intact bedrock outside the instability from the strongly fractured bedrock inside the instability.

2.2 Bedrock geology

The bedrock of the unstable part of Skutshorn is characterized by two lithological units. The upper unit is mapped in NGUs 1:50.000 bedrock map (Heim, 2003) as an arkose, however, the unit also contains quartzite and mica shists (Figure 4). These are metamorphic rocks. The arkose and quartzite also have a schistosity. Based on the quantity of exposed rocks, are the arkose and quartzite dominant on the slope. It is part of the Valdres sparagmite nappe that was thrusted onto the Vangs nappe during the Caledonian orogeneses (Heim et al., 1977). The lower unit is a phyllite that is part of the Vangs nappe which at places contains quartzite and graphite (Heim, 2003). At Skutshorn both nappes are folded in an anticline with the fold axis going along the ridge crest of the mountain. Therefore, both units are inclined towards the lake on the SE oriented side. In addition, both units are internally folded in various directions (Heim, 1979). While the upper arkose/quarzite has a thickness of only ca. 250 m is the lower phyllite more than 500 m thick in a profile 3 km to the west of the unstable part of Skutshorn. Both units extend all along the northern shore of Vangsjøse and have therefore important continuity (Heim, 2003).

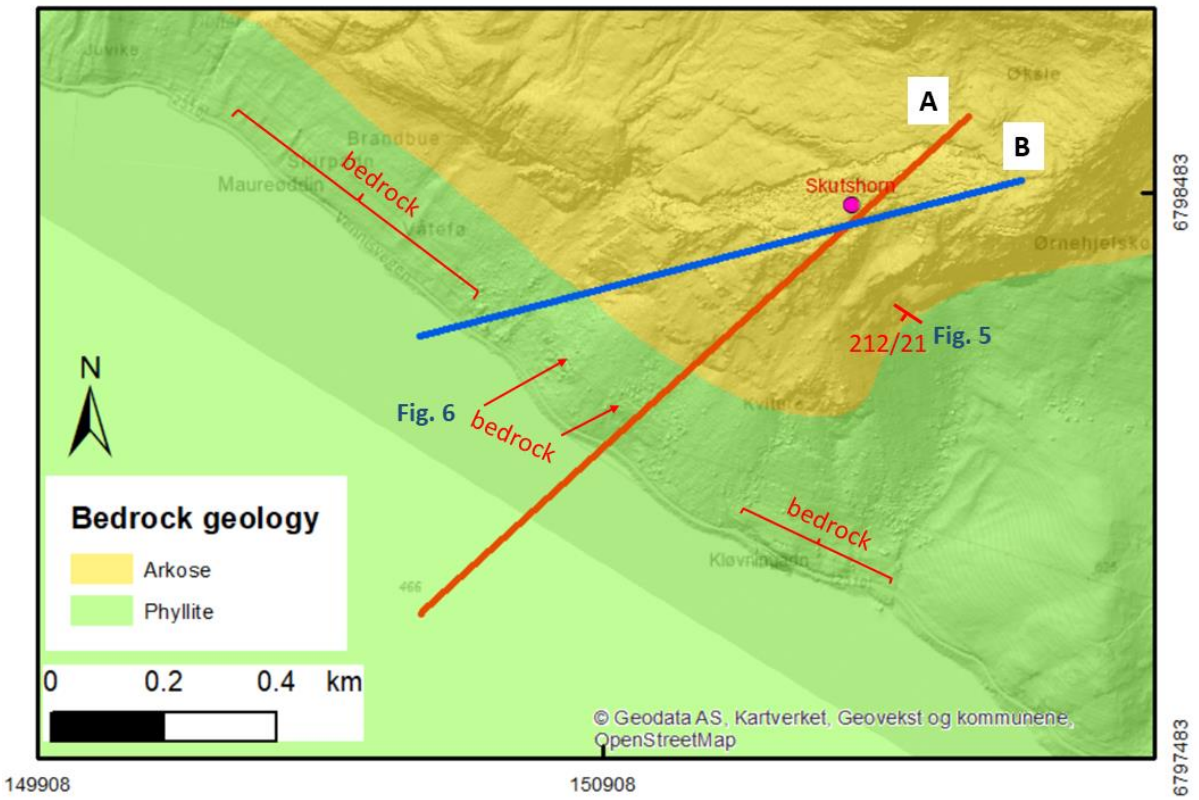

Figure 4) NGU 1:50.000 map draped over a hillshade map of the unstable rock slope of Skutshorn The line showing the position of profile A (red) and B (blue) shown in Figure 28.

Bedrock outcrops are abundant in the upper arkose/quartzite rock unit of the Valdres sparagmite nappe. The contact to the lower lying phyllite, however, is rarely exposed and almost everywhere covered by scree deposits. We investigated the only accessible outcrop to the east of the unstable part. At this locality the contact is rather gradual and no fault breccia was found (Figure 5),

suggesting the nappe contact is ductile (higher temperatures during tectonic deformation), which is consistent with the description of Heim et al. (1977). The foliation dips at 212/21 in this location (Figure 4), which coincides with the trace of the nappe boundary (Heim, 2003). The lower phyllite rocks are well-exposed along Vangsmjøse, the road to the WNW, and ESE direction from the scree deposit forming Kviture, however, only small, strongly fractured phyllite outcrops occur through the scree deposits themselves (Figure 4, 6). While the outcrops to the WNW of Kviture expose intact phyllite bedrock, the outcrops to the ESE are dissected by fractures that are several tens of meters long, several meters deep, and several meters wide.

Figure 5) Photo of the contact zone between the upper arkose unit (thick bedded rock) and lower strongly foliated phyllite. Photo is looking upwards, see tree for scale.

2.3 Quaternary geology

Like the rest of Norway the area around Vangmjøse was covered by glaciers during various glacial cycles in the Quaternary (Vorren and Mangerud, 2008). Vangsmjøse lies at the confluence of three glacially carved U-shaped valleys (Figure 7), the Sandalen draining from the north, the Begnadalen draining from the west, and the Skakadalen draining from the southwest into the lake. In confluent glacial valleys, the high erosion rates often result in deep thresholds that following deglaciation form lakes (Jansen, 1986). Vangsmjøse is such a lake. Glacial flow direction changed over this area related to the evolving position of the ice divide during glaciation (Vorren and Mangerud, 2008).

Vang is part of the area where the decaying Scandinavian ice sheet after the Last Glacial Maximum lasted longest, and all regional models suggest that the area of Vangmjøse was still under ice 10,000 years ago (Hughes et al., 2016) (Figure 7). Climate reconstructions suggest that winter temperatures in southern Norway were slightly colder and summer temperatures slightly warmer at that time than today (Lilleøren et al., 2012), and the deglaciation in the Vang area and elsewhere in the inland part of southern Norway was characterized by a vertical thinning. Thereby, the highest mountains became ice free before the valleys.

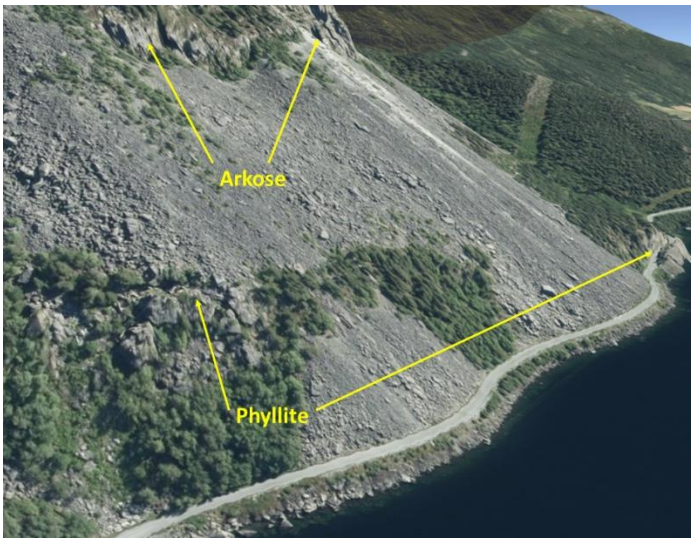

Figure 6) Oblique aerial photo towards the SEE over the Kviture scree deposits showing the massive arkose outcrops at the top and fractured to strongly fractured phyllite outcrops in the lower section of the slope.

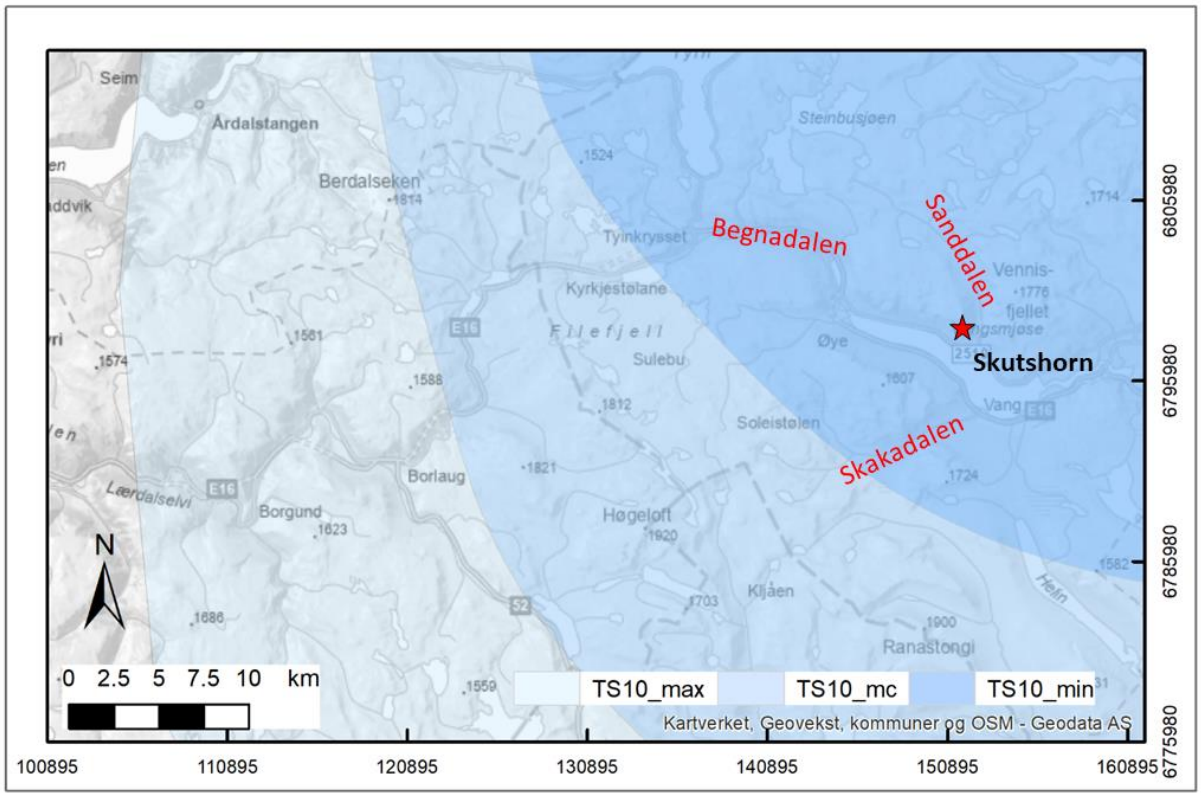

Figure 7) Interpreted regional extend of the Scandinavian Ice sheet at 10 kyr ago with its maximum extension (TS10_max), its mean extension (TS10_mc), and its minimum extension (TS10_min) draped over the local relief map. Ice limits are taken from (Hughes et al., 2016, data repository). Note: This map scale of the regional ice sheet distribution is too coarse for the detail of showing ice flow direction or vertical thinning of the ice body. However, the model clearly shows that the three valleys draining towards Vangsmjøse were likely not ice free 10 kyr ago.

The superficial deposits along this part of Vangsmjøse are mapped at a scale of 1:250.000 (Sollid and Trollvik, 1991). In this coarse mapping, deposit boundaries are not demarcated precisely, and do not coincide with the detail shown in Figure 8. Nevertheless, the coarse mapping indicates that

only two units are present, “landslide material” below the rock slope, and “moraine material” towards the east. Comparing the extent of the scree deposit with the mapped “landslide material” indicates the large miss-match in map units. Similarly, to the SE of the unstable rock slope there are scree deposits that are related to rock fall activity. However, the smoother surfaces found further east are likely to at least in part consist of moraine deposits. In this area, a channel with pronounced lateral rims was inspected during field mapping, and was interpreted to reflect glacial deposition.

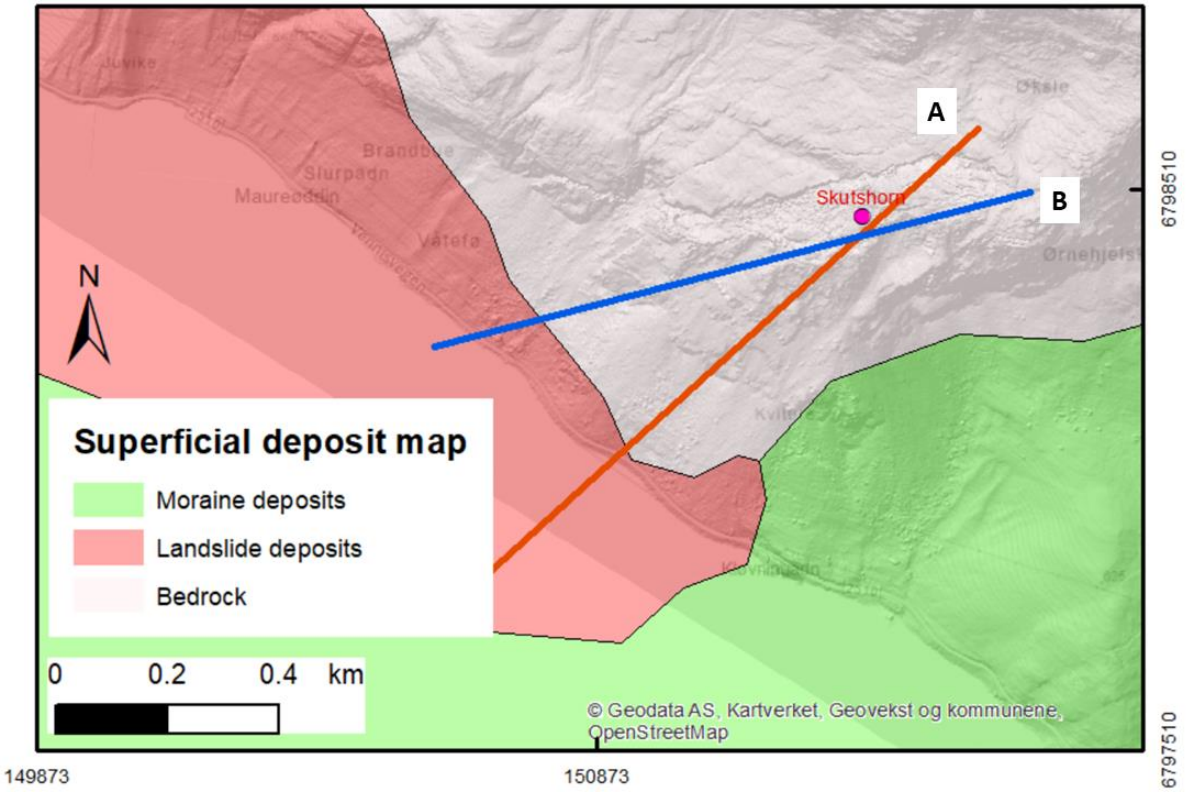

Figure 8) Quaternary database from NGU in scale of 1:250.000 that is part of the Oppland county map by Sollid and Trollvik, 1991, draped over the hillshade map. This map scale is too coarse for the detail shown in this map view and do not show the actual boarder of deposits. However, it is a good hint of type of deposits that occur in the area. The lines marking Profil A and B indicate the position of profiles shown in Figure 28.

Modern and historic photos suggest that the map unit “landslide deposits” comprises mainly landslides of the type “rock fall” deposits. This is also suggested by the morphology of the scree deposit, which do not show any channels or levees. Debris flow(s) as a scree producing process is thus very unlikely. However, it cannot be ruled out that part of the scree material was deposited by snow avalanches. The volume of earlier bedrock failures is impossible to evaluate from the land-based deposit alone. The deposits may result from various volume classes of failures that include rock fall (steinsprang) and rock collapse (steinskred), as these produce nearly identical landforms (Loew et al., 2021; Hermanns et al., 2022). However, they might also contain material from rock avalanches, which have larger volumes and higher mobility. To better understand the main process

forming the scree deposits, high resolution bathymetric data was acquired and surface exposure dating using the nuclide ^{10}Be carried out as part of this study.

On October 12, 2019, a rock fall occurred that reached county road 293 and Vangmjøse and led to a road closure (Figure 9a). A comparison of point clouds from photogrammetric models from 2018 and 2020 suggest that the volume was 565 cubic meters (Figure 9b) and was released from the front of the unstable rock slope (see below). However, aerial photos published by Kartverket on the project “Valdres 2011” show additional rock falls derived from the strongly deformed phyllite outcrop sticking out of the scree (Figure 9c), indicating that the entire slope can be source of rock fall (see also Figure 2).

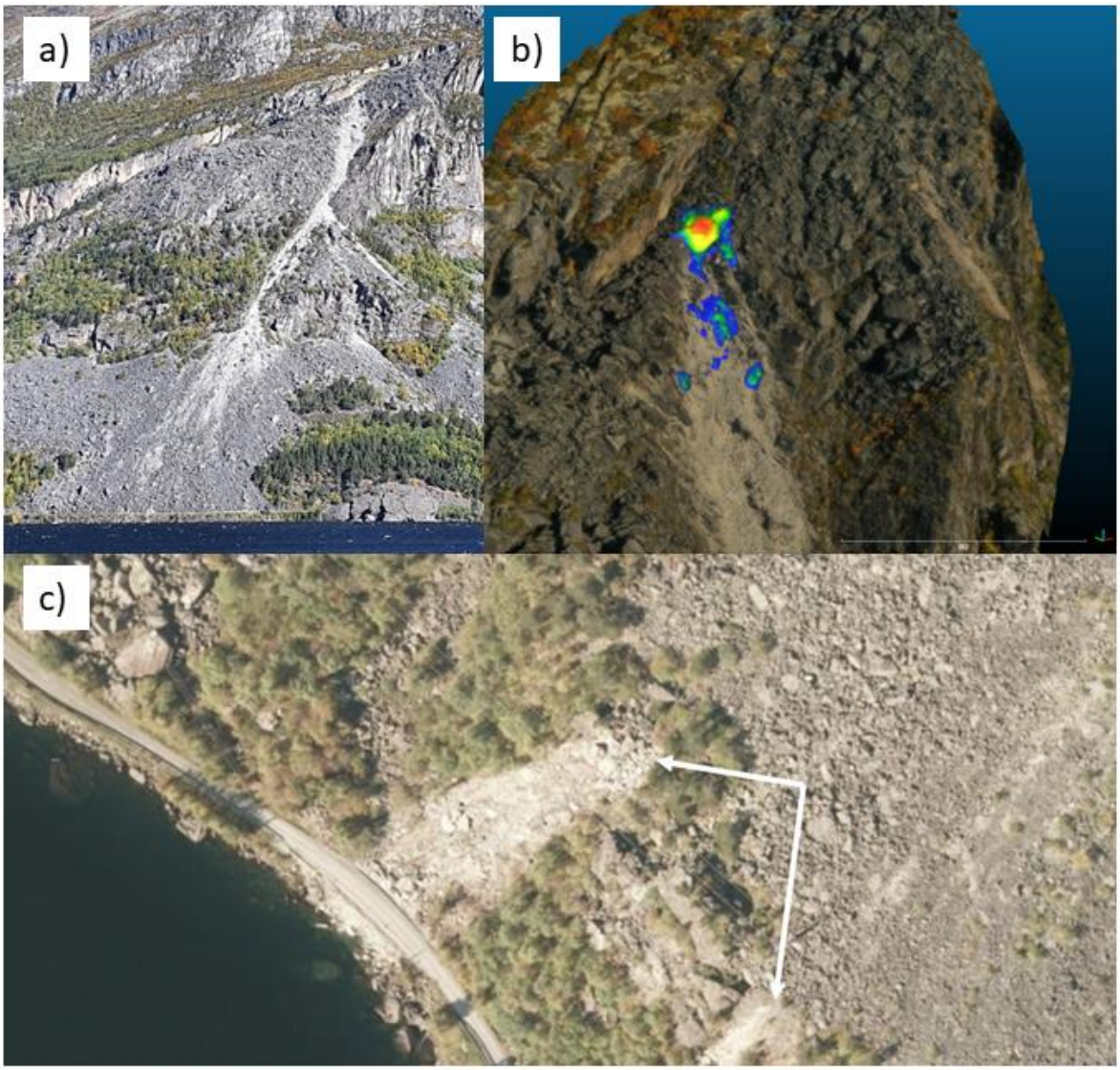

Figure 9) a) Photo of the October 12, 2019, rock fall. b) A comparison of photogrammetric models from 2018 and 2020 was used to calculate the volume of the event to include 565 cubic meters. c) Aerial photos from Kartverkets flight “Valdres 2011” document rock fall sourcing from the strongly cracked phyllites sticking out of the scree deposits in the lower part of the slope.

2.4 Description of the unstable rock slope Skutshorn

The morphological signs of rock slope deformation on Skutshorn were mapped in the field, from a hillshade model derived from the high-resolution LIDAR data collected by Kartverket, and aerial photos. In the following section we describe the main deformation structures.

The most prominent deformation structure on Skutshorn is the well-developed back scarp. In the uppermost part at 1075 m a.s.l. the back scarp is slightly spoon-shaped and parallel to the slope. It strikes here in a NW direction for a length of ~130 m (Fig 10, Figure 11a) before it turns into a WSW striking direction. Here, it crosses the slope obliquely (Fig 10, Figure 11b) and descends to 825 m a.s.l over ~480 m where it again turns slope parallel with a NW strike for another ~300 m (Fig 10, Figure 11c). The back scarp separates the strongly fractured bedrock from almost completely undeformed bedrock (Fig 10, Figure 11c). In the uppermost section, the back scarp is covered in a coarse boulder scree, while it forms a vertical wall in both lower sections (Fig 10, Figure 11b, c, d). To the N and NW of the back scarp cracks, depressions, and minor scarps indicate some slope deformation. However, the degree of deformation is much less outside the back scarp (Figure 10), and the density of cracks and scarps is low.

At 480 m a.s.l., where the back scarp transitions into a NW striking direction, there is a minor block that is strongly fractured and hereafter described as scenario B. This block is detached from the main deformation body (scenario A) by a deeply incised gorge and can thus fail independently from the main unstable rock mass. A well-developed back scarp of an earlier failure has cut into the back scarp here with a niche of failure (Figure 10). With exception of this minor block, the entire lower and SE side of the highly deformed main body (scenario A) is surrounded by back scarps of niches of failures. The rock fall from October 12th, 2019, sourced from this back scarp. It is not possible from field observations or topographic data over the unstable slope to determine whether these niches are the result of continuous rock fall, rock collapses, or a larger rock avalanche event. The volume missing is large enough that it could represent an earlier large event. Indeed, there is a smooth surface dipping ~40° towards the SW which potentially represents a basal failure surface of an earlier larger event (Figure 12).

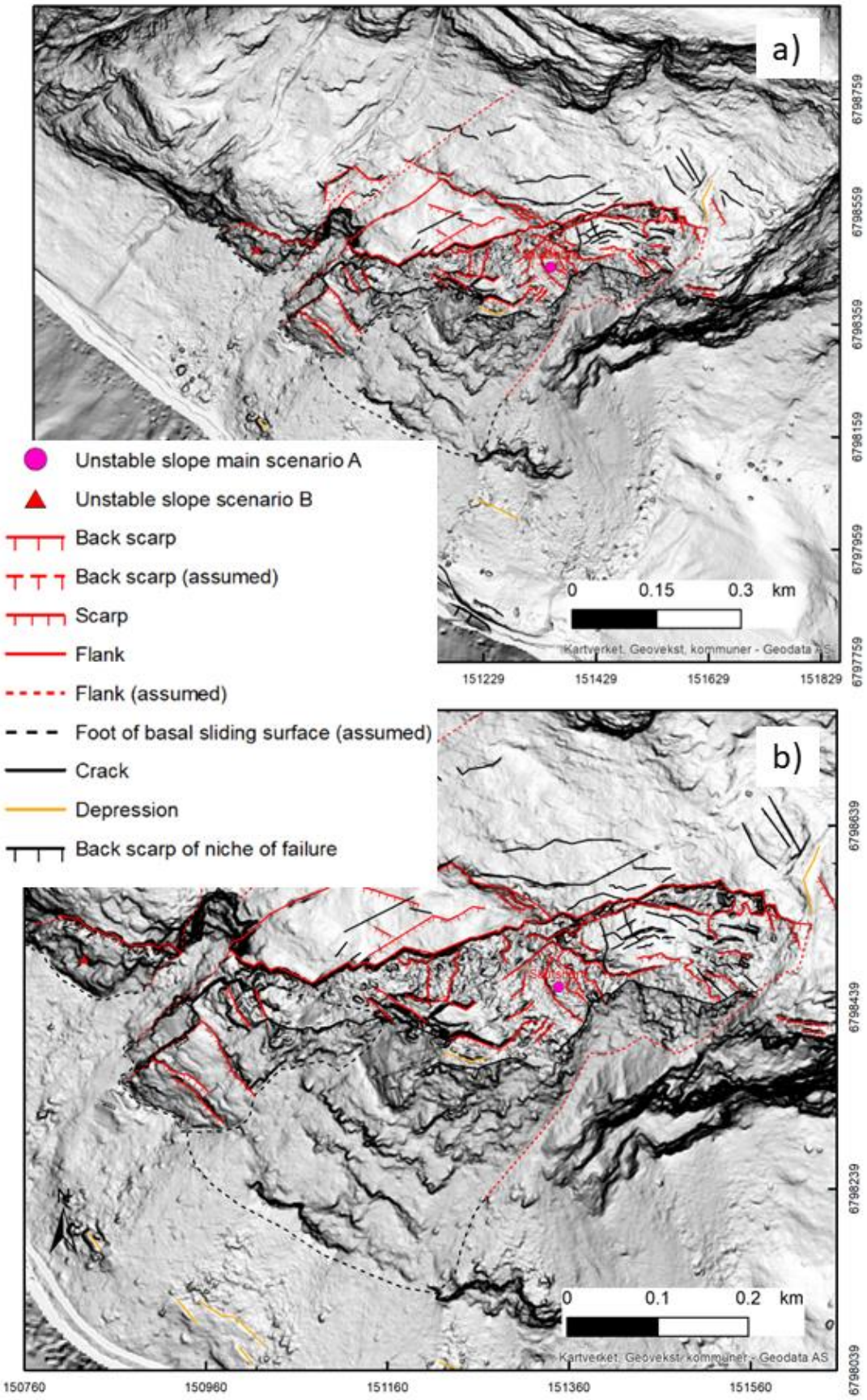

Figure 10) a) Hillshade draped over topographic map with main deformation features mapped out on the entire slope. b) showing the part of the unstable slope with most prominent deformation.

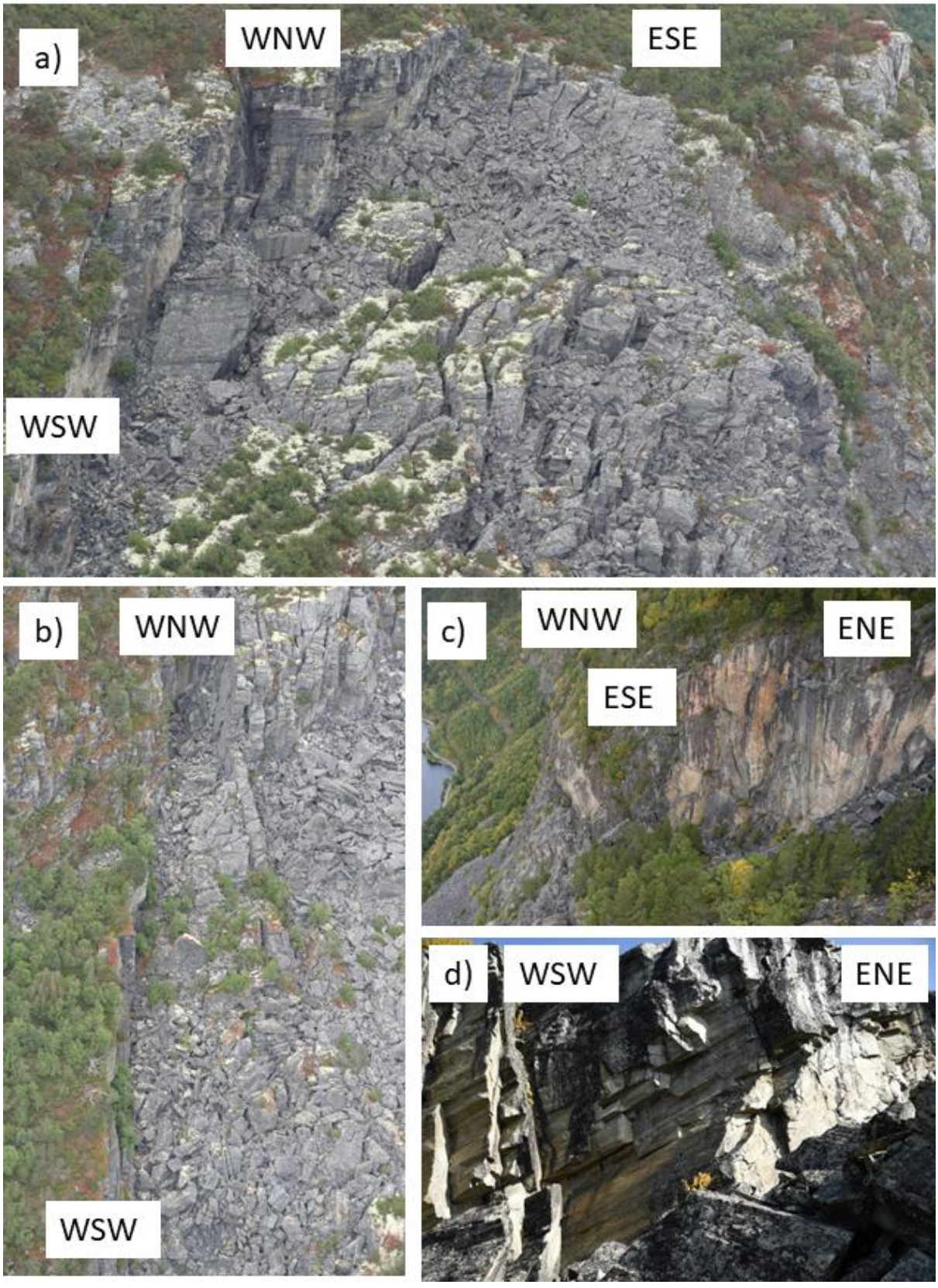

Figure 11) Photos of the back scarp: a) In the head area of the most unstable part. b) In the central area where the carp crosses oblique to the slope. c) In the lower area where the scarp runs slope parallel. d) Detail of the central part of the back scarp showing 50 m high vertical walls.

Figure 12) The main body of the strongly deformed unstable slope (to the left) and the underlying massive, undeformed bed rock below a failure surface. This failure surface might have formed during a large event or due to continuous rock fall from the unstable rock mass. The trace of the October 12, 2019 rock fall marks the limit between the unstable rock mass and the failure surface. The back scarp of the unstable rock mass is visible as a bright pink coloured rock band in the background.

The basal sliding surface of the unstable slope is not mappable in the field at its base, on aerial photos, or on the high-resolution hillshade model. This is different to the NE part of the instability, where the basal sliding surface is exposed (Figure 12). Rock deformation in the arkose / quartzite is visible down to the contact with the scree deposits. However, rock deformation is also visible in the lower lying phyllites. This rock deformation is characterized by strong disintegration and fracturing in the phyllite outcrops that protrude from the scree deposits, and cracks several tens of meters long and several meters wide and deep in the outcrops along the road in the southeastern part of the instability (Figure 10 a). Thus, it is a question of whether the deformation in the arkose/quartzite and in the phyllite are connected or separated from each other. To better understand the deformation at depth in the lower part of the slope, bathymetric data of Vangsmjøse and geophysical data along the road where collected (see below).

3. Methods

To understand the complexity of the Skutshorn unstable rock slope a multi-method approach was necessary. Combined, the methods give an understanding of the form, volume, and geologic development of the unstable rock slope that we feel provides sufficient confidence for hazard and risk analyses.

3.1 Hazard analysis

Hazard analysis of unstable (deforming) rock slopes have been carried out in Norway since 2006 (Blikra et al., 2006b). The focus was first to find high risk sites that require monitoring and early warning, and five unstable rock slopes have been classified as high-risk sites since 2009 (Blikra and Kristensen, 2013). The criteria used for hazard and risk classification were standardized in 2012 (Hermanns et al., 2012b). Since then all sites (not only high-risk sites) can be classified (Blikra et al., 2016). Sites that are not classified as high-risk, but are associated with building restrictions or have no follow-up consequences, now outnumber the high-risk sites (Hermanns et al., 2021). All sites classified as high-risk since the onset of the systematic approach in 2012 followed the method used in this report (Blikra et al., 2013; Böhme et al., 2016; Penna et al., 2021; Nicolet et al., 2022). The hazard analysis is based on three morphological observations (development of the back scarp, flanks, and toe line of the unstable slope), two structural observations (the orientation and persistence of the sliding surface, and kinematical feasibility of failure) and four activity observations (velocity of slope deformation, acceleration, earlier post glacial rock slope failure events of the same or similar scale as the presently deforming rock mass, and rock fall activity) (Hermanns et al., 2012b). The visible morphology of slope deformation and rock fall activity has been described in the previous chapter. The assessment of the remaining parameters is described below.

The above listed nine observations are assigned a score depending on the geological conditions observed. The maximum number of scores is predefined for each observation and the scores are summed (Hermanns et al., 2012b). Uncertainty in the observations can be expressed by distributing the score over several possible conditions. The sum of the score thus has a distribution that reflects the total uncertainty of geological observations. The sum represents the probability of failure with the respected uncertainties related to the geological observations. The probability of failure is split across 5 classes: very low, low, moderate, high, very high. These classes are connected to security classes related to the Norwegian building code (Blikra et al., 2016).

3.1.1 Structural geological data of the unstable slope and kinematic analysis

Both the arkose/quartzite rock in the overlying Valdres sparagmite nappe and the phyllite rock of the underlying Vangs nappe are affected by ductile and brittle deformation. The ductile deformation has caused the schistosity of the arkose quartzite and mica shists of the Valdres sparagmite, and small scale folding therein, and the foliation of the phyllites in the Vangs nappe. The brittle deformation is characterized by various sets of joints. The dip and dip direction of these structures was measured at several tens of sites inside and outside the deforming rock slopes with a compass, while he near vertical frontal part was measured from photogrammetric models in CloudCompare using photos taken from drone or helicopter. The photogrammetric data are not comparable to field data as only surfaces with considerable surface expression can be measured. Thus, this method is unable to capture structures that dip into the slope or have only small surfaces in the respective

slope orientation. Similarly, the characterisation of the type of discontinuity is based solely on the interpretation of photos taken from helicopter. Finally, structural observations along the foot of the slide area were made from helicopter photos as surfaces in that part of the slope are small, folded, and mainly vertical.

Orientation data were plotted, and kinematic analysis was carried out using the software Dips, version 7.0 (Rocscience.com). The majority of structural observations were acquired from outside the deforming area, or in the upper, less deformed part of the rockslide mass. Moving within the most deformed part of the mass was deemed too dangerous and, with only a few helicopter landing spots permitted, data collection was restricted (Figure 13).

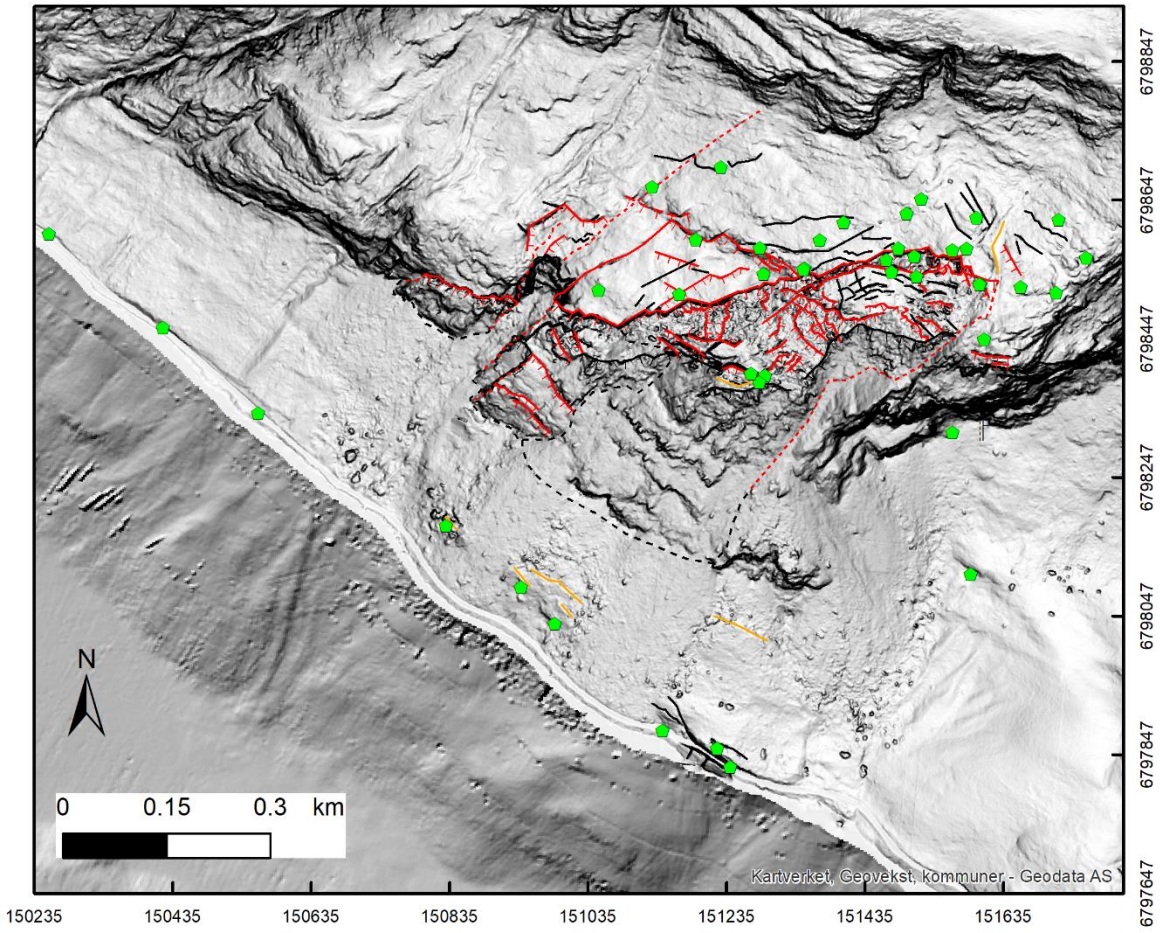

Figure 13) Map showing locations where structural data were collected in the field (green dots).

3.2 Deformation measurement

The highest weight within the hazard classification scheme is given to the displacement rate (Hermanns et al., 2012b). There are various methods to determine deformation rates, and all come with advantages and disadvantages. For example, differential Global navigation satellite system (dGNSS) measurements of bolts installed in rock allow a millimetric precision and indicate the 3D vector of deformation, however, it gives the deformation at only a single point in the rock outcrop.

Satellite-based radar interferometry (InSAR) on the other hand documents displacement over many measurement points providing insights of the spatial distribution of displacements. InSAR results also gives millimetre-scale precision, but detects displacement only along the line-of-sight (LOS) of the radar. If the true displacement direction deviates from the LOS, the displacement will be underestimated. In addition, steep cliffs produce shadows that cannot be observed by satellites. Ground-based radar interferometry (GB-InSAR) can also yield millimetric precision, however, again only in the imaging LOS. This system requires an installation with power source, thus it cannot be placed necessarily where best LOS exists. We chose a combination of these three measurement systems to build an understanding of rock slope deformation rates with high confidence for most parts of the unstable area.

3.2.1 Differential Global Navigation Satellite System (dGNSS)

Bolts for dGNSS reference stations were installed along shore of lake Vangsmjøse and close to the ridge top of Skutshorn. In total, ten bolts for rover stations were installed inside the deformed rock mass (Figure 14). The reference station SKUT_GPS_FP and the rover stations SKUT_GPS_01 to SKUT_GPS_06 were installed in 2018 while the additional locations were installed in 2020 after the first reliable results were obtained. This was done to increase the spatial understanding of deformation. Static phase measurements of these measurement points were carried out once a year over a length of at least one hour and the data processed using the reference points from outside the deforming mass. The displacement rate was considered significant under the condition that the documented data showed significant movement within sigma 3 uncertainty (99 % confidence level) and the displacement followed a coherent trend over the years. Processing of data follows NGU standard processing of dGNSS data as established in Oppikofer, et al. (2013). For the data from the upper slope, surrounding meteorological stations were used to correct the data (Trond Eiken pers. com.). This effort was not necessary for the measurements of bolts installed in the phyllite along the lake shoreline (SKUT_GPS_07 and SKUT_GPS_08 in figure 14) as, at these sites, the time series covered only two years and the measurements did not indicate a consistent deformation trend for SKUT_GPS_08 and a large variation in direction for SKUT_GPS_07 (see chapter 4.3.1.1). While SKUT_GPS_07 has a relative large open horizon to the south and east, is SKUT_GPS_08 surrounded by large trees.

3.2.2 Satellite-based radar interferometry (InSAR)

Skutshorn exhibits good coverage of satellite InSAR data due to little vegetation, making it possible to detect displacement rates at millimetric precision. Skutshorn is covered by two ascending and two descending datasets from the Sentinel-1 satellites over the period 2015 – 2023 (Fig 15 and 16).

As mentioned before, the sensitivity of InSAR to ground displacement is highest along the satellite LOS, while it is not possible to detect the horizontal component of displacement orthogonal to LOS.

The unstable slope is oriented toward the south-west and displacements are possible to detect with both satellite orbit geometries, though the sensitivity is best from the descending satellite orbit (line-of-sight equals c. 280/40). In both ascending and descending direction, however, that the 'true' displacement is underestimated to some degree.

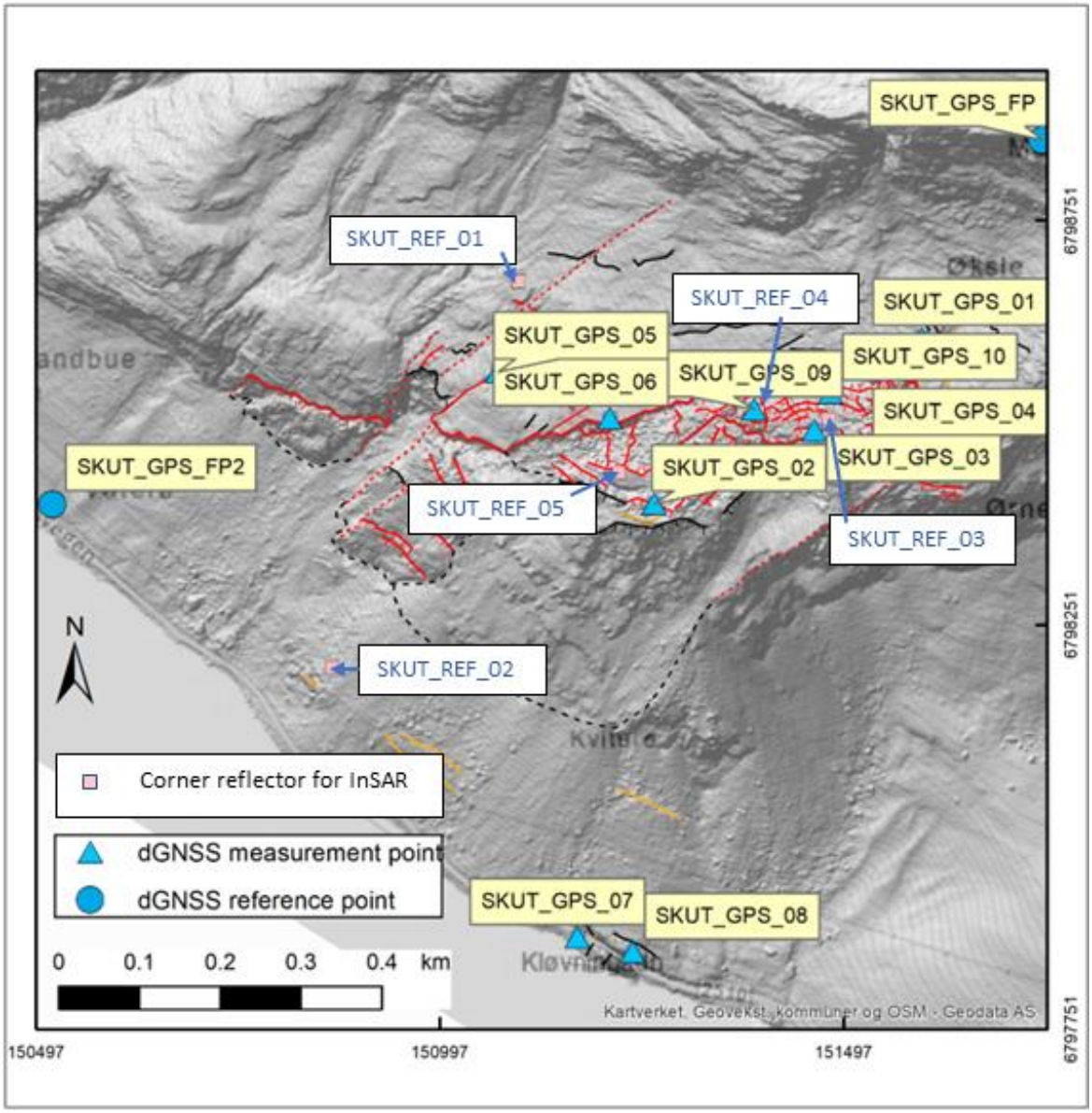

Figure 14) Map showing distribution of dGNSS reference and measurement points (see year of installation in the text) and corner reflectors for satellite based InSAR.

Table 1 Available datasets for Skutshorn; period for data acquisition and viewing geometries.

Dataset	Period	Incidence angle	Azimuth angle
Descending 1	2015 – 2023	40°	10,5 (NNV)
Descending 2	2016 – 2023	33,3°	12,3 (NNV)
Ascending 1	2016 – 2023	43,9°	170,6 (SSE)
Ascending 2	2015 – 2023	37,6°	168,8 (SSE)

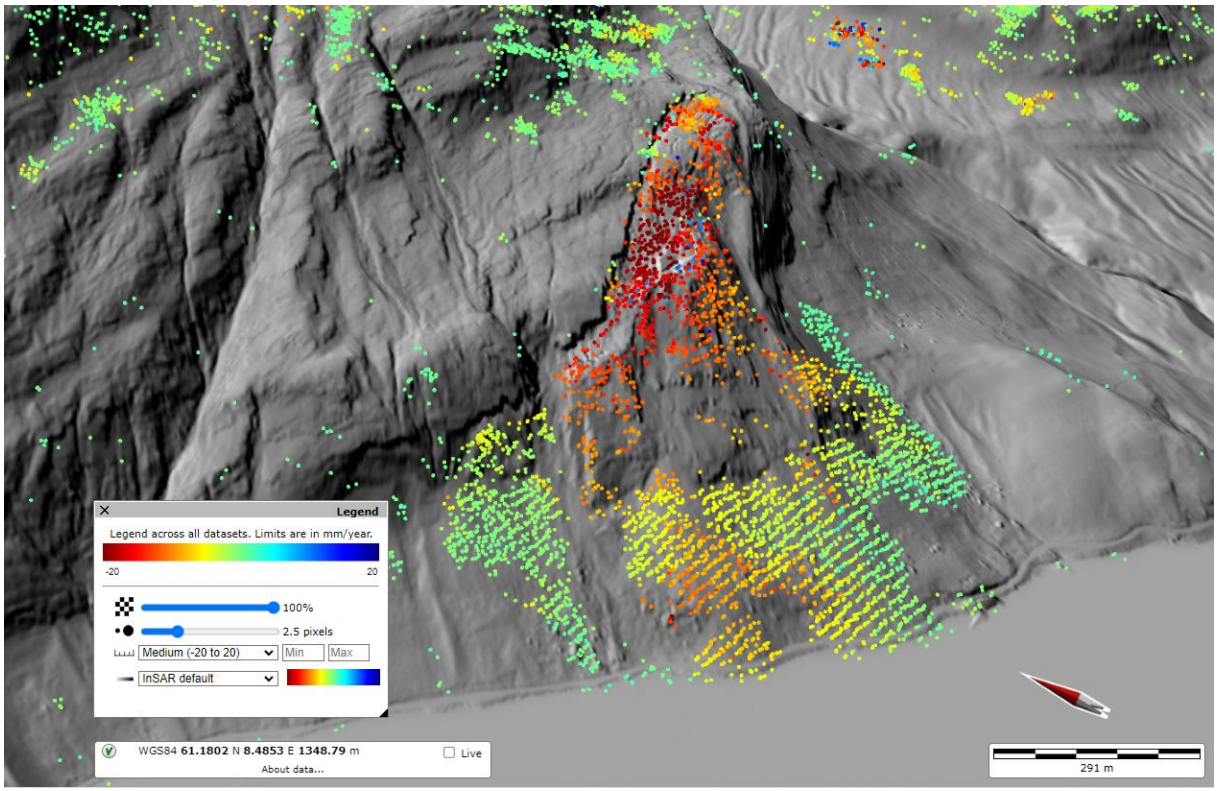

Figure 15) Map of data points from the descending track 2. Retrieved from insar.ngu.no 02.03.2023. Note that the potential basal failure surface (red arrow, see also figure 13) lacks observation points as it lies in a topographic shadow.

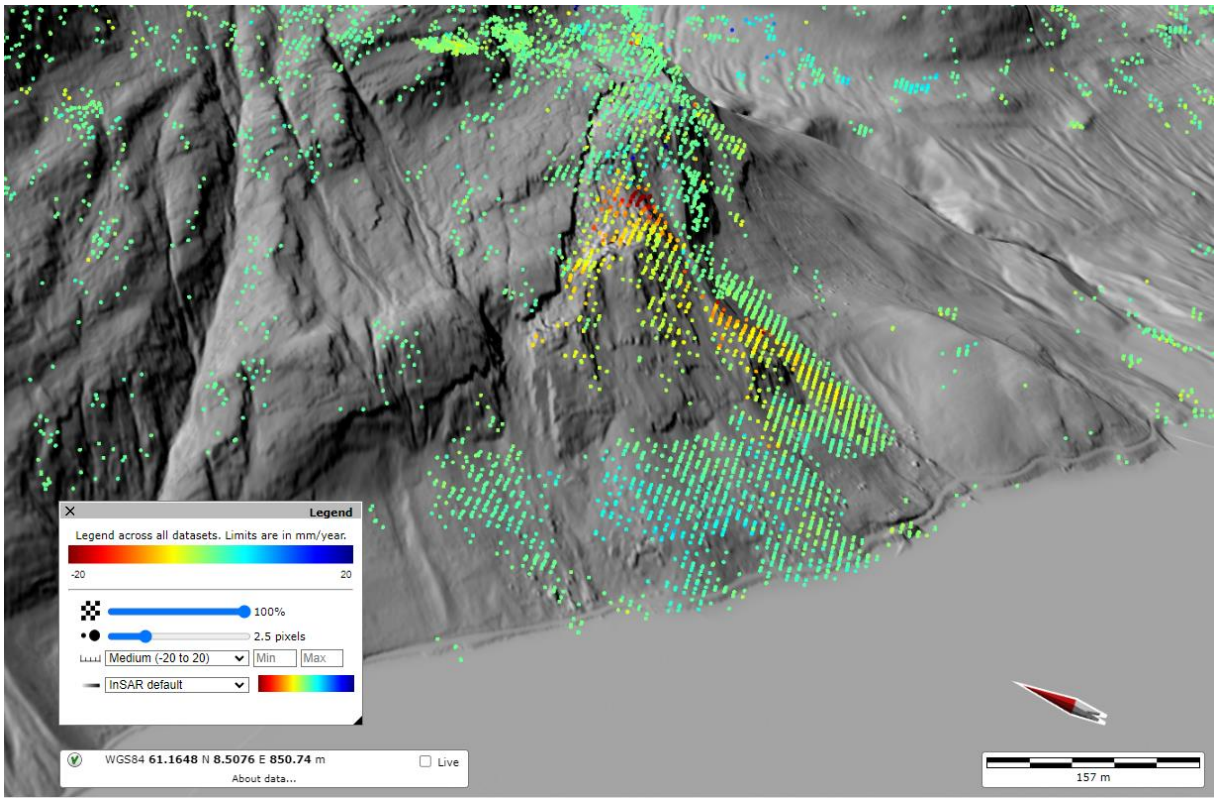

Figure 16) Map of data points from satellite track Ascending 2. Retrieved from insar.ngu.no 02.03.2023

Another limiting factor of satellite InSAR is that we are unable to estimate displacement when the slope is snow covered. To mitigate this, five corner reflectors (CRs) were installed above the snow cover depth, making it possible to measure year-round displacement rates (Figure 14).

3.2.3 Ground-based radar interferometry (GB-InSAR)

Two periodic campaigns with GB-InSAR were carried out at Skutshorn: 02.07. 2019 – 08.08.2019 and 17.07.2020 – 25.08.2020 from two different locations. The measuring locations and the data coverage is shown in Figure 17.

The radar used was a LiSAmobile from LiSALab Ellegi srl, which was leased by NVE, who carried out the field campaigns and data processing. The radar emits microwaves with an average frequency of 17,2 GHz and receives the reflected signal from natural reflectors on the slope (Fordella et al., 2018). It records displacement in the slope by InSAR processing and provides a distributed 2D map of displacement. Areas of low reflection or low coherence were filtered to remove noise from vegetation. Atmospheric noise was removed using a linear function derived from image to image from stable reference areas on the slope.

2-300 scans per day were obtained during the campaigns, but they were averaged to 8 or 24 hours to increase the signal/noise ratio and obtain the best possible images.

Usually, good time series of movement can be obtained by accumulating interferograms. However, when measuring across a water often more issues with atmospheric disturbances arise, which was indeed the case for Skutshorn. In 2019 the system was placed very close to the lake surface and the data had poor quality – but a few interferograms on selected days were of acceptable quality. In 2020 the system was placed about 20 m higher. The results were better but still strongly affected by atmospheric noise which we were unable to remove. Some fairly good images of the total displacement during the campaign were obtained by using interferograms on selected days and manually unwrapping fringes, where the displacement exceeded the quarter wavelength and phase wrapping occurred. However, no time series or automatically accumulated images were useful.

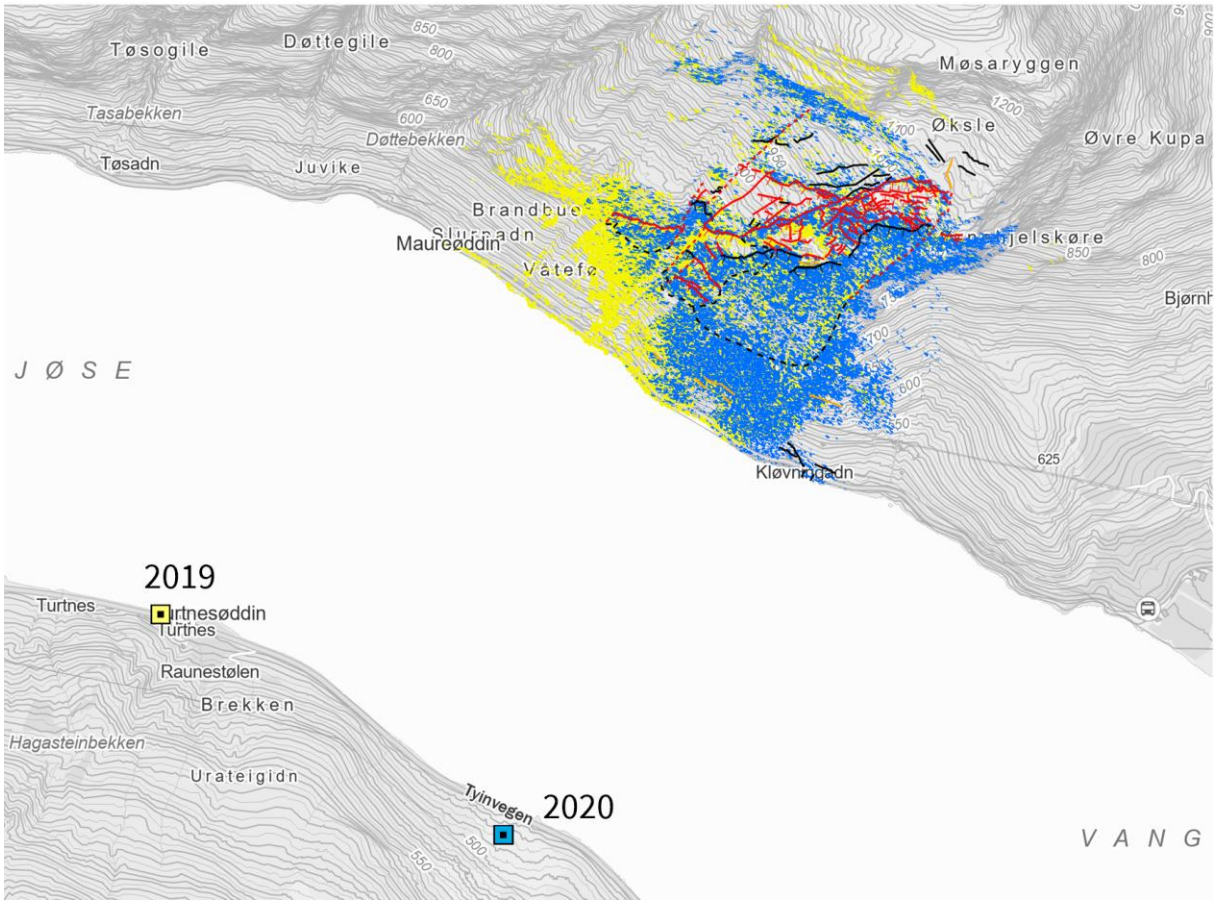

Figure 17) Map showing position of the LiSAmobile instruments in 2019 and 2020 and the areas where data points were acquired (yellow: 2019 data, blue: 2020 data).

3.2.4 3D analysis of coupled satellite and ground-based InSAR data

Using satellite based InSAR and GB-InSAR we obtained three-dimensional (3D) displacement vectors. To retrieve these displacement vectors decomposed into 3D components the InSAR LOS observations detected over the same location from multiple viewing geometries (i.e., ascending and descending satellite orbits, and ground-based radar viewing geometry) covering the same time interval, was combined. We used a GIS-compatible tool (Lauknes et al., 2020) exploiting two satellite sensor geometries (ascending and descending) and a third ground-based radar geometry and a digital elevation model (DEM) to estimate and visualise the annual mean velocity measurement points as vectors along defined profiles.

For the 3D decomposition we used the GB-based InSAR dataset retrieved over the period 19.07.2020 – 17.08. 2020. The velocity vectors attributed to the profiles are interpolated values based on measurement points located within 20 m perpendicular to the profiles.

3.3 Bathymetric data collection Vangsmjøse

As highlighted above, two main questions could not be answered solely by mapping of the unstable rock slope and deposits below: 1) where is the base of the deformed rock mass situated, and 2)

have rock avalanches have occurred in post glacial time on Skutshorn? To investigate these questions, it was necessary to map the bathymetry of lake Vangsmjøse. During September 17th-20th, 2021, high-resolution bathymetric data were collected from lake Vangsmjøse using a Kongsberg EM 2040P MKII multibeam echo sounder. The equipment was mounted on NGUs vessel 'Varv', a Sandström 560 MC. A frequency range from 200 to 400 kHz was selected and changed according to water depth. Swath coverage is 170 degrees at the widest, narrowing with higher frequency range and shallower depth. Sound velocity profiles (SVP) were measured using a Valeport SVP to adjust for changes in sound velocity in the water column at different locations. A Seapath 130 was used for positioning, and gave an accuracy of ± 1.5 m. The accuracy of depth measurements during data acquisition was in cm-dm scale. Processing was conducted using the Kongsberg software in combination with Caris HIPS/SIPS postprocessing software and included sound velocity correction and calibration to reduce signal-to-noise ratios and adjusting and filtering out offset data. Multiple overlapping runs over the same area according to standard procedures described in the Kongsberg manual were used to calibrate the system at the initial stages of the survey.

3.4 Geophysical methods

Electrical Resistivity Tomography (ERT) was used to map geoelectrical contrasts in bedrock based on fracturing or lack thereof, water content or lack thereof, mineralization etc. In all ERT surveys NGU conducts, chargeability is also measured alongside resistivity with the use of Induced Polarization (IP) method.

3.4.1 Electrical Resistivity Tomography (ERT)

The 2D ERT and IP methods are carried out by injecting current into the ground with the use of two electrodes and by measuring the voltage between two separate ones. Based on measured resistance (measured voltage / injected current) and a geometrical factor dependent on the electrode positions, the apparent resistivity and IP effect can then be calculated. The 2D ERT/IP measurements were performed using the Lund cable system (Dahlin, 1993) while ABEM Terrameter LS (ABEM, 2012) is the NGU in-house system for acquiring data. As seen in Figure 18, four multi-electrode cables are used to measure the Multiple Gradient electrode configuration (Dahlin & Zhou, 2006). Once the electrodes are connected to the ground and the cables to the instrument, an automated measuring procedure starts, by transmitting current through one electrode pair and measuring electric potential at another (up to four electrode pairs simultaneously). Resistivity is measured when the injected electric current is on, while IP-effect is measured shortly after cutting it. The cable length controls depth coverage and for 2, 5 and 10 m electrode distance, the penetration depth is ca. 20, 50 m and 100 m respectively, depending on the resistivity in the ground. Generally, resolution decreases with depth and deeper parts of the resistivity sections are, by experience, of low reliability.

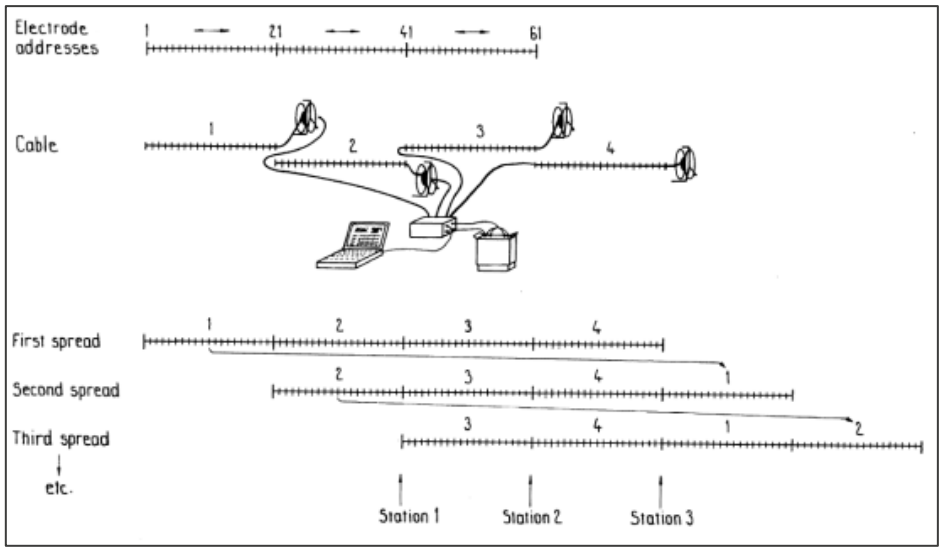

Figure 18) Diagram of measuring procedure that illustrates the setup of the Lund System and the roll-along method for performing measurements. From (Dahlin, 1993).

To detect the transition between scree deposits and bedrock there need to be a contrast in resistivity between these. If the scree material is water saturated there should be a considerable contrast to the bedrock, with the bedrock being more resistive. If the scree is dry, the contrast may be close to zero, making it very difficult to detect. It is also possible to detect a sliding surface where the unstable rock is detached from the host rock. Along the sliding surface, water could accumulate due to high fracturing making it less resistive than surrounding rock. Typical resistivity values can be found in Table 2.

Table 2: Resistivities in selected geological materials, from (Reynolds, 2011) and (Olesen, et al., 2020).

Material	Resistivity (Ωm)
Sand (water saturated)	30 - 800
Sand (dry)	100 - 3000
Moraine	10 - 5000
Crystalline rocks	< 2000
Weathered crystalline rocks	500 - 2000

3.4.2 Data acquisition

Field work was carried out the 16th of June 2022, information on the collected ERT line can be found in Table 3.

Table 3: Details of ERT profile measured, including length, electrode distance, no of datapoints and orientation.

Name	Length	Electrode distance	Datapoints	Direction
Profile 1	1200m	10m	2137 (0 removed)	West → East

As shown in Figure 19 the area is dominated by scree deposits. The entire length of of the profile follows a dirt road and the cable is set up between the road and the scree deposit. There is a metal crash barrier along the road for almost the entire length of the profile, but it is fastened on wooden stakes preventing the electicity from short circuiting along the metal. The point resistance between

electrodes and the ground was good along the entire profile. No electrodes had to be excluded due to poor connection.

Figure 19) Cable set up between road and scree.

3.5 Surface exposure dating with ^{10}Be

To determine whether the scree deposits underlying the unstable rock slope reflect the build-up of rock fall, or larger rock slope failures, such as rock collapse or rock avalanche events, boulders were selected for surface exposure dating using the nuclide ^{10}Be. This is a convenient method to date deposits of rock slope failures as no material other than the deposit itself is required (e.g. Ballantyne et al., 1998, Hermanns et al., 2001). The method is based on the build-up of the ^{10}Be nuclide that normally does not occur on Earth but is produced by cosmogenic irradiation at the Earth's surface (e.g. Gosse and Phillips, 2001 and references therein). The nuclide concentration in an exposed rock surface increases with time and the concentration can therefore be used to determine the exposure duration. By sampling boulder surfaces, the concentration can be measured in a laboratory. Quartz was separated from the rock samples and Be extracted at the Cosmogenic Nuclide Preparation Facility at the University of Bergen. The cosmogenic ^{10}Be concentration of the samples were measured at Aarhus AMS Centre (AARAMS), Department of Physics and Astronomy, Aarhus University, Denmark.

This method has been proven to date rock avalanche in Norway and is here used first to date deposits of more unknown origin (e.g. Schleier et al., 2015; Hilger et al., 2018). 14 large boulders with diameters of at least 1-2 meters were sampled from the "Kvitur" scree deposit that lies below the largest back scarp of failure niche (see also Figure 10). Additional three boulders were sampled from a scree deposit further to the northwest. This was carried out to understand whether the boulder ages are spread chaotically or if they cluster in time and/or space. The first is an indication of continuous rock fall activity while the next would suggest a rock collapse or rock avalanche origin.

3.6 Risk analysis

The risk analysis of unstable rock slopes had always been an integral part of the landslide assessment in Norway (e.g. Blikra et al., 2006b; Dahle et al., 2008). The risk analysis approach was described in detail in Oppikofer et al. (2016). This risk analyses follows a stepped approach that includes displacement wave analysis or landslide damming analysis where a landslide impacts either a fjord/lake or a river, respectively. At Skutshorn, which is situated above Vangsmjøse, we carried out the following steps to complete a risk analysis 1) volume calculation, 2) runout analysis, 3) displacement wave analysis, and 4) potential loss of life analysis. The risk classes following the Norwegian building codes are defined in Blikra et al. (2016).

3.7 Volume calculation

Following Oppikofer et al. (2016) a volume calculation can have various levels of quality. A standard method is the SLBL technique (Jaboyedoff et al., 2015 and references therein). For this technique the outer perimeter of the deforming rock body has to be known and a curved sliding surface is calculated for this perimeter. While the degree of curvature can be modified based on tolerance levels, the derived sliding surface cannot be forced to follow selected structures (e.g. tectonic weakness zones on the slope). This method was used to determine the volume of erodible material in the scree slope below the unstable rock slope. A more robust volume estimation can be made at deforming rock slopes which are strongly controlled by clearly observable weakness zones that separate deformed and undeformed rock, by manually defining bounding and basal planes (Oppikofer et al., 2016). This is the case at Skutshorn where weakness zones, namely the pronounced back scarp, divide a strongly deformed area inside the instability from a poorly deformed area to the northwest. Additionally, the basal failure surface described above (see also Figure 12) separates the deforming rock mass above from a rock mass with no visible deformation below.

In this study we followed this second approach by defining structural surfaces to delimit the deforming rock mass in PLANOS software (Pullarello et al., 2019). The inputs required are the position of the planes on the topography, their dip and dip direction, as well as a digital elevation model (DEM). PLANOS will generate these planes and extract the topography above them to enclose the body. This allows the tool to calculate the volume and create a new topography without the mass. For Skutshorn, we used a series of planes based on DEM analysis and field observations for each scenario. The planes used are given in the result section The resolution of the DEM was 10 m, which was down sampled from the 1 m LiDAR dataset.

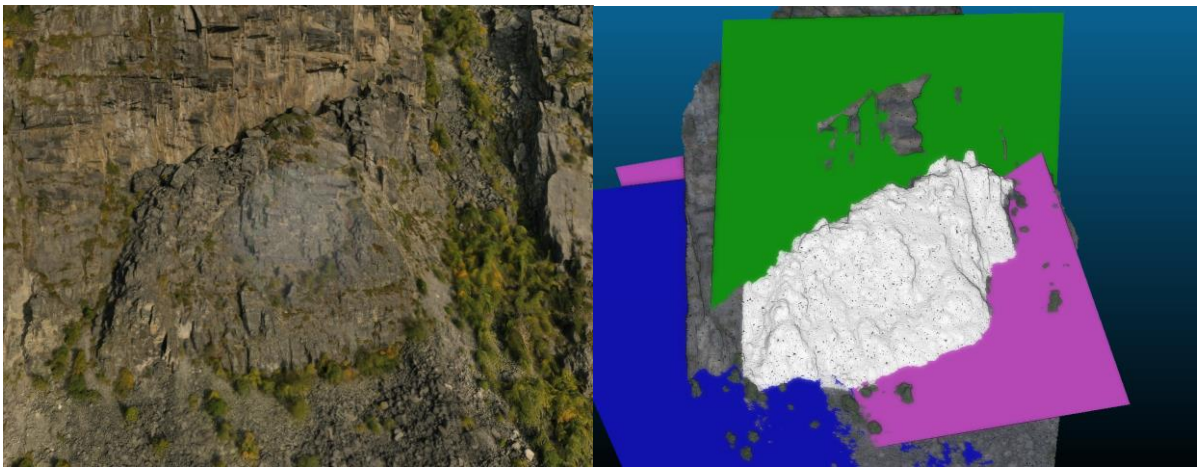

Figure 20) (Left) photogrammetry model using drone images taken on 2020 campaign of a detached unstable rock mass NNW of the main body of the deforming rock mass (See Figure 10 for location), (right) an example of volume calculation using PLANOS. The white point cloud is the topographic surface extracted by the 3 planes behind and beneath it (green, blue, and pink).

3.8 Runout analyses

The dynamic modelling of potential failure was conducted using the software DAN3D (McDougall and Hungr, 2004; Hungr and McDougall, 2009). This numerical simulation software is specifically designed to model the flow of granular materials such as rock avalanches, debris flows, and landslides. It utilizes a three-dimensional numerical model to simulate the behaviour of such flows, considering factors such as slope angle, topography, and material properties. The software requires input data such as the thickness of the sliding mass (source) and the path topography (both aerial and underwater), control parameters, and rheological parameters (McDougall and Hungr, 2004; Hungr and McDougall, 2009)

The control parameters for DAN3D refer to: 1) the number of particles 2) the smoothing coefficient of particles, and 3) the velocity smoothing coefficient. For Skutshorn, we modelled the propagation of the rock mass for the three scenarios using two different rheologies (Frictional and Voellmy) with 2000 particles and no smoothing coefficients. We performed a sensitivity analysis to test which combination of parameters would result in the most realistic deposit.

The scree material at the toe of the unstable rock mass is very loose and would likely be entrained during runout. We assumed that a depth of 5 m of scree could be mobilized. This is a simplification and entrainment will vary over the slope (see e.g. Chen et al., 2020). However, we believe that an overall thickness of 5 m is a reasonable estimate for a coarse granular material with large open voids that cannot store water or liquefy. Bulldozing of particles due to the high energy impact of the slide mass on the scree would likely represent the main entrainment type.

The range of parameters was determined by considering back-analyses of Norwegian rock slope instabilities in metamorphic bedrock (as shown in the following Table 4) and other mountain settings

(e.g., Hungr and Evans, 1996; Sosio et al., 2008; McKinnon, 2010). The modelled runout was compared with the volume/travel distance relationship for landslides (Scheidegger, 1973).

For the study area, we used the Frictional rheology for the subaerial part of the movement and the Voellmy rheology for the submerged part. This combination of rheologies has been used in previous studies on landslides propagating into water bodies (e.g., Mazzanti et al., 2010; Penna et al., 2017).

3.9 Displacement wave analysis

A first displacement wave analysis was calculated using the SPLASH relation (Oppikofer et al. 2019). It is a semi-empirical model for predicting the run-up height of displacement waves (tsunamis) generated by sub-aerial landslides. The model is based on ten events with multiple documented run-up values and focuses on the relationships linking run-up to distance from landslide impact with the water body, and landslide volume. Combining these relationships gives the SPLASH equation (Eq. 1) with best-fitted parameters a = 18.093, b = 0.57110 and c = −0.74189.

$$R = aV^b x^c \quad (Eq.1)$$

$$R = 18.093\, V^{\,0.57110}\, x^{\,-0.74189} \quad (Eq.2)$$

Where R is the maximum height of the wave in metres, x the distance from impact to run-up in kilometres and V the volume in millions of cubic metres. The resulting equation has been shown to be effective for preliminary hazard and risk assessments of unstable rock slopes above water bodies (Geertsema et al., 2020). The SPLASH formula also widely used today and referenced in high ranked international geological journals (e.g. Svennevig et al., 2023) gives only the maximum run-up at the end of the selected profiles, that can be interpolated technically in geographic information systems, however no real assessment goes into this interpolation.

To calculate the wave run-up heights around Vangmsjøe, the distance from the landslide impact point to the site of interest (wave profiles in Figure 21), and the changes in directions along the travel line, were computed.

Table 4, next page) Other simulations in the NGU internal database that show similar conditions either in the volume of mass in movement, type of movement, water content, etc.

	Source Lithology	Path lithology	Entrainment	Rheology	Standard unit weight	Friction angle (Frictional)	Pore-pressure Coefficient (Frictional)	Friction coefficient (Voellmy model)	Turbulence coefficient (Voellmy model)	Internal friction angle	Volume [10^6 m3]
Sosio et al. 2008				Frictional/Voellmy		Oct-30		0.1-0.25	450-1000	35-40	
Mazzanti and Bozzano, 2011									200		
Schleier et al. 2015				Voellmy	28			0.15	500	35	23.5
Schleier et al. 2017				Voellmy	28			0.1-0.13	600	35	15.1 / 5.4 / 0.3
NGU rapport 2016.047		debris	Yes	Frictional/Voellmy	26-30	15-35		0.1-0.25	450-100	30-50	2.4 / 0.48 / 0.075
Hungr (pers. comm. Ivanna)									150-200		
Gamanjunni 3	Metamorphic			Voellmy	22/27			0.05-0.1	500-800	35	
Stampa	Metamorphic	debris	Yes	Frictional	25/27	21-32	0-0.7			23-29	
Stampa	Metamorphic			Voellmy	25			0.2	250	32	
Doaresgaisa	Metamorphic			Frictional/Voellmy	27	20-30	0.5-0.7	0.05-0.1	500	35	
Storhaugen block	Metamorphic			Frictional		20				35	
Kvitfjellet (Norddal kommune)	Metamorphic			Voellmy	27			0.1-0.25	500-800	35	1.52
Klingråket (Sunndal kommune)	Metamorphic			Voellmy	27			0.1-0.15	500-1000	35	0.44
Ivasnasen (Sunndal kommune)	Metamorphic			Voellmy	27	17-20		0.15-0.25	600	35	2.21
Fulånebba (Sunndal kommune)	Metamorphic			Voellmy	27	20-25		0.15-0.25	600	35	0.95
Svarttinden (Rauma kommune)	Metamorphic			Voellmy	27			0.07-0.15	600-1000	35	5.95
Kilstiheia (Norddal kommune)	Metamorphic			Voellmy	27			0.1-0.25	500-800	35	1.59
Opstadhornet (Midsund kommune)	Metamorphic			Voellmy	22			0.1-0.35	300-500	35	1.56
Gikling 1 scenario A (Sunndal kommune)	Metamorphic			Voellmy	27			0.05-0.10	800-1000	35	19.1
Veslemannen (Rauma kommune)	Metamorphic			Frictional	28	30-34	0.1			35	0.062

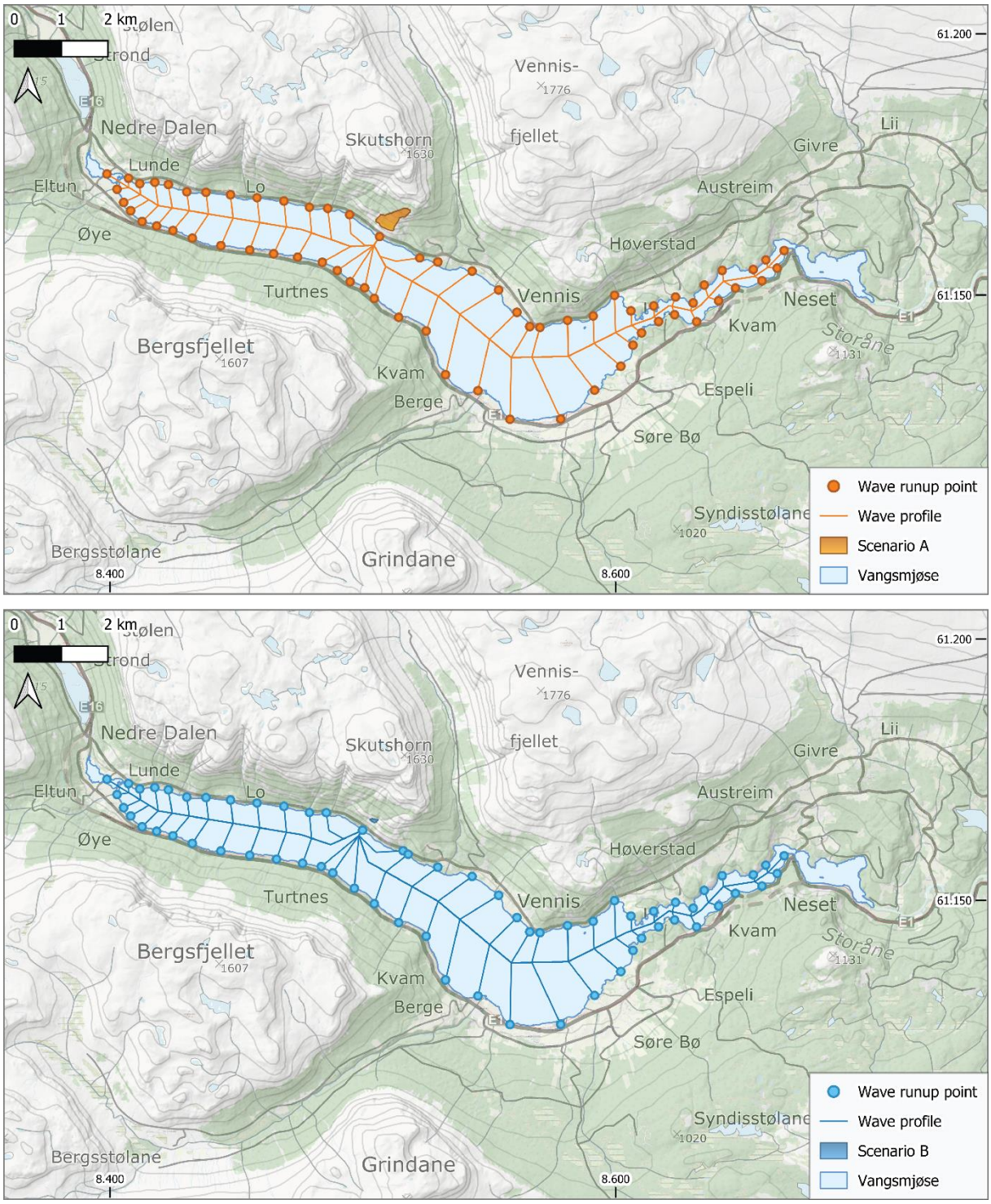

Figure 21) The map shows the possible path that the wave may take and the locations that could be affected. The lines indicate the direction to the sites and the number of changes in direction that were considered.

This preliminary displacement wave analysis resulted in high displacement wave run ups at certain locations along the lake (see chapter 4.10). As the SPLASH formula is a simplified approach and

does not give likelihoods of run-up, an 3D displacement wave analysis was carried out by the Norwegian Geotchnical Institute (NGI) reported in an independent report (Glimsdal, 2022).

3.10 Potential loss of life analysis

In this report, the consequences are only addressed as potential losses of life in the propagation area of the displacement wave area modelled by Glimsdal (2022) for the main scenario A and modelled for scenario B with the SPLASH formula as there are no buildings in the run-out area of both Skutshorn scenarios. Two hazard zones, as modelled by Glimsdal (2022) with probabilities of 1/1000 and 1/5000, respectively, were used in the analysis for scenario A. For scenario B with a likelihood of failure of 1/1000 – 1/2000 (see below) the run-up as determined with the SPLASH formula was used. Consequences are thus only addressed as potential losses of life within buildings in the propagation area of the displacement wave (tsunami). Detailed information on how the potential loss of life is estimated is given in Oppikofer et al. (2016).

Permanent residents and children attending school/kindergarten are counted based on statistics available from ssb.no. The number of people in buildings that are not primary residences is estimated based on the FKB-Bygning dataset (available from genorge.no) and standard values with exposure values that vary for different building types. Potential persons in transition on roads were not considered.

3.10.1 Risk analysis

The risk classification is obtained by combing the hazard score including the related uncertainty with the potential loss of life analysis, including its uncertainty in the risk matrix presented by Hermanns et al., (2012b). However, since the hazard zones defined for the displacement wave are given in predefined probabilities of 1/1000, 1/5000, but not for the probability of rupture, the consequences cannot be plotted in the matrix directly against probability of failure. Therefore, the consequences are calculated for each scenario and multiplied by the corresponding probability of failure to obtain the total risk as outlined in Penna et al. (2021).

4. RESULTS

In the following section, we present the results that form the basis for a geological model which underpins hazard and risk classification. We present the results in maps, tables, and along two profile lines that are important directions (A and B in Figures 4 and 8). Profile A is in a downslope direction and broadly parallel to most of the deformation vectors. Profile B is in the dip direction of the penetrative schistosity in the upper part of the unstable slope. This surface is seen as the most critical surface and the large niche of failure (Figure 10 and 12) and failure surface of earlier failures out of the unstable slope occurred above that surface.

Because profile A extends to the lake bottom of lake Vangmjøse, we start with presenting the results of the bathymetric analysis.

4.1 Results from the bathymetric analysis

Our analysis of the bathymetric data focuses on two main questions related to the hazard analysis of Skutshorn a) are there deposits of earlier rock avalanches in lake Vangsmjøse, and b) are there any signs of slope deformation visible below the unstable rock slope Skutshorn that would suggest that the basal sliding surface of the deforming rock mass is lying below the water line?

Figure 22 shows a shaded relief model of the Vangsmjøse bathymetry, and the unstable rock slopes registered in the NGU unstable slope database. This figure shows that lake Vangsmjøse has a flat floor representing basin infill by fine sediments, especially in the western part of the lake (Figure 22a). This flat part is also where the lake is deepest with 163 m below lake level (303 m a.s.l.). The central part of the lake basin is characterised by irregular terrain in front of the three valleys draining into the lake (Nedre Dalen to the east, Skakadalen to the south and Sanddalen to the north) (Figure 22a and b). The material sourced from Sandalen extends to the slope of Skutshorn. The irregular terrain is interpreted as deglacial deposits. It may contain material from relatively old rock avalanches or of rock avalanche material transported by glaciers into the basin that got later covered by lake infill. At the easternmost tip of Vangmjøse on the northern shore and east of the unstable slope Knappen there is a typical boulder deposit of rock avalanche material that is quite pristine suggesting a relative young age (Figure 22 c). Inspection of the boulders on land indicate that the rock avalanche was composed entirely of phyllites and thus that it sourced from the Vangs nappe. At that locality marks the Vang nappe a much larger portion of the slope compared to Skutshorn (Heim, 2003).

Below the unstable rock slope Skutshorn the bathymetric data shows that the scree deposits (described in chapter 2.3) are restricted to within 50 to 100 m of the shoreline (Figure 23 a). Further out into the lake, individual boulders cannot be distinguished. The only larger landslide deposit that can be traced from the unstable rock slope Skutshorn connects on land to the scree deposit below the niche of failure splitting the unstable rock mass in two parts scenario A and B (Figure 23 a, see Figure 10 for legend of lineaments). This deposit covers an area of about 450 m^2 of the lake bottom and two lateral levees enclose a channel that can be traced over much of the slope. This failure reached the deepest part of the lake east of Skutshorn. In the central and eastern part of Skutshorn there are clear signs of deposition of thicker basin infill, however this cannot be traced to the unstable slope and connects with the infill transported into the lake from Sanddalen.

Below the unstable slope there are several steps on the slope where bedrock seems to daylight. Those are not associated with signs of soft sediment deformation, and such steps occur below the unstable rock slope and outside the deformed rock mass both, within the lake and outside the lake.

The slope map shows that the slope within the lake and below the unstable rock slope Skutshorn is shallower than most of the unstable rock mass and the scree deposit on land (figure 23 b). The bedrock steps are the steepest parts of the slope within the lake. Slope angles are comparable to the slopes within the lake to the NW and SE.

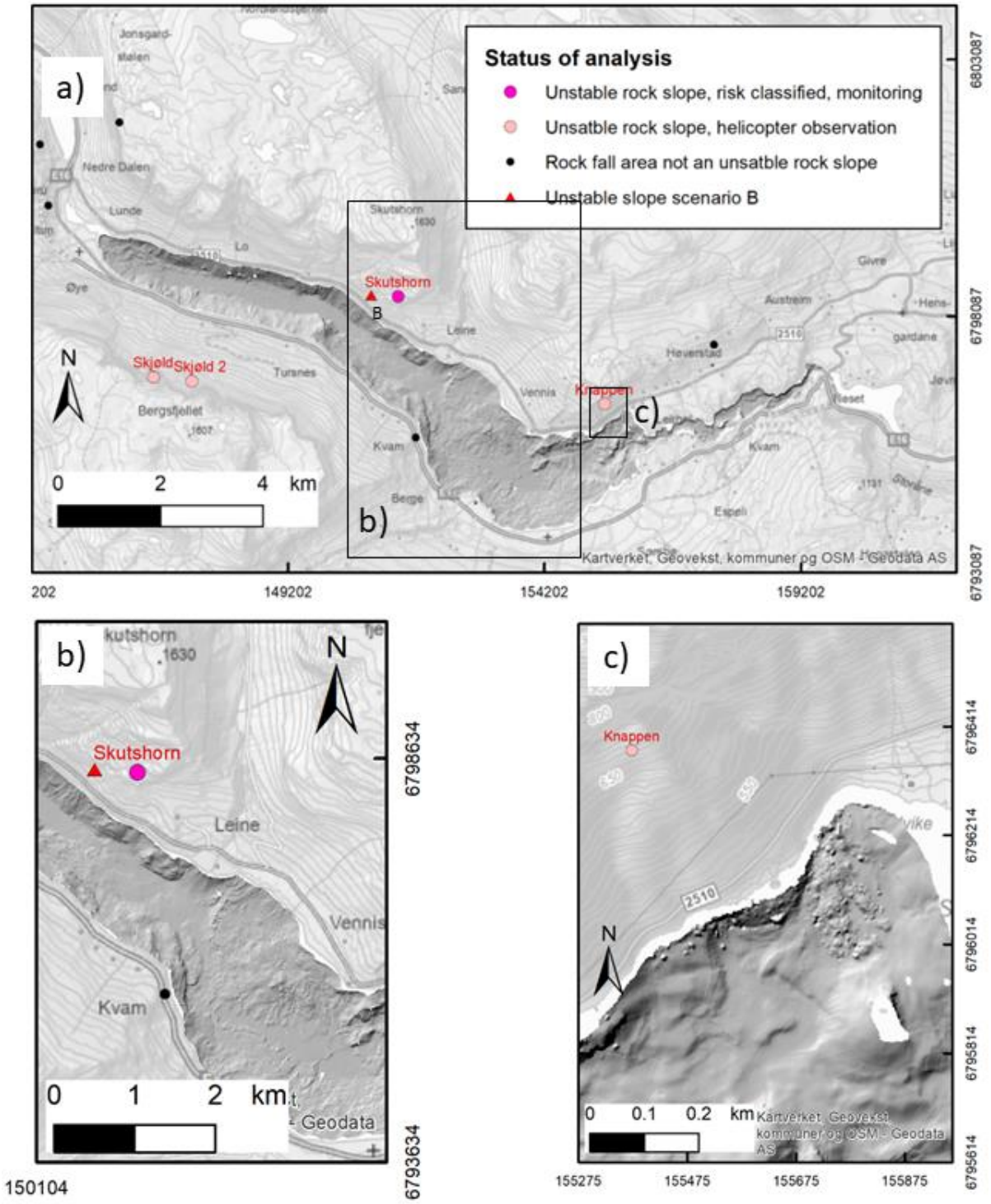

Figure 22a) Overview hillshade map of lake Vangsmjøse showing the flat basin floor to the east of Skutshorn and significant basin infill from the three surrounding valleys. The coloured and labelled dots represent unstable slopes in NGUs respective data base and if defined there scenarios

(triangle). b) Hillshade map of the central part of Vangsmjøse focusing on the basin infill from the valleys to the north and south. c) Detailed hillshade map of the north shore of the easternmost tip of lake Vangsmøse showing a lobate boulder deposit. These characteristics are typical for rock-avalanche deposits elsewhere.

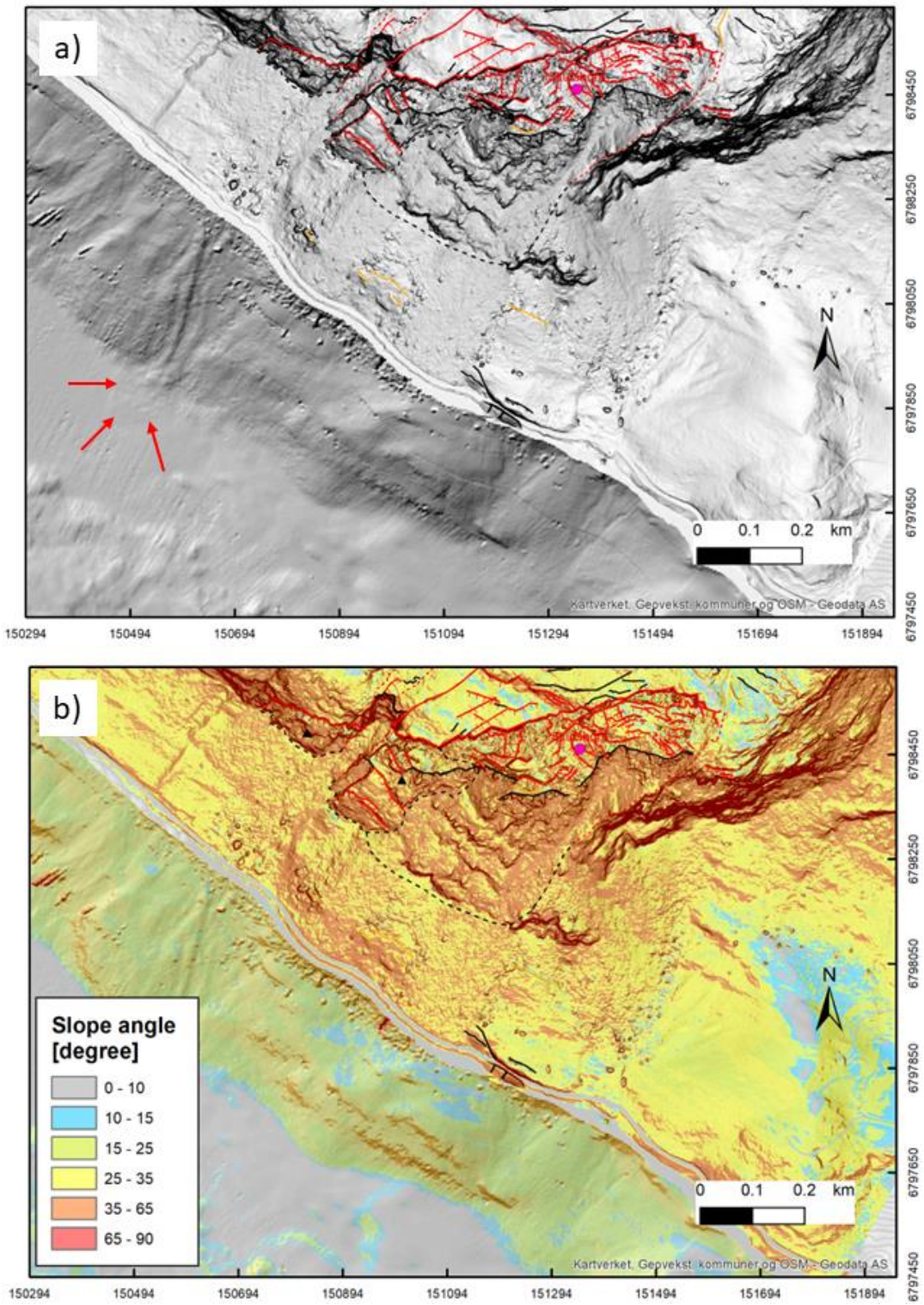

Figure 23a) Detailed hillshade map of the unstable rock slope Skutshorn and the lake bottom morphology below. The red arrows depict a landslide deposit that originated from the niche of failure (see Figure 10 for legend of lineamnets) b) Combined slope map the unstable rock slope Skutshon on land and the slope below the water line.

4.2 Litho-structural model of Skutshorn

4.2.1 Lithological model of Skutshorn

The lithological model is drawn here only for the profile A (Figure 24). This profile includes the entire slope from above the deformed rock mass to the lake bottom. The profile is relatively simple with 4 geological units the arkose/quartzite of the Valdres sparagmite in direct contact over the phyllites of the Vangs nappe. Within the profile there is no outcrop of the contact daylighting, but we here use the observations from an outcrop to the east (see Figure 4) and the geological map of Heim (2003) to infer the inclination of this contact.

This contact is covered in the profile by the scree deposit sourced from the unstable rock mass. The outcrop of the phyllites are slightly exaggerated in the profile to indicate their presence within the scree. The bouldery scree deposit extends from the foot of the unstable rock slope in the arkose/quartzite, into the lake where it extends for 50 m from the shoreline at a water depth of ~40 m. Beyond this depth, the lake bottom is covered by relatively fine-grained material and no single boulders can be mapped. The thickness of those fine-grained sediments might be exaggerated in the profile and the phyllite might locally reach close to the surface.

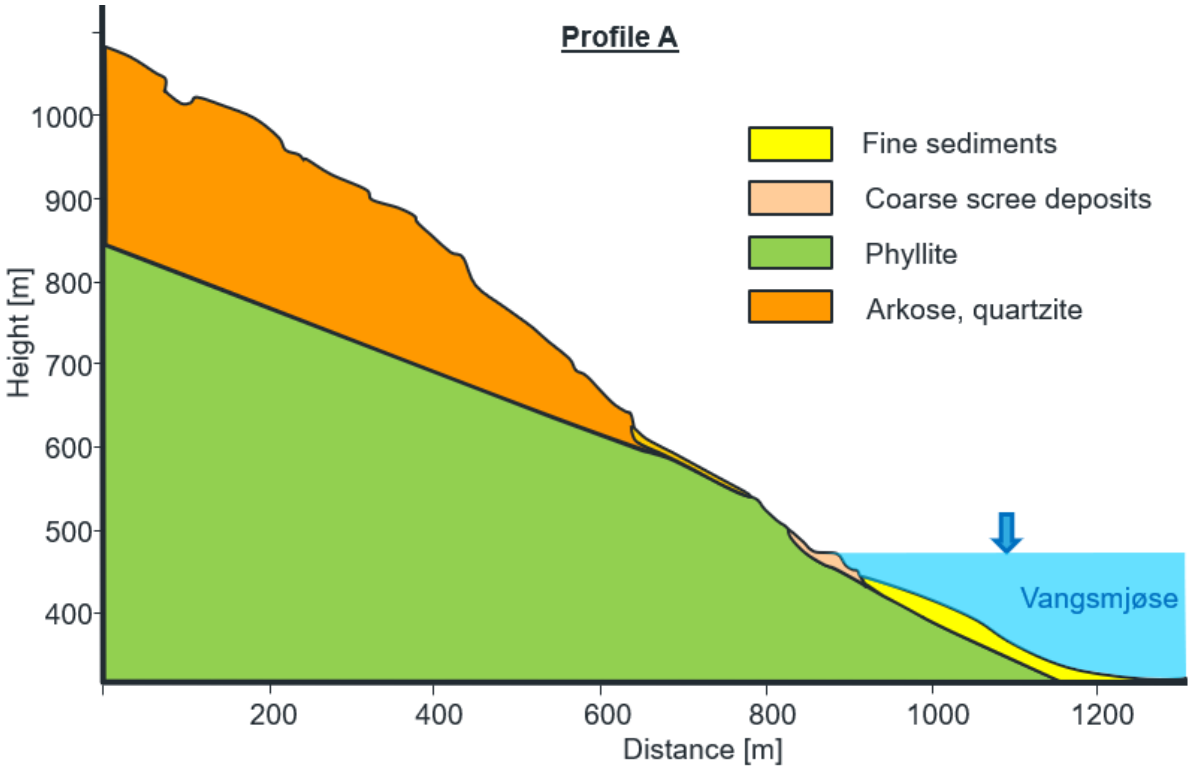

Figure 24) Lithological profile of Skutshon on the line A (see figure 4 and 8 for position).

4.2.2 Structural geological model of Skutshorn

Field-based structural measurements of the foliation and joints were evaluated as structural plots on a map to identify spatial variability in the orientation of structures. Through this approach, the

structural observations were grouped into domains with similar structural characteristics. Six different domains were established: upper east, upper central, upper west, central slide, phyllite, and dissected block in phyllite (Figure 25). In all domains, the orientation of the foliation and several joint sets clustered and distribute with statistical relevance around mean orientations. However, in all domains there are additional randomly distributed joint orientations.

Structural data from the frontal blocks and the SE face of the unstable slope were extracted from high resolution photogrammetric elevation models constructed from helicopter and UAV photos, respectively (Figure 25 for position). These were not incorporated into the structural domains identified from field data as the photogrammetric models are blind to structures that do not have a surface expression and the classification of structures is more uncertain. A structural and kinematic analysis is therefore incomplete for those locations, and structures are therefore described for those sites independently of the domains. In addition, subjective observations were made along the frontal blocks from helicopter and documented with photos (see Figure 25 for locations).

The largest structural variability between domains is seen in the foliation data (Table 5), the penetrative structure on which sliding is most likely to occur. The foliation only strikes approximately parallel to the slope in the phyllites (Figure 26 A), except for one dissected block that is cut by the road. In this domain the foliation shows an average dip direction and dip of 204/25 but, in some areas, is even flat or inclined into the slope. At the dissected block the foliation dips towards the east at an angle of ~25 degrees. In the central slide area domain (Figure 26 F), and western upper slope (Figure 26 E) the foliation varies from the strike of the slope by an average of ~ 20 degrees. In the western upper slope the foliation shoes two statistically relevant mean directions, and is thus plotted as Sf1 and Sf2, with one having horizontal attitude and the other inclining obliquely out of the slope (Table 5, Figure 26E). This indicates that the foliation is folded here, an observation also reported by Heim and Schärer (1977). In the eastern upper slope domain, the dip direction of the foliation deviates from the slope direction by ~40 degrees on average. In this domain, the foliation dips almost to the east with a wide spread of inclinations. In the upper central domain, the foliation shows a mean inclination of 031/23 into the slope and is folded with near horizontal inclinations to steep inclinations into the slope (Figure 26 D). In the central slide domain, the foliation dips obliquely out of the slope at 202/43 in a SSW direction (Table 5). This direction is parallel to the potential sliding surface of a possible earlier event and the lower limit of the disintegrated rock mass (see chapter 2.4, Figures 10 and 12).

Six joint sets (J1 to J6) could be identified in the field data (Table 5), however, not all of them could be observed in all domains. The most frequent joint set is J2, which was observed in five of the six domains, while J1 and J4 have been observed in three domains, and J5 in three domains. Joint set J3 was only observed in the upper east domain, and joint set J6 in the central slide area. Most of the joint sets (J1, J2, J3, J4, J5) are almost vertical or steeply inclined, while joint set J6 is inclined 31 degrees towards the north and thus dips into the slope.

The joint set J3 strikes parallel to the WNW to WSW striking portion of the back scarp (see chapter 2.4 and Figures 10, 11, and 12), while joint set J1 strikes in a 20-degree angle with the WNW-ESE striking portion of the back scarp. Therefore, these joint sets define the limits of the main slide body.

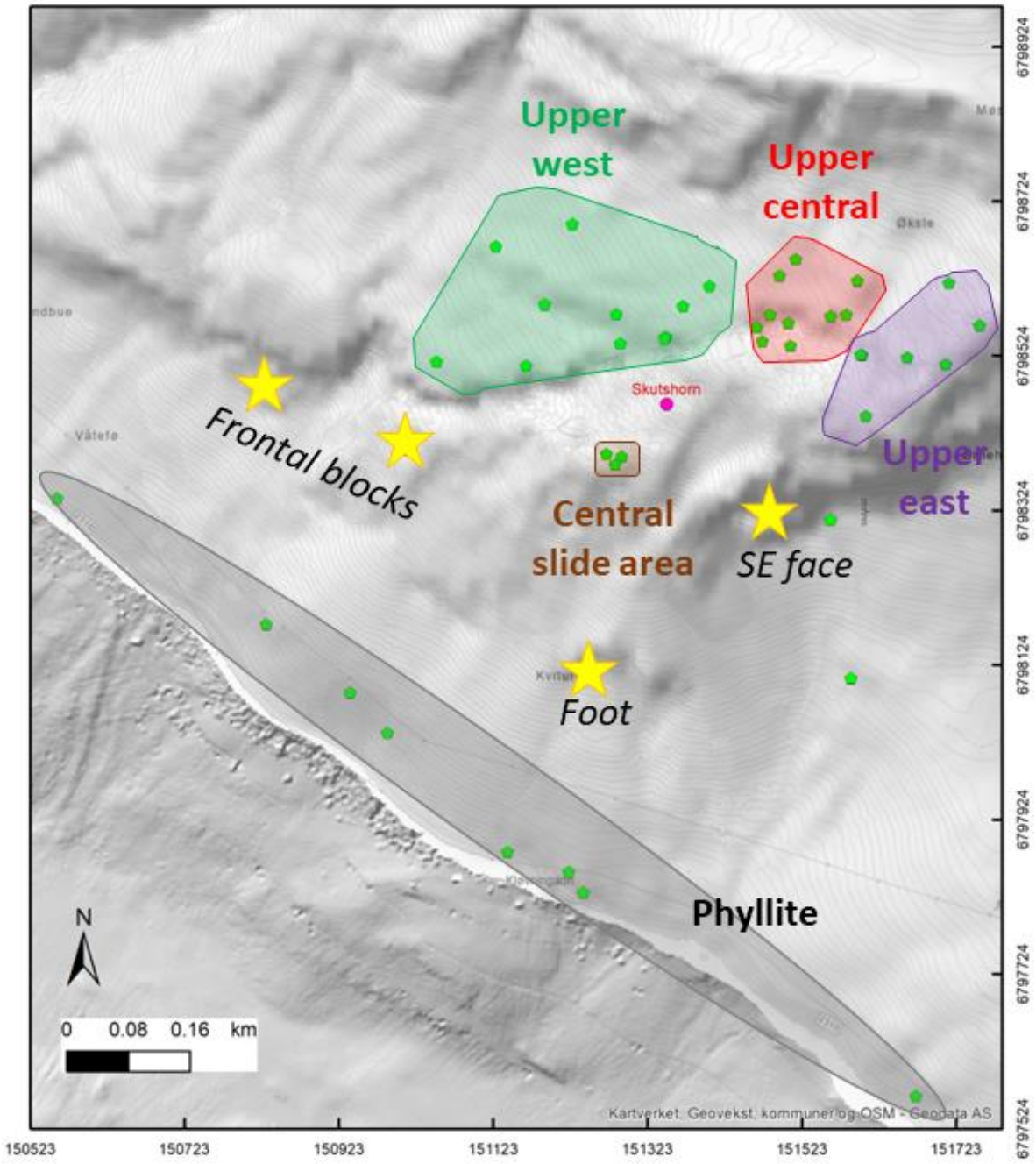

Figure 24) Grouping of structural observations based on structural similarities. In addition are localities shown where structural data were acquired from high resolution topographic data acquired by photogrammetry (Frontal blocks, SE face) and where structural observations were taken from helicopter by eye.

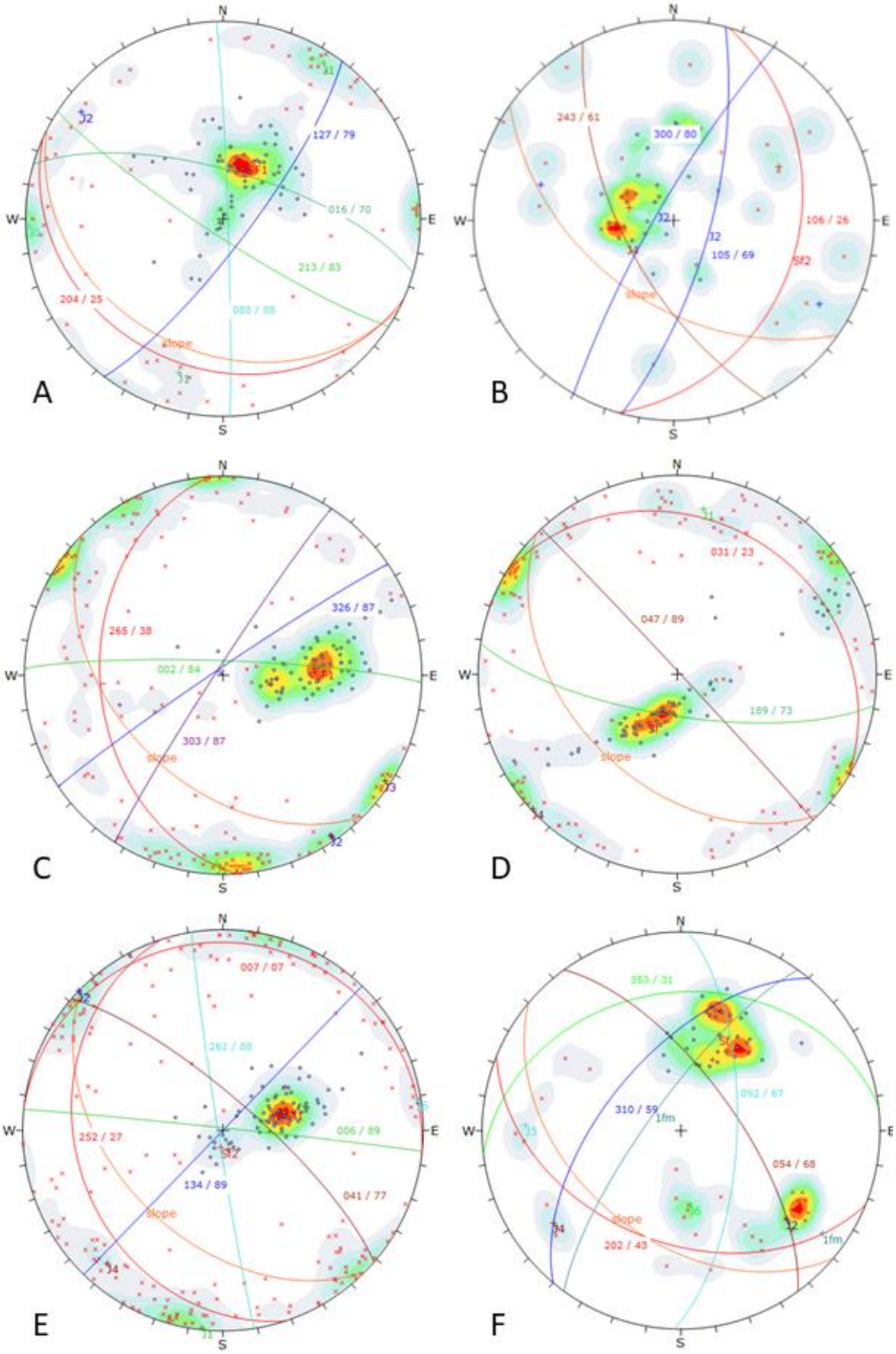

Figure 26) Structural analysis showing joint directions (black dots) and joint directions (red X) for the A) phyllite, B) frontal slide area, C) the eastern upper slope, D) the central upper slope, and E)

for the western upper slope, F) the central slide area. Plots are in lower hemisphere, equal area stereo nets. Data are summarized in Table 5.

Table 5) Structural domains characterized on the slope and orientation of the foliation and joint sets observed in these domains. (See the distribution of the measurements in Figure 25 for each domain.

Structure	Structural domain					
	upper east	upper central	upper west	central slide area	phyllite	dissected block
Sf(1)	265 /38		252 /27	202 / 43	204 / 25	
Sf(2)		031 / 23	007 /07			106 / 26
J1	002 / 84	189 / 73	006 / 89		213 / 83 **	
J2	326 / 87		134 / 89	310 / 59 *	127 / 79	300/80 - 105/69
J3	303 / 87					
J4		047 / 89	041 / 77	054 /68		243/ 61
J5			261 / 88	092 / 67 *	088 / 88	
J6				353 / 31		

** This joint set has the same direction however is 20 - 30 degrees less inclined*

*** This joint set is interpreted as having a wider spread in dip direction and the structural analysis split this set statistically in two separate sets one dipping 218/83 the other dipping 016 / 70*

Fewer structures were observed on remote sensing data, with three or four structures identified at each location (frontal slide block and SE face) (Figure 27 A and B respectively). As field observations on those steep and almost vertical slope sections were not possible, the type of structure is interpretative and documented with photos (Figure 27 C and D). At both locations the foliation could be identified. In the frontal blocks the foliation is almost vertical, and in the SE face it is ~45 degrees inclined to the south. J2 could be recognized in both data sets and J1 in the SE face. In the frontal slide blocks, there is an almost surface parallel structure with long persistence that was not recognized elsewhere, which is interpreted as an exfoliation joint.

Photographic observations were also carried out from helicopter along the SW tip of the back scarp and the foot of the arkose, quartzite (Figure 28). The foliation was again identified and show a similar (near vertical) orientation to the frontal blocks. At the foot of the arkose / quartzite the foliation is folded and therefore partly steeply dipping into the slope. In addition, almost vertical joints can be seen at both locations. One of those is interpreted to be parallel to J2.

Table 6) Structural data extracted from photogrammetric models for the frontal slide blocks. (See the distribution of the measurements in Figure 26 for each location.

Structure	Structural domain	
	Frontal blocks	SE face
Sf(1)	207 / 86	179 / 46
Exfoliation	210 / 52	
J1	002 / 84	224 / 90
J2	321 / 90	138 / 86

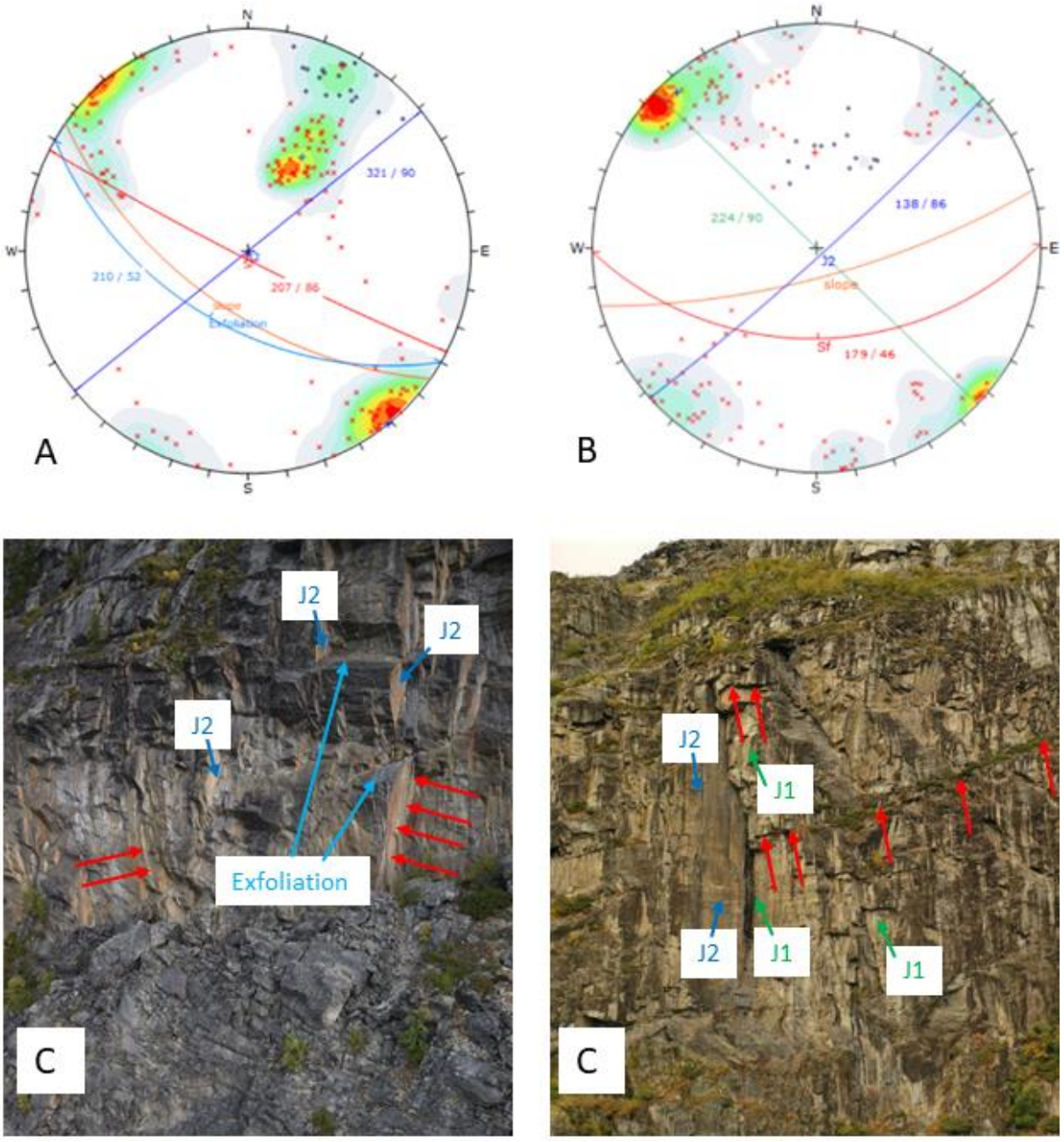

Figure 27) Structural analysis based on photogrammetric models showing interpreted orientation of foliation (black dots) and joint directions (red X) for the A) the frontal slide blocks, B) the SE face. The interpretation on the type of structures is based interpretative and documented on photos C) frontal slide blocks, D) SE face. On the photos C and D is the trace of the foliation marked with red arrows and structures with surface expression are labelled. Data are summarized in Table 6. (See figure 25 for location.)

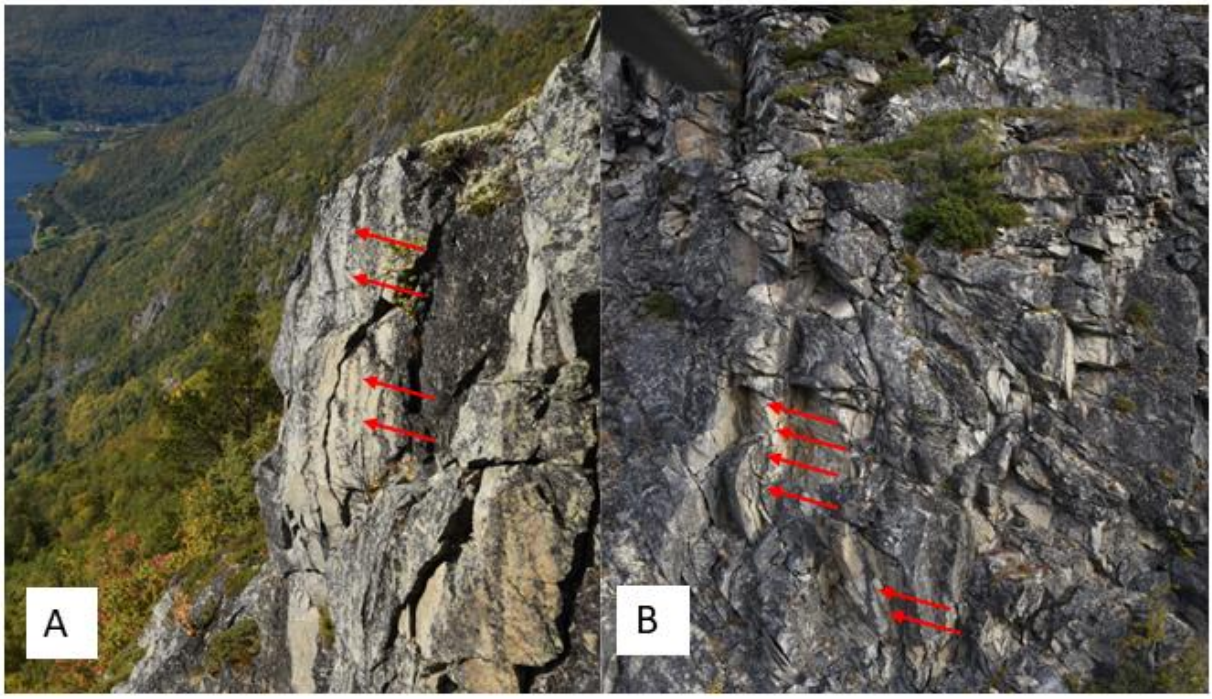

Figure 28) Structural observations from helicopter of A) the SW tip of the back scarp and B) the foot. The trace of the foliation marked with red arrows. (See figure 24 for location).

The above observed structural observations are summarized in two schematic structural profiles, A and B (see figure 4 for position), as shown in Figure 29. Profile A is drawn in downslope direction and profile B normal to the foliation. As most joints are near vertical, they are only shown as vertical. The profiles show similar structure features, with the main difference being that the foliation dips steeper on profile B than on profile A.

4.2.3 Kinematic analysis of the unstable rock mass

The structural measurements were used to make a stability assessment in form of kinematic tests for failure feasibility considering different movement types (planar sliding, wedge sliding, toppling). Planar and wedge sliding are most relevant mechanism for the failure of large volumes (e.g. Hungr et al., 2014) while toppling failures only rarely resulted in large failures of critical volume on slope scale of several million cubic meters (Nichol, et al., 2002). Most important are persistent structures. Those are the foliation and joint set J2 and, to a lesser degree, joint set J1. Those structures also delimit the main slide body. Important to evaluating a failure mechanism is how those structures relate to the slope orientation. As the foliation is highly variable over the slope, the kinematic analysis was carried out separately for each structural domain. Kinematic plots of planar sliding and wedge sliding failure are shown in Figure 30 and all kinematic tests are summarized in Table 7 and 8. For the kinematic test of the upper domains the slope angle was set to 45 degrees which represents the average slope angle there, while the average slope angle was set to 60 degrees in the frontal slide blocks and to 75 degrees in the SE face. In the phyllites the slope angle was set to 33 degrees as the terrain is shallower here. A friction angle of 30 degree for the arkose / quartzite

was used as typical for hard metamorphic rocks and 25 degrees for the phyllite for metamorphic rocks that may contain clayey material. Those friction angles follow standard tables (Wyllie and Mah, 2004).

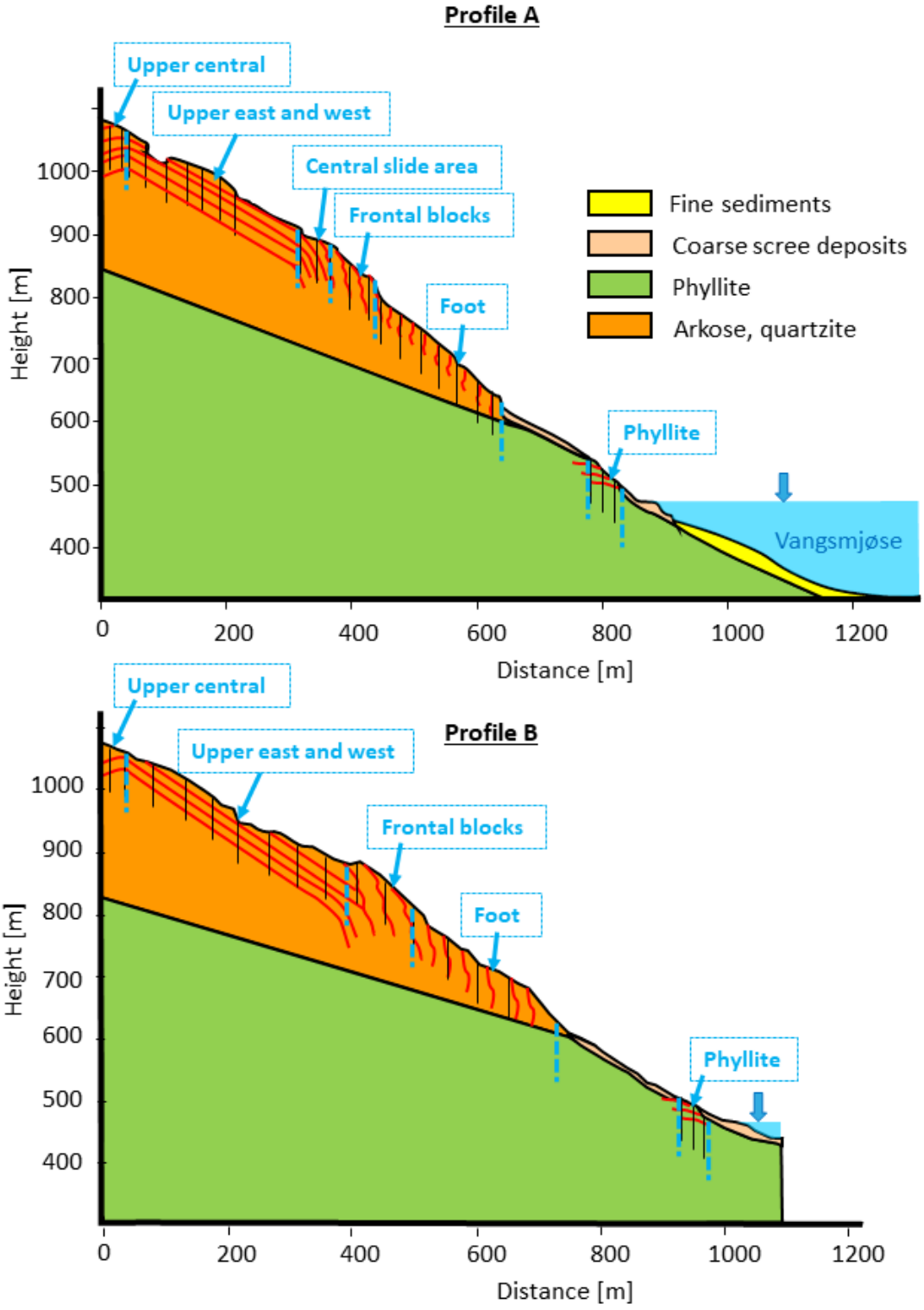

Figure 29) Schematic structural profiles showing the structural observations summarizing the structural observations from Figure 26 to 28 and Tables 5 and 6. Structural domains are indicated and their limits suggested.

Planar sliding is kinematic partially feasible on the foliation in all domains except the upper central structural domain. Sliding on the foliation is only partially feasible because the foliation often dips on average obliquely to the slope direction by 20 to 40 degrees. In the frontal slide blocks and on the SE face planar sliding is fully feasible on the exfoliation or foliation, respectively, owing to the steeper slope angle in these locations. Based on helicopter observations, the foliation changes dip angle towards the front and foot of the slide mass and becomes almost vertical. Thus, it is not daylighting and planar sliding will not be feasible in this frontal part.

Wedge sliding is feasible on the intersection between the foliation and all joint sets in the upper east structural domain, on intersections between the foliation and joint sets J1 and J2 in the upper west structural domain and in the phyllites, and between the foliation and J2 and J5 in the central slide domain. Wedge sliding is also possible in the frontal slide blocks and on the SE face. Wedge sliding is unlikely in the upper central domain and is only feasible on randomly distributed joints. Similar to planar sliding, wedge sliding is not feasible in the front and foot of the unstable mass where the foliation is not daylighting, because the foliation is the most important structure that forms the wedge with the joints in all other domains.

Flexural toppling and direct toppling are feasible in all domains except the central slide domain and the phyllites. As mentioned above, however, this failure mechanism rarely leads to failures on the scale of the Skutshorn instability but is a typical release mechanism for smaller size volumes.

Table 7) Kinematic feasibility tests for structural domains based on field data.

	Slope angle	Planar sliding	Wedge sliding	Flexural Toppling	Direct Toppling
Upper east	225 / 45	6.2 %	8.3 %	5.1 %	14.5 %
		on Sf	all intersections with Sf	on J1	all J on Sf
Upper central	225 / 45	0.5 %	1.4 %	10,5 %	6,7 %
				on J4	Intersection on Sf
Upper west	225 / 45	6.6 %	5.4 %	10. 2 %	24 %
		on Sf	on Sf 1 and J1, J2	on J4 and J1	Intersection on Sf
Central slide	225 / 45	12 %	22 %	0 %	0,7 %
		on Sf	on Sf and J2, J5		on Sf
Phyllite	205 / 33	9 %	8.5 %	2.3 %	2,0 %
		on Sf	on Sf and J1, J2	on J1	Intersection on Sf
Phyllite	205 / 33	0 %	0.5 %	0 %	1,2 %
Dissected block		on Sf	on Sf and J1, J2	on J1	Intersection on Sf

Table 8) Kinematic feasibility tests for data compiled from photogrammetric models.

	Slope angle	Planar sliding	Wedge sliding	Flexural Toppling	Direct Toppling
Frontal bocks	215 / 60	28 %	40.5 %	29 %	9 %
		on Sf	on Sf and J2	on J1	J1 on exfoliation
SE face	165 /75	12 %	25.6	12 %	18.6 %
		on Sf	all intersections with Sf	on Sf	Intersection on Sf

Planar sliding

Wedge sliding

Upper east structural domain

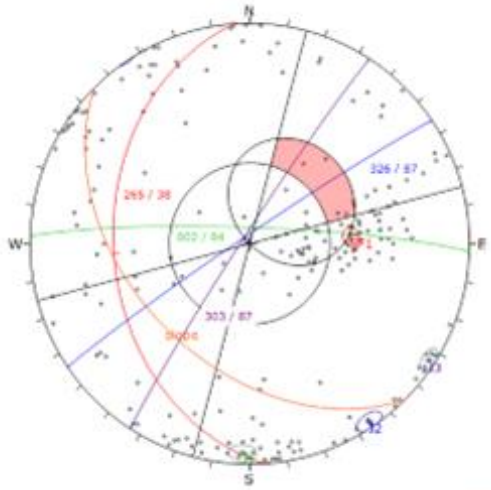

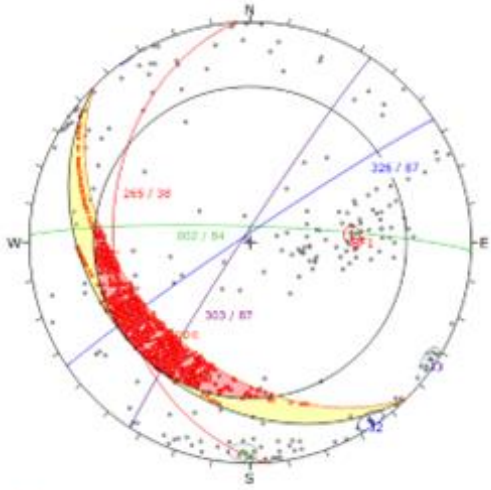

Upper central structural domain

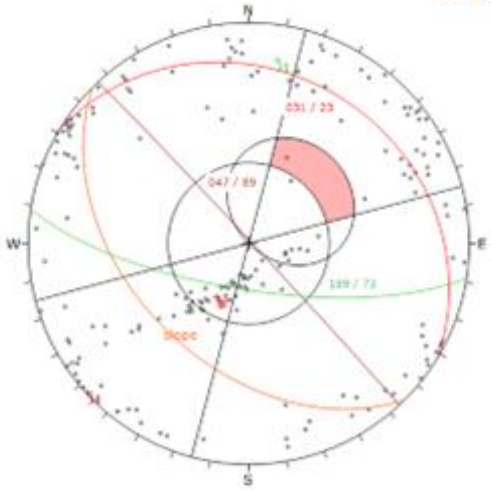

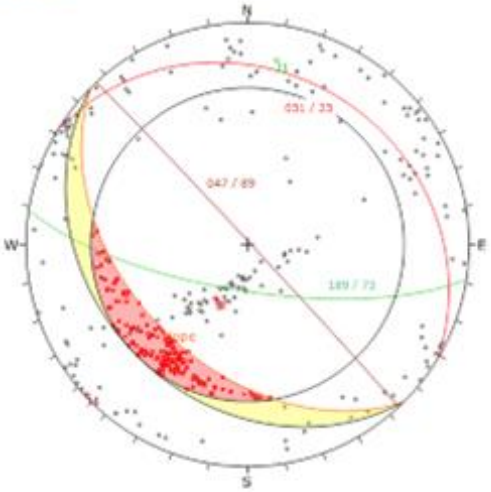

Upper west structural domain

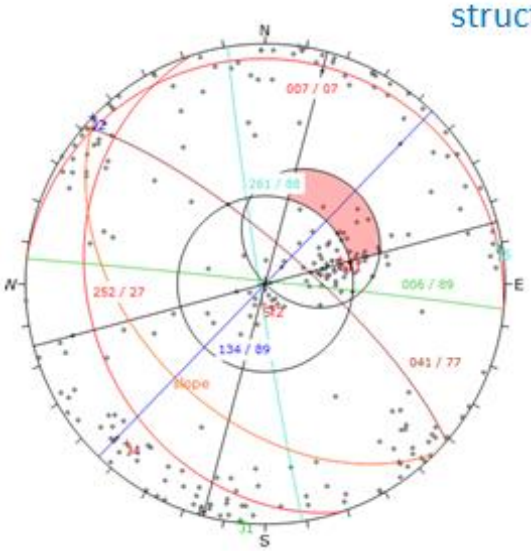

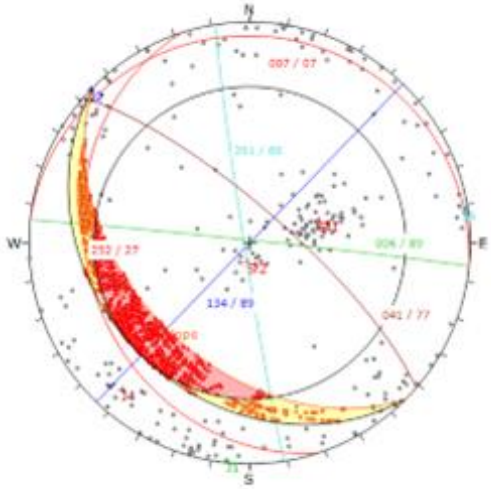

Planar sliding

Wedge sliding

Central slide
structural domain

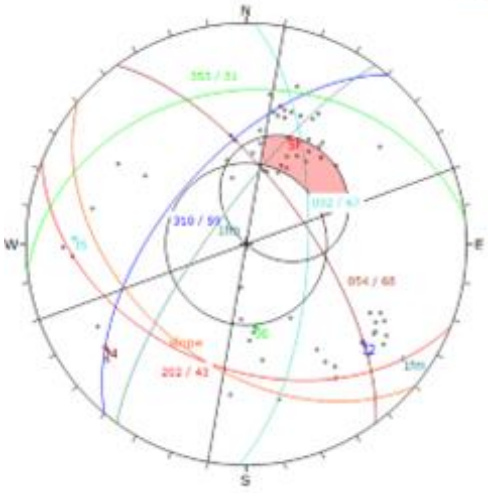

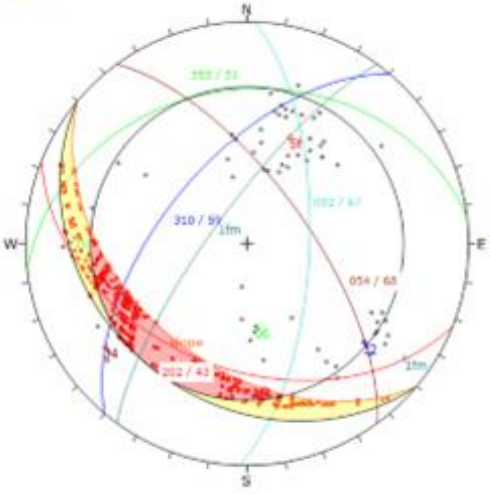

Phyllite
structural domain

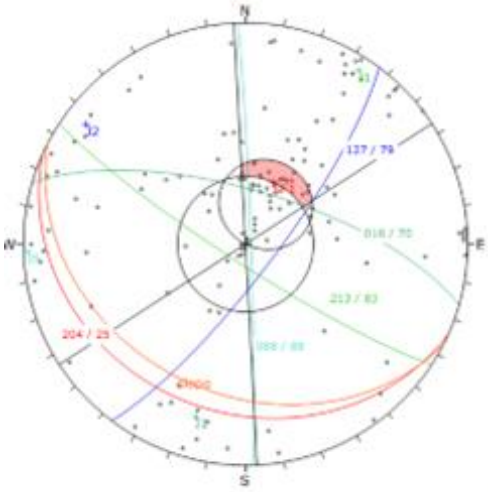

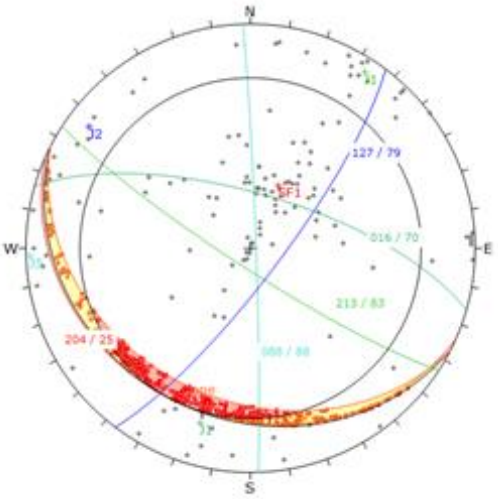

Phyllite
Dissected block

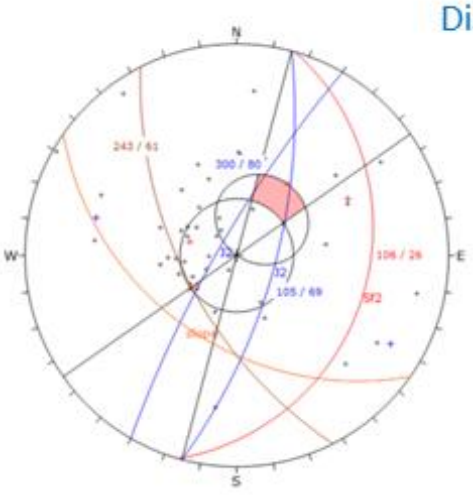

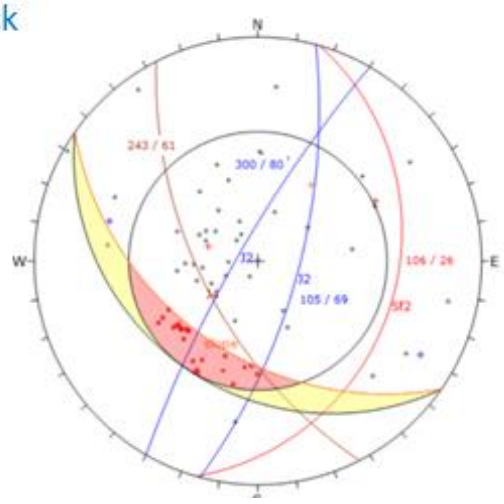

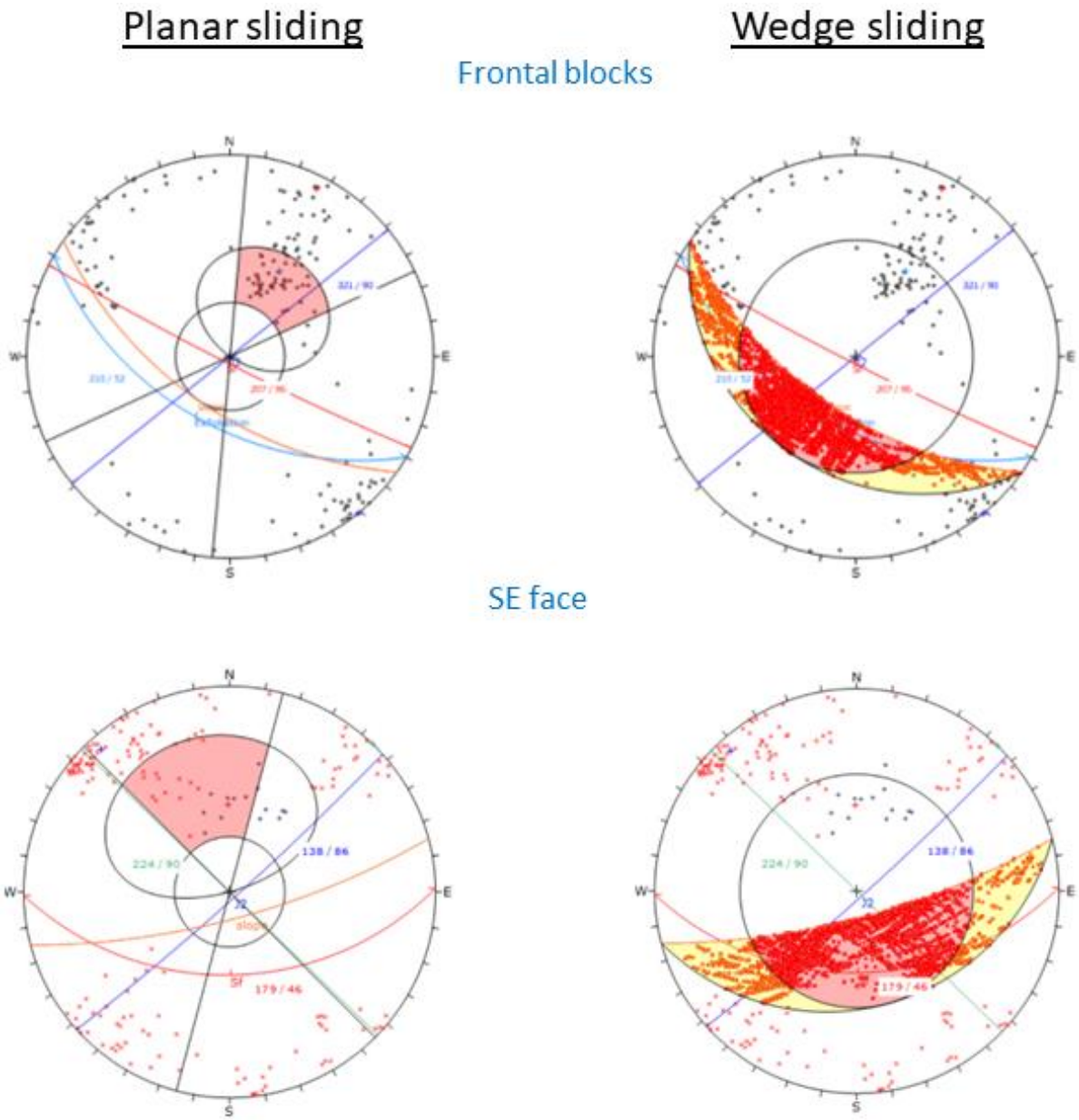

Figure 30) Kinematic feasibility test for planar and wedge sliding for all defined domains and the areas analysed with photogrammetric data. Plots are in lower hemisphere, equal area stereo nets. Data are summarized in table 6.

4.3 Deformation rates at Skutshorn

Deformation rate data exists for point observations through dGNSS measurements of bolts installed on the rock slope and reflectors installed for InSAR from satellites. Deformation rate data covering large surfaces data exists in the form of GB-InSAR and satellite based InSAR.

4.3.1 Deformation rates based on dGNSS

dGNSS data are summarized in table 9 and those with significant movement shown in Figure 31 and 32. The results are partly variable from year to year (Appendix 1), with point SKUT_GPS_02 moving in the horizontal but not in the vertical vector and point SKUT_GPS_03 moving up in some

years while down in other years. Points SKUT_GPS_05 and SKUT_GPS_06 have only moved upwards since installation. This behaviour is best explained by processing challenges owing to the relatively long distance between the site and nearest weather station, and variable weather conditions experienced during field measurements over serval years.

The measurement point SKUT_GPS_01 shows no deformation over the four years measurements and can be considered stable. All measurement points within the main slide body (SKUT_GPS_02, SKUT_GPS_03, SKUT_GPS_04, SKUT_GPS_09, SKUT_GPS_10) have significant displacement in the vertical and in the horizontal after the four years measurement period and a movement direction in the dip direction of the slope. However, there is a difference in the amount of vertical and horizontal displacement among those locations with dGNSS points further to the southeast showing higher velocities than those further northwest (Table 9). 3D displacements are all above 1 cm/yr and below 3 cm /yr.

In the fractured, but relatively intact, area to the northwest of the back scarp (SKUT_GPS_05, SKUT_GPS_06) the displacement shows positive significant movement in the vertical and SKUT_GPS_05 also significant horizontal movement in upslope direction. These dGNSS locations, however, do not show a consistent movement trend after this period and the data are interpreted as reflecting stable rock. The upward movement again likely reflects processing difficulties owing to weather conditions during the measurement days.

Table 9) Results from dGNSS measurements (velocities in the horizontal (yellow), in the vertical (green), and in 3D (blue) are shown for measurement points with sigma 3 significance in Figure 31

GNSS point ID	SKUT_GPS_01	SKUT_GPS_02	SKUT_GPS_03	SKUT_GPS_04	SKUT_GPS_05	SKUT_GPS_06	SKUT_GPS_09	SKUT_GPS_10
Time in between first and last measurement	4	4	4	4	3	3	2	2
First measurement year	2018	2018	2018	2018	2019	2019	2020	2020
Last measurement year	2022	2022	2022	2022	2022	2022	2022	2022
*** Least squares (unweighted, constrained to 0 for the first measurment) ***								
Average E-W displacement [mm/year]	0.1637	-7.9828	-8.2498	-14.0279	4.239	-1.055	-7.6166	-6.9001
Standard deviation	0.1784	0.0529	0.1367	0.1572	0.4677	0.5369	0.5137	0.0231
R^2	0.1036	0.9995	0.9966	0.9985	0.9078	0.3513	0.9784	0.9999
Average N-S displacement [mm/year]	0.3557	-12.5048	-16.6893	-17.8216	3.8633	-0.4518	-9.5536	-7.3247
Standard deviation	0.1027	0.2095	0.4049	0.1249	0.5796	0.4383	0.613	0.089
R^2	0.5115	0.9965	0.9928	0.9994	0.8425	0.1646	0.9804	0.9993
Average horizontal displacement [mm/year]	0.3916	14.8356	18.617	22.6802	5.7353	1.1477	12.2181	10.0629
Standard deviation	0.0431	0.2062	0.4072	0.194	0.7152	0.5872	0.7996	0.0804
R^2	0.9323	0.9976	0.9941	0.9991	0.8857	0.4107	0.9797	0.9997
Average vertical displacement [mm/year]	0.5007	-16.0888	-6.6663	-17.0234	5.86	9.5656	-11.0903	-7.0528
Standard deviation	0.68	1.2134	1.0762	0.577	1.4701	1.3514	0.1819	0.6615
R^2	0.0863	0.9347	0.7607	0.986	0.6653	0.858	0.9987	0.9592
Average 3D displacement [mm/year]	0.6356	21.8848	19.7746	28.3582	8.1996	9.6342	16.5008	12.2884
Standard deviation	0.509	1.0949	0.4708	0.4084	1.5758	1.4366	0.7246	0.4186
R^2	0.3525	0.9702	0.9931	0.9974	0.7699	0.8456	0.9907	0.9944
Movement trend	37.3175	212.5355	206.2764	218.2103	47.4669	247.7107	218.5753	223.2839
Standard deviation	16.0827	0.3723	0.4848	0.2095	3.8825	15.3647	0.1488	0.4751
Movement plunge	-49.899	47.4142	19.4953	36.8907	-46.7975	-79.5021	42.0476	35.0616
Standard deviation	48.4603	3.8383	3.6139	1.4146	7.1703	54.8231	2.5271	3.4409

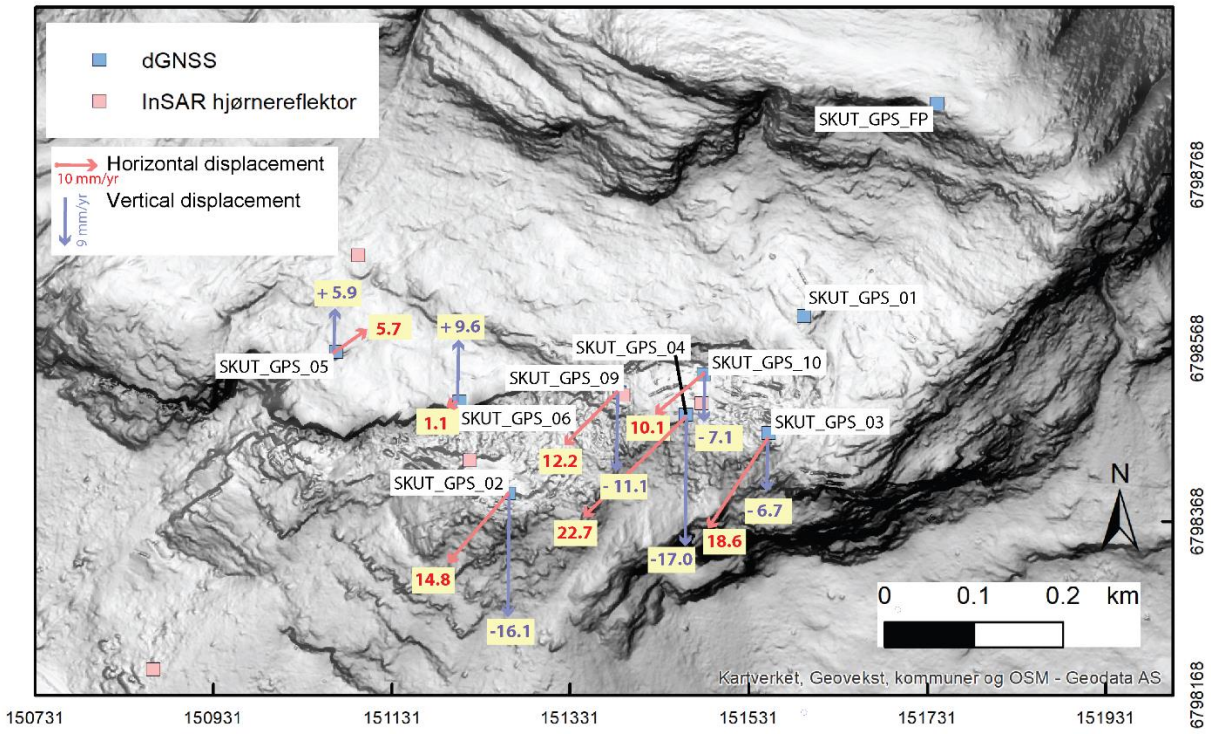

Figure 31) dGNSS displacement vectors horizontal (red) and vertical (blue) plotted on location of the installed bolt. See Table 10 for statistical information on measurements.

The measurement points SKUT_GPS_07 and SKUT_GPS_08 (Figure 14) were only measured in two intervals. While the first-year measurement interval indicated significant movement, this was almost reversed in the following year (SKUT_GPS_08) or has a strong change in direction (SKUT_GPS_07), and thus suggests the movement is or may not be significant (Appendix 1).

4.3.2 Deformation rates based on corner reflectors (CRs)

CRs do not show the total velocity of the point where they are installed but the component that is parallel to the line of sight from the satellite. With a SW-oriented slope the view direction from the descending satellites is almost parallel with the slope direction. Thus, we can assume that a large component of the real displacement is detected. Three of the CRs (SK-SAT-2, SK-SAT-3, and SK-SAT-4) can be observed from 3 flight paths of the satellite (Figure 33), while SK-SAT-5 can be observed only from one of the satellite paths. SK-SAT-3, and SK-SAT-4 and SK-SAT-5 are located close to the installed dGNSS bolts within the main deformation part within the arkose/quartzite (see Figure 14). SK-SAT-2 is installed on the small phyllite outcrop surrounded by scree depots in the lower part of the slope.

The flight path showing the highest deformation rate is closest to the real velocity. The velocity data shows some noise (Figure 33) due to atmospheric conditions during measurements that cannot be fully corrected. Noise is typically highest in wintertime and attributed to snow/ice cover on the reflectors. Considering that the CR velocities are minimum velocities, they correspond well with the

deformation rates recorded at nearby dGNSS bolts. SK-SAT-2 shows an average velocity of about 1 cm/yr.

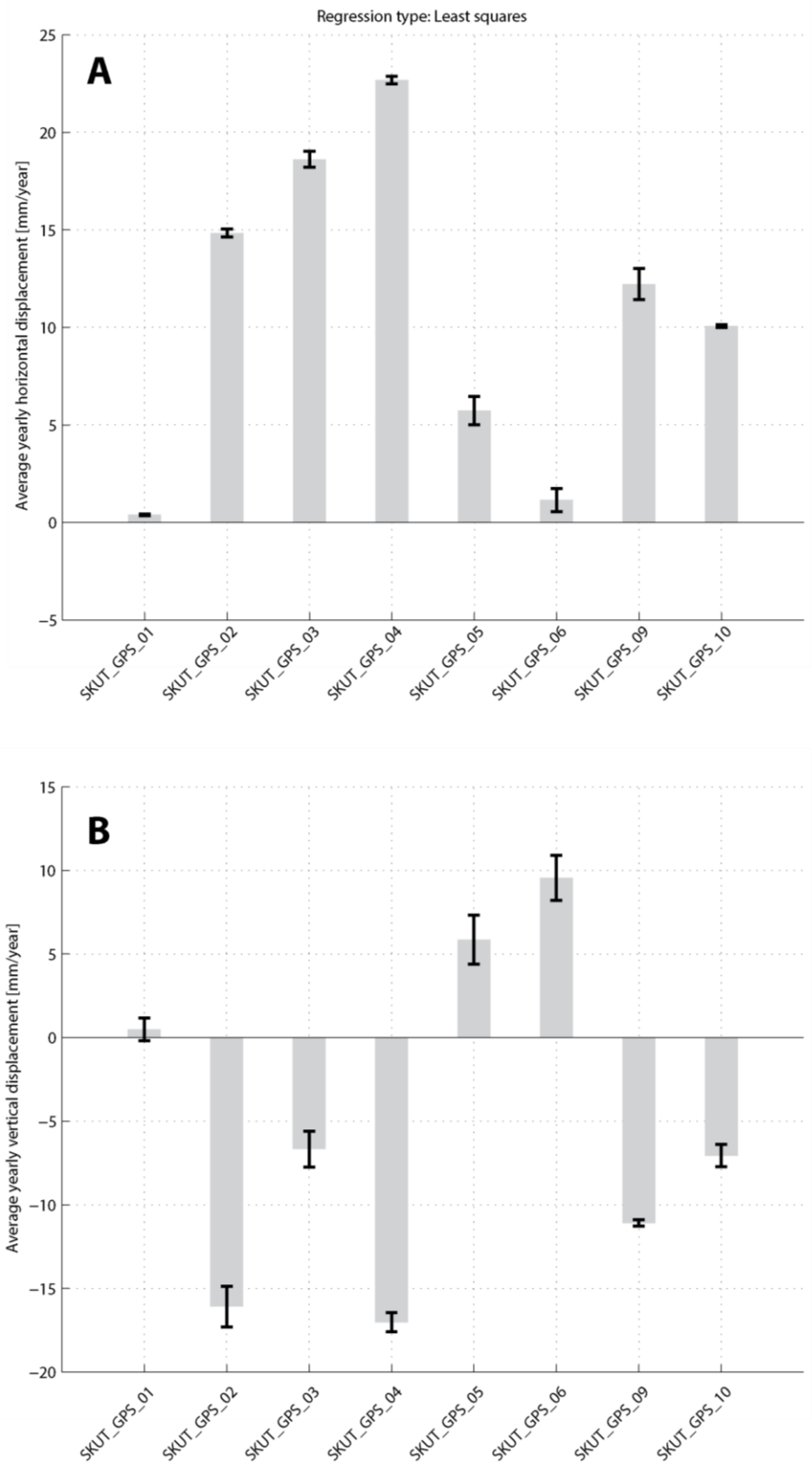

Figure 32) dGNSS displacement vectors horizontal (A) and vertical (B) plotted as histogram. See Table 10 for statistical information on measurements.

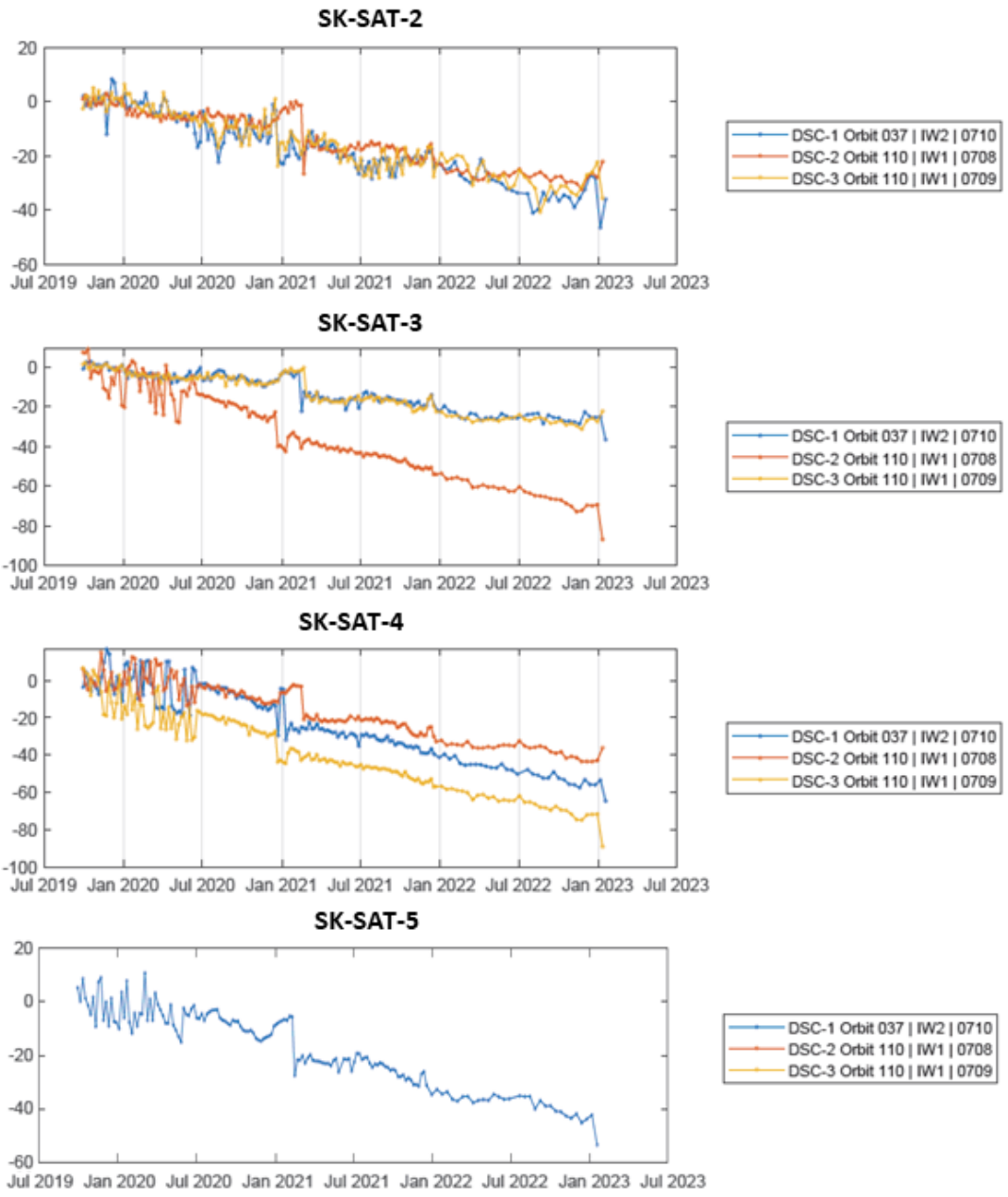

Figure 33) CRs velocity graphs in with y axis (mm) and x axis time. See Figure 14 for position of CR reflectors. The three different colours represent measurements from 3 different satellite orbits.

4.3.3 Deformation rates based on GB-InSAR

Line-of-sight velocity (see radar position in Figure 17) measurements for the period 19th of July to 17th of August 2020 show surface displacement over most of the unstable slope (Figure 34). These data indicate that the backscarp is moving away from the scanner, however, these results are likely an effect of the atmospheric disturbance due to the necessity to scan over the lake, and the results rather suggest that the back scarp is stable. The main slide mass moved with a displacement of >1 to more >4 mm/month towards the lake over this period. The highest displacements are found close to locations where dGNSS also shows the fastest movements (SKUT_GPS_04 in Figure 31), with the monthly GB InSAR velocities, when extrapolated across a year, being slightly higher but in the

same order of magnitude as the dGNSS displacement rates. The central frontal part of the slide mass has displacements of 2–3 mm/month, while at the foot of the slide mass of the movements are slower at 1–2 mm/month. The scree deposit below the slide mass shows movement towards the scanner, particularly in the most active rock fall zone, at displacements >2 mm/month (see Figure 9 A for comparison). This is most likely not the slide movement, but the build-up of rock fall deposits on the scree deposit that is registered in the GB-InSAR data as movement of the surface towards the radar. However, large parts of the scree deposits are less active, including parts of the broken up phyllite, which is moving at >0 and >1 mm/month towards the radar and could represent real slide movement. The area exposed by rock fall interpreted as the sliding surface (Figure 12) indeed does not show deformation on the GB-InSAR data supporting the interpretation that it is the lower limit of the sliding rock mass.

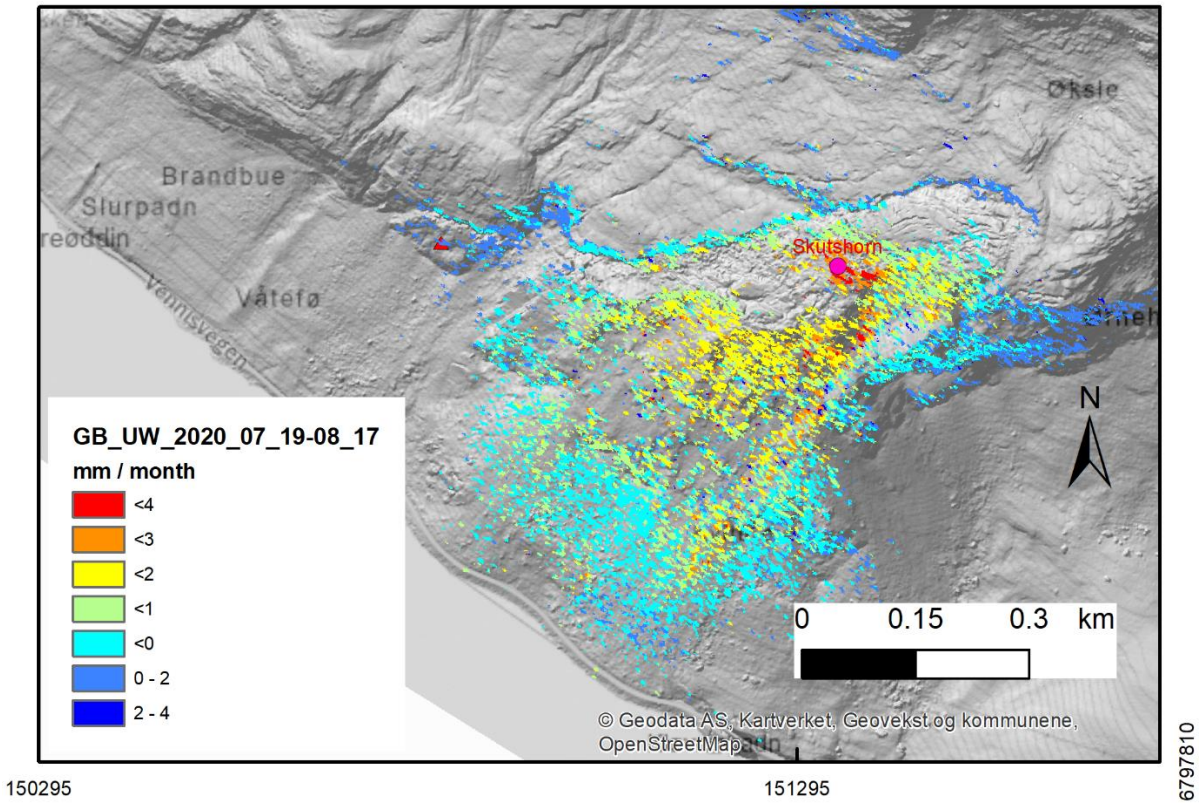

Figure 34) Velocity map of GB-InSAR results from the period 19-07-2020 to 17-08-2020 unwrapped data. See Figure 17 for position of radar.

4.3.4 Deformation rates based on satellite-based InSAR

Satellite track Descending 2 (see Table 1) has an incidence angle that is close to parallel with the slope direction and probably gives displacement estimates closest to the true rockslide velocity. Data from 2015-2019 were analysed using the online tool insar.ngu.no (see screen shot in figure 35) and displacements derived from areas with consistent movement rates and minimal noise (labelled A-H).

The highest displacements (34 mm/yr) were detected in the area labelled A, which is a transition zone between a larger intact block and an area where the rock mass is strongly fracturing in smaller units. Areas B, C, and D correspond to zones where the dGNSS bolts SKUT_GPS_03, SKUT_GPS_10, and SKUT_GPS_02 are installed, respectively, and the displacements are as expected slightly lower than in the dGNSS data as only the fraction of the displacement parallel to LOS is documented. Area D shows the displacement rate nearest to the rate recorded in SKUT_GPS_02 as the deformation vector at that location is closest to the LOS of the satellite. In areas E, F, G, and H no dGNSS bolts are installed. Area E and F represent the frontal blocks of the instability. While the eastern part of the frontal block (E) moves at 15.5 mm/yr, comparable with the main rockslide mass (measurement areas B, C, D), the western frontal block (F) shows a lower displacement of 4.5 mm/yr. The strongly fractured phyllite that protrudes from the scree deposits moves with a displacement of 11.5 mm/yr, while the fractured phyllite block to the east (H) moves with a displacement of only 3.5 mm/yr.

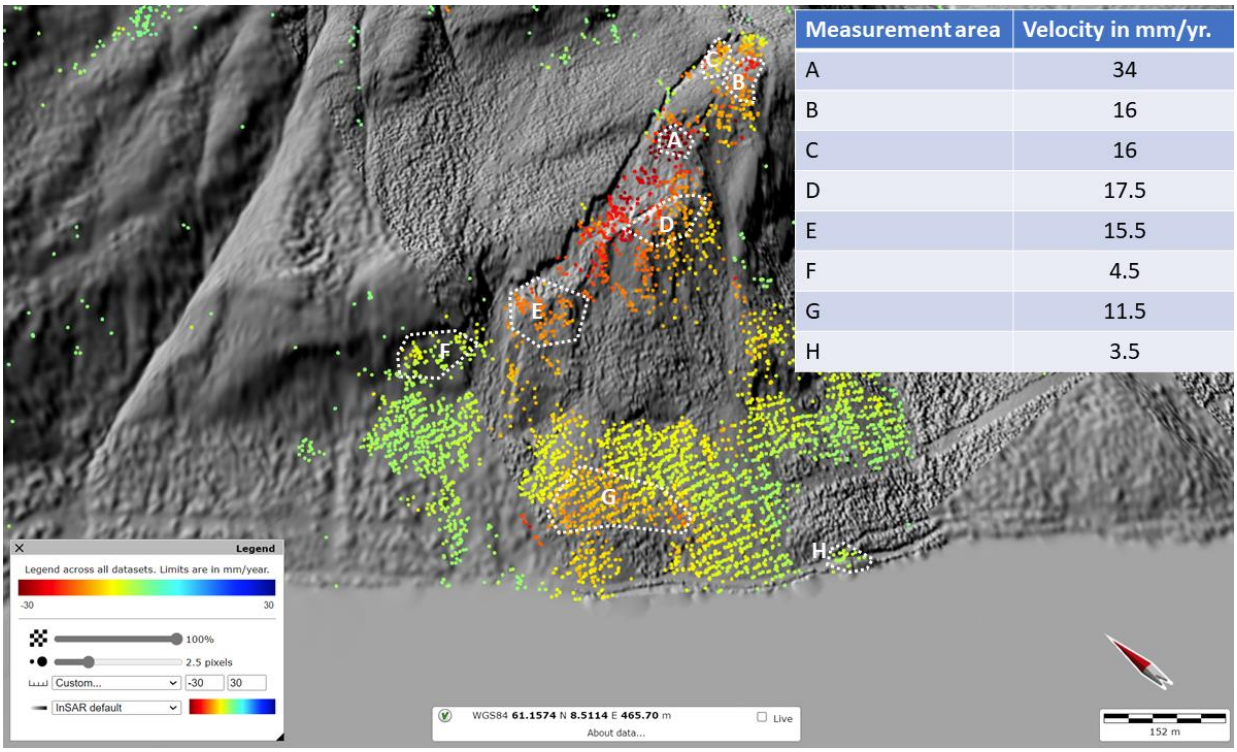

Measurement area	Velocity in mm/yr.
A	34
B	16
C	16
D	17.5
E	15.5
F	4.5
G	11.5
H	3.5

Figure 35) Screen shot from insar.ngu.no of a view over Skutshorn from the SW. Velocity represent descending data track 2 2015 to 2023 data.

4.3.5 3D deformation rates

3D decompositions of the ascending and descending tracks of satellite-based data in combination with the GB-based InSAR data was performed along two profiles (Figure 36).

The 3D decomposition of the three datasets indicates that deformation in the upper part is almost surface parallel, as the horizontal component is larger than the vertical component (Figure 37). This pattern changes in the mid-slope, where the vertical displacement is larger than the horizontal.

Further downslope in the scree deposits, the deformation vector becomes slope parallel again. When compared to 3D vectors from the dGNSS bolts (Figure 31) the deformation patterns are identical with respect to the angle of displacement.

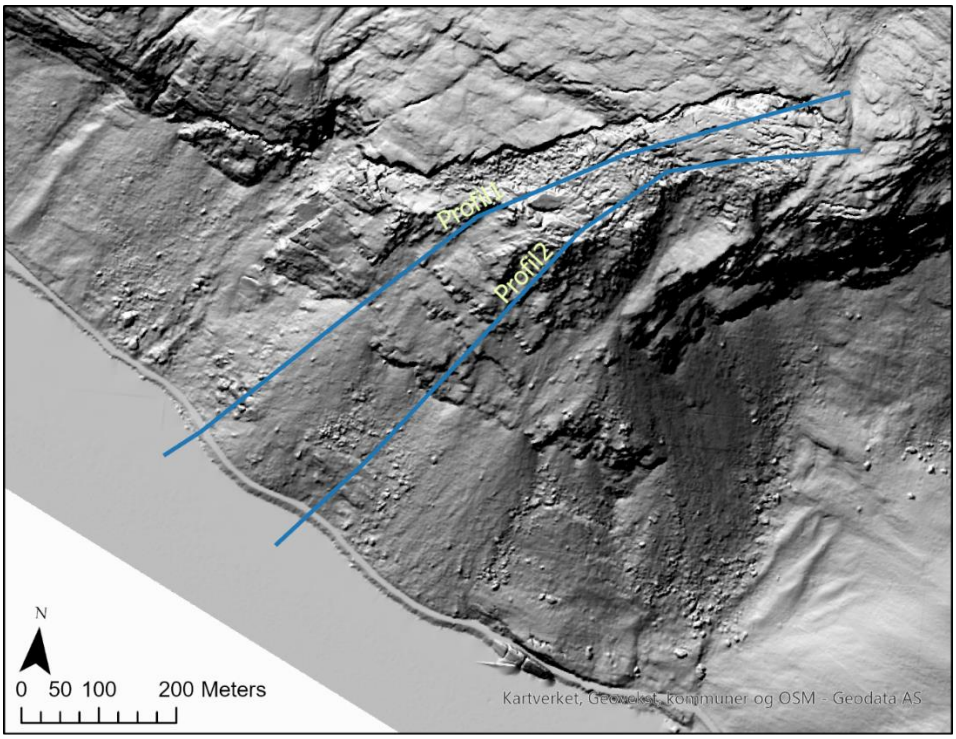

Figure 36) Profiles along which decomposition of satellite based InSAR data from ascending and descending track in combination with GB-based InSAR data was performed to calculate 3D vectors of deformation.

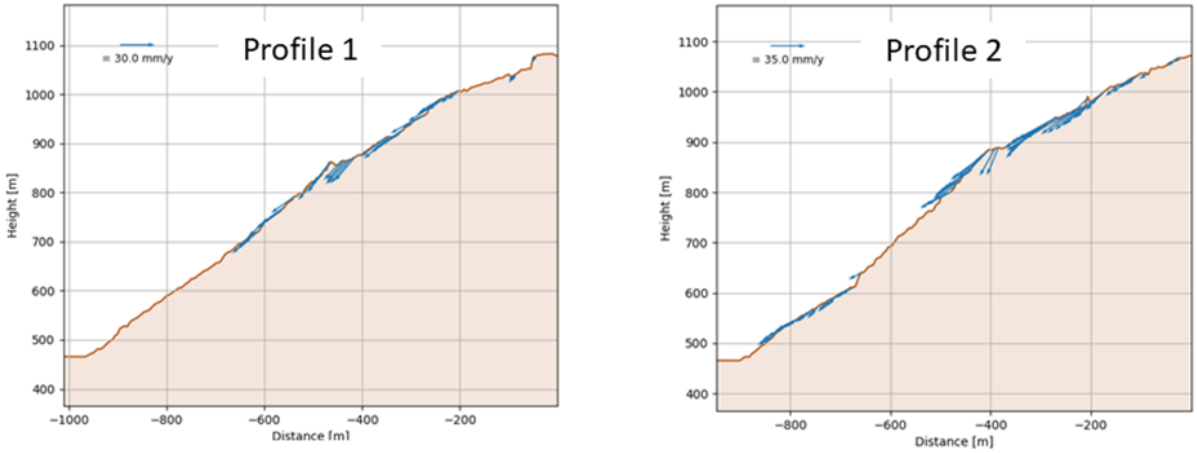

Figure 37) Profile1 and profile 2 see Figure 36 for location) showing 3D decomposed vectors obtained by combining ascending, descending satellite deformation data with GB-InSAR data. Deformation vectors are plotted in the plane of the profile.

4.4 Results from the ERT analysis

The ERT profile is 1200 m long and runs from just outside the scree field in the west to just outside the eastern side. The entire length runs along the gravel road, see Figure 19 for photo from field and Figures 38 and 39 for map and results.

The results show an upper surface of high resistivity running along the entire profile. These values distribute over a thickness of 20 meter and resistivity values vary from 5000 to 15 000 Ωm. The only exception is between 850 and 1000 meters where this zone is absent. There is instead a zone with values from 2500 to 6000 Ωm that extends from surface to the bottom of the profile. Below the 20-meter-thick zone is a low resistivity zone with values between 700 and 2000 Ωm. This zone is roughly 50 meters thick and rests upon a high resistivity zone with values between 2500 and 4000 Ωm.

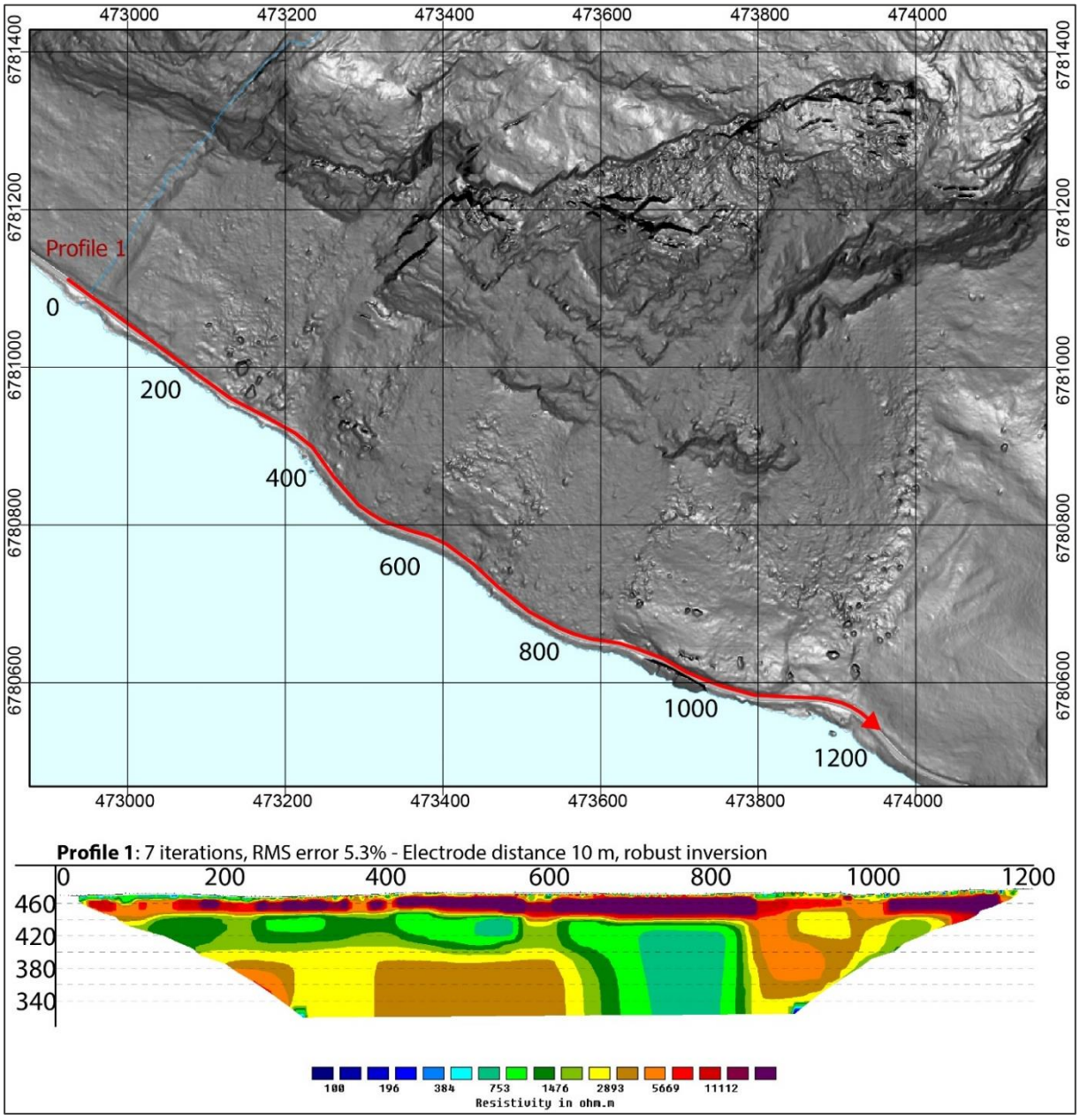

Figure 38) Map showing the location of and inverted ERT profile.

The upper high resistivity layer is interpreted as mainly representing the scree deposits (Figure 39). This zone runs along the entire profile except certain zones where “pillars” of fractured bedrock stand out between the scree, for example, at the dissected phyllite block cut by the road (see also Figure 6 between 850 and 1000 meters profile length). This 150-meter-wide zone has lower resistivity than the dry scree deposits, but higher resistivity than the water saturated fractured bedrock below the scree deposits. This zone dominated by fractured bedrock is roughly 20 meters below the surface (characterized by 700 to 2000 Ωm). This layer rests on a layer of high resistivity (2000 to 6000 Ωm) typical for dry bedrock for the first 600 meters of the profile, however between 600 and 850 meter this is absent. The selected processing method of the data overrepresents vertical signals, so the boundary is not necessarily that sharp. There is no evidence of a sliding surface in a graphitic layer in the ERT profile, as observed at other unstable slopes in phyllite in Norway (Tassis and Larsen., 2021) which would be marked by very low resistivity values. Therefore, does the ERT profile neither prove or disprove a sliding surface.

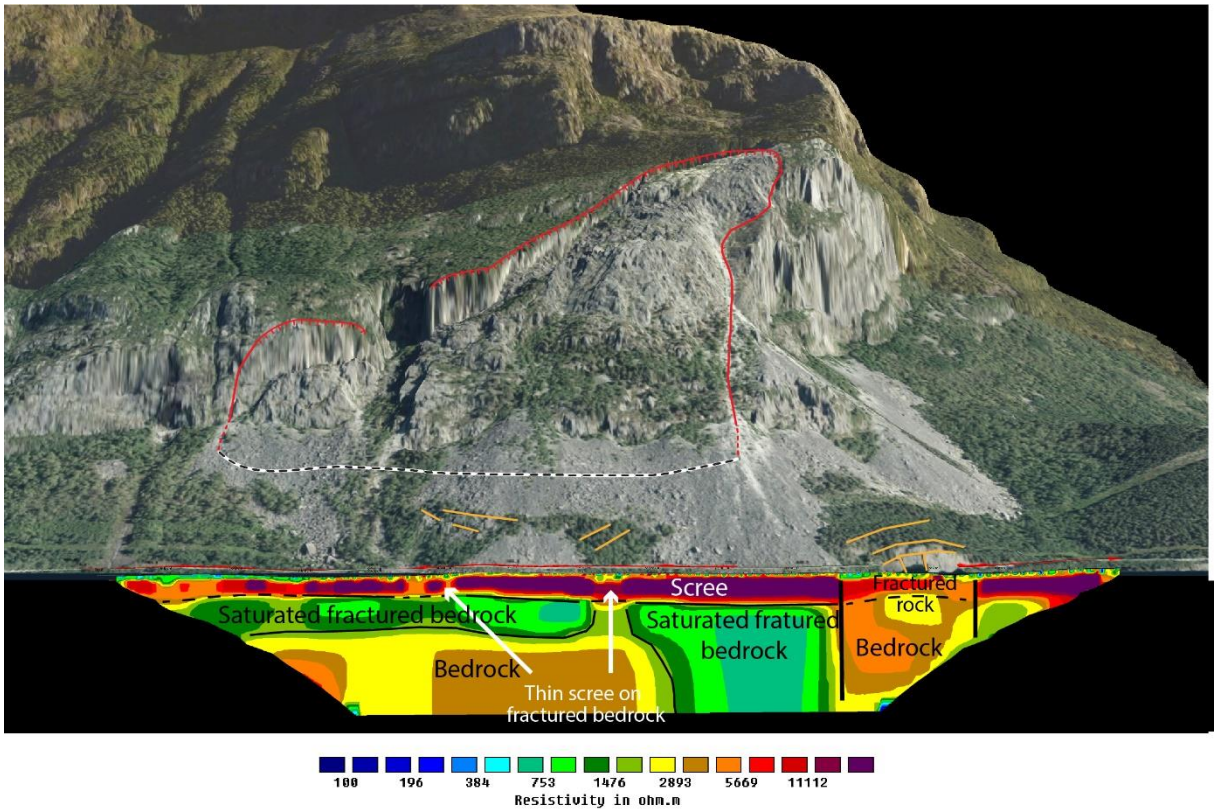

Figure 39) Inverted ERT profile drawn along the road at the foot of Skutshon with the interpretation of the different resistivity values.

4.5 Geological model of the Skutshorn unstable slope

Before volumes can be calculated for the unstable parts of the slope, a robust geological model must be developed. This model is based on an extensive and complementary array of (sections

4.1 to 4.4) focused on understanding the lithological and structural conditions over the slope, the rates of deformation, the bathymetry under the unstable slope, and the geophysical conditions at depth. The different methods used generally lead to a coherent picture on the landslide behaviour and, therefore, our geological model, described below, has a high degree of confidence. We do note, however, that we have limited data at depth, and must rely on extrapolation to make inferences on the internal landslide body in three dimensions.

We draw our geological model (Figure 40) along profile line A (see Figure 4). This profile is parallel to slope azimuth and parallel to the deformation vectors obtained from dGNSS analyses, but not parallel to the dip of the most penetrative structure, which is the foliation. The dip of the foliation is therefore steeper than indicated in Figure 40 and oriented more towards the west. In the lower part of the slope the foliation is more folded and steeper and, in the front, vertical. The long persistence of foliation in the upper part of the slope represents an ideal failure surface, however, a large amount of rock deformation would be required for a failure plane to break through the lower part of the sliding rock mass. This interpretation is supported by the dGNSS vectors in the upper part of the slope, which indicate movement orientation that are approximately parallel to the foliation and dip out of the slope. Moreover, in the central part the dGNSS vector is parallel to the steeper foliation. This is possible if the lower part is expanding in opening cracks that could be mapped (Figure 10). In addition, this model fits with the observation that rock fall activity along the SE flank reaches behind the frontal more stable part of the rock mass. Most joints (J1, J2, J3, J4, J5) are vertical or almost vertical and joint set J1 and J2 form the back scarp. These are ideal boundary structures of the unstable rock mass to the NE and NW. Such a failure would than represent a wedge failure between the foliation sf and joint J2 with the movement taking place on the foliation. The kinematic analysis supports that model (Figure 30, Table 7 and 8) indicating that wedge sliding has, in most domains, a higher probability than planar sliding. Toppling failure is most likely in the upper slope and the rock fall activity from this area can be related to this failure mode.

It is more difficult to estimate the lower boundary of the rock slope deformation. GB radar indicates a strong decrease in deformation rates at the boundary between the foot of the arkose/quartzite and the scree below (Figure 34). Satellite based InSAR data are blind at that transition due to the steepness of the slope. However, they indicate that while the arkose/quartzite unstable rock mass is deforming with a higher rate of 15.5-34 mm/yr is there still slope deformation in the scree below, as well as in the phyllite rock outcrops with velocities between 3.5 and 11.5 mm/yr. It is inconclusive, therefore, whether the rock mass deformation in the arkose/quartzite crosses the lithological boundary to the phyllites or if there is independent deformation in these lithological zones. These units have contrasting mechanical properties and different structural conditions. Besides these differences, crossing the lithological boundary is further questionable owing to tectonic boundary between the Valdres spagmatite and the Vangs nappe (see chapter 2.2). In Figure 40 two models are proposed. In model A the lithological boundary forms the base of the main rock slope deformation, with a second independent, but less developed, deformation within the phyllites. The

detectable deformation in the scree can be related to compaction in this very active rock fall slope. In model B the deformation extends into the phyllite. The ERT data, the bathymetric data, and observations along the road, which has a continuous crash barrier, suggest that there is no deformation zone below the road. However, if such a zone was only poorly developed it would not be detectable with the methods used in this study. Therefore, in both models the deformation within the phyllites is limited to the lowermost phyllites that protrude from the scree. As the difference in the volume of the two models is low, as the major part of the instability lies within the arkose/quartzite, we limit the lower boundary to the lithological contact. This is further justified as we consider entrainment (see below), in the run-out path over the lower slope.

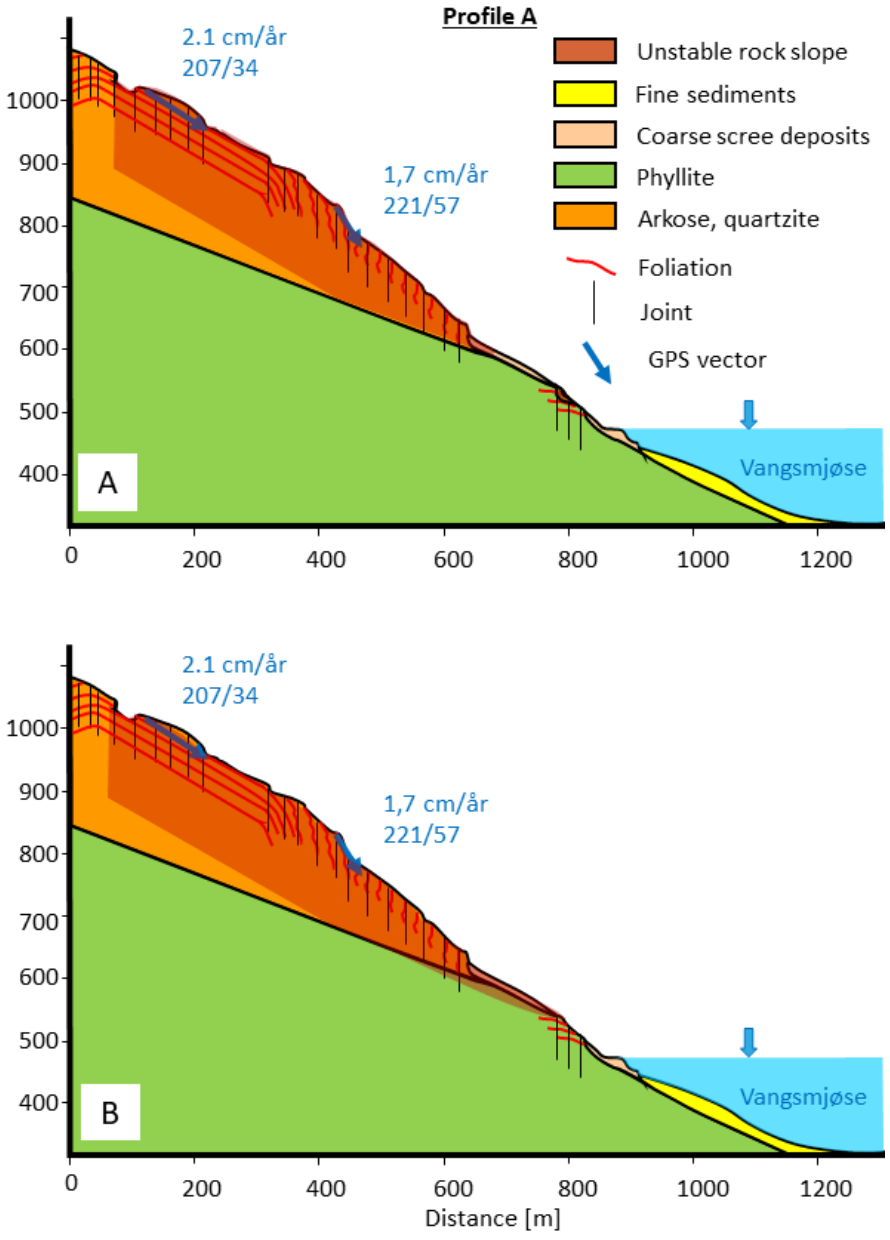

Figure 40) Geological models of the unstable rock slope at Skutshorn with A) showing the lower limit at the lithological boundary and a separate smaller instability developing in the phyllite and B) with the rock slope deformations in the arkose / quartzite and phyllite being connected.

4.6 Volume of the unstable slope of Skutshorn

The volume of the unstable mass was calculated by defining major bounding planes on a 10 m digital elevation model (DEM), supported by structural observations made in the field. The volume that could be mobilized by entrainment in the scree deposits below the unstable rock slope was also estimated. Two failure scenarios were defined based on lineaments in the rock slope. (Chapter 2.4). These are scenario A, which represents the larger unstable rock mass enclosed by the back scarp, and scenario B, which is separated from scenario A by an earlier small post-glacial failure (Chapter 4.1, Figure 23a). We assume a bulking factor of 20% for scenario A during failure, and a bulking factor of 10% for scenario B. The higher bulking factor used for scenario A reflects its greater travel length in a failure, where more rock mass expansion can be expected. The chosen bulking factors compare to those previously suggested for rock avalanches in Norway (Schleier et al., 2015; Oppikofer et al., 2017) and elsewhere (Hungr and Evans, 2004).

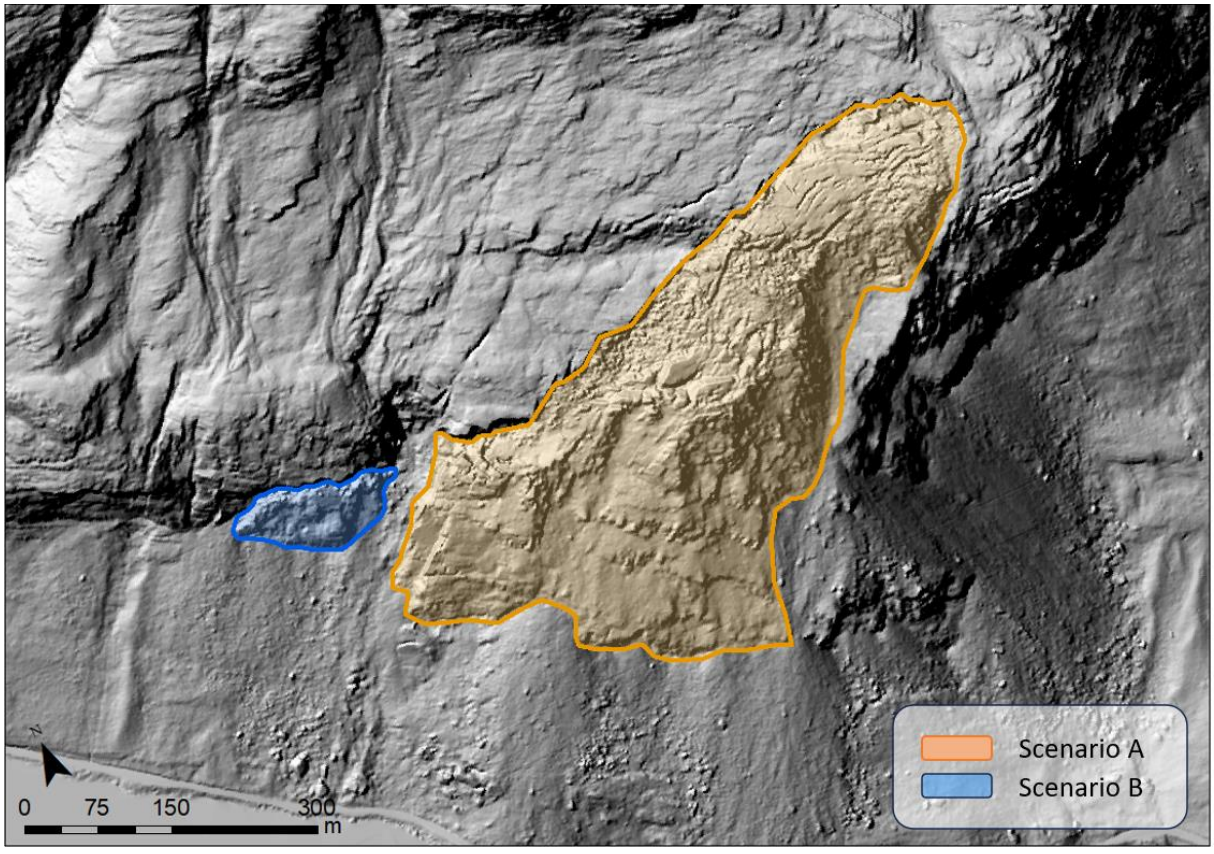

Figure 41) The unstable rock mass is split in two scenarios a and B because they could develop independently from each other. Both were defined on delimiting structures.

Scenario A has a surface area of 152,600 m^2. The rock volume was calculated using four planar surfaces, as shown in Figure 42. The (blue) plane (162/82) marks the NW portion of the back scarp, corresponding to the mean direction between J1 and J2 (see chapter 4.2.1). The (pink) plane (234/62) marks the short upper portion of the backscarp. This value was measured on the DEM and does not directly correspond to an observed structure. The (red) plane (242/38) represent the

basal surface of the niche of failure (see also Figure 12) and approximates the foliation measurements obtained in the upper east part of the instability (see chapter 4.2.1). The (green) plane (215/20) represents the basal failure surface in the lower part of the slope and approximates the fault separating the upper Valdres sparagmite nappe from the lower Vangs nappe (see chapter 2.2). The corresponding volume is 9.5 $\times 10^6$ m^3 without bulking and 11.4 $\times 10^6$ m^3 with bulking and the maximum thickness of the rock mass is 117 m. The volume is coloured in Figure 42 and corresponding structures shown with and without the overlying rock mass.

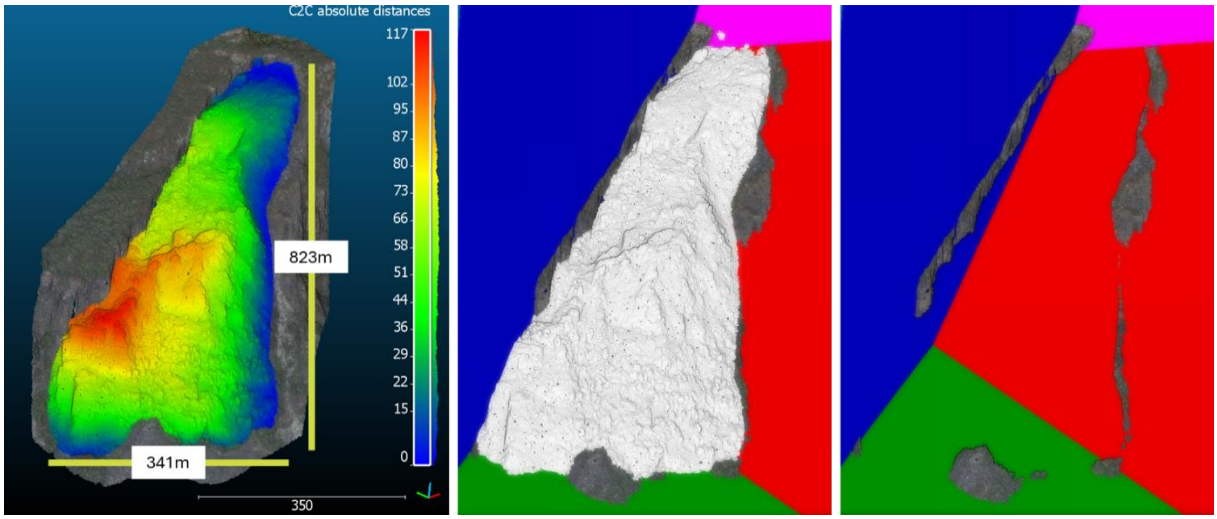

Figure 42) (Left) The rock mass coloured blue to red by the distance between the surface (DEM) and the intersection of planes using the PLANOS software tool. (Middle) Topography cut (grey) by planes. Blue (162/88), green (215/20), red (242/38) and pink (234/62). (Right) The mass is removed, showing the sliding surface and the new topography.

Scenario B is ~130 m long and 150 m wide and has a surface area of 8,660 m^2. It is located on the west side of Skutshorn and separated from the main slide mass by a previous failure. The rock body is detached from the rock wall at the back scarp. For the volume calculation, four planes were used that reach around 40 m deep. The limiting surfaces have orientations of 193/86 (green), 208/34 (blue), 212/12 (red), and 223/34 (pink). The planes were either mapped on the DEM and extrapolated into the slope (green, blue and pink) or reflect the suggested inclination of the nappe boundary at that location (red) (Figure 43). The resulting volume is ~165,000 m^3. The estimated volume with a 10% bulking is 182,000 m^3.

As mentioned above, a rock slope failure from the upper slope would likely entrain the unconsolidated scree deposit on the lower slope by ploughing on impact or through basal erosion. Hence, surfaces for entrainment below the unstable rock slope were defined (Figure 44). As the scree deposit is coarse, angular, permeable owing to large void spaces, a maximum of 5 m depth of erosion during entrainment was incorporated in the run-out model. However, the run out model software (Dan3D) requires a limitation to depth but models thereafter depth of erosion by itself. It suggested an average thickness of erosion of 2.5, and 1.3 m for scenarios A and B, respectively

(Table 10). This mass was not modelled as additional failed mass (see chapter 4.8.) as the material is positioned close to the lake shore and will thus rather decelerate a rock mass than add to its speed. But this volume was added to the mass entering the lake for our displacement wave analysis (see chapter 4.10).

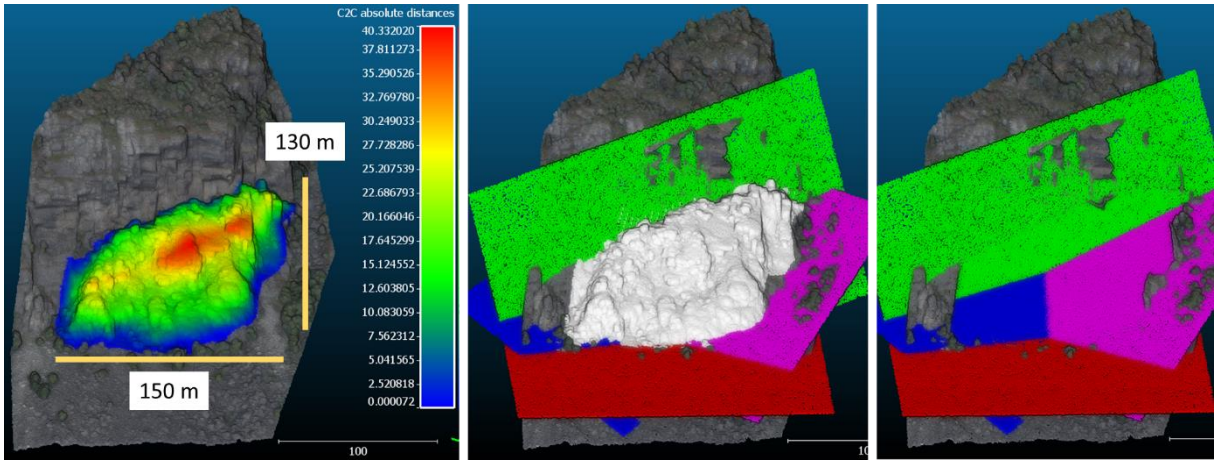

Figure 43) (Left) The rock mass (coloured blue to red) by the distance between the surface (DEM) and the intersection of planes using the PLANOS software tool. (Middle) Topography cut (grey) by planes. Green (193/86), blue (208/34), red (212/21) and pink (223/34). (Right) The mass is removed, showing the potential surface and the new topography.

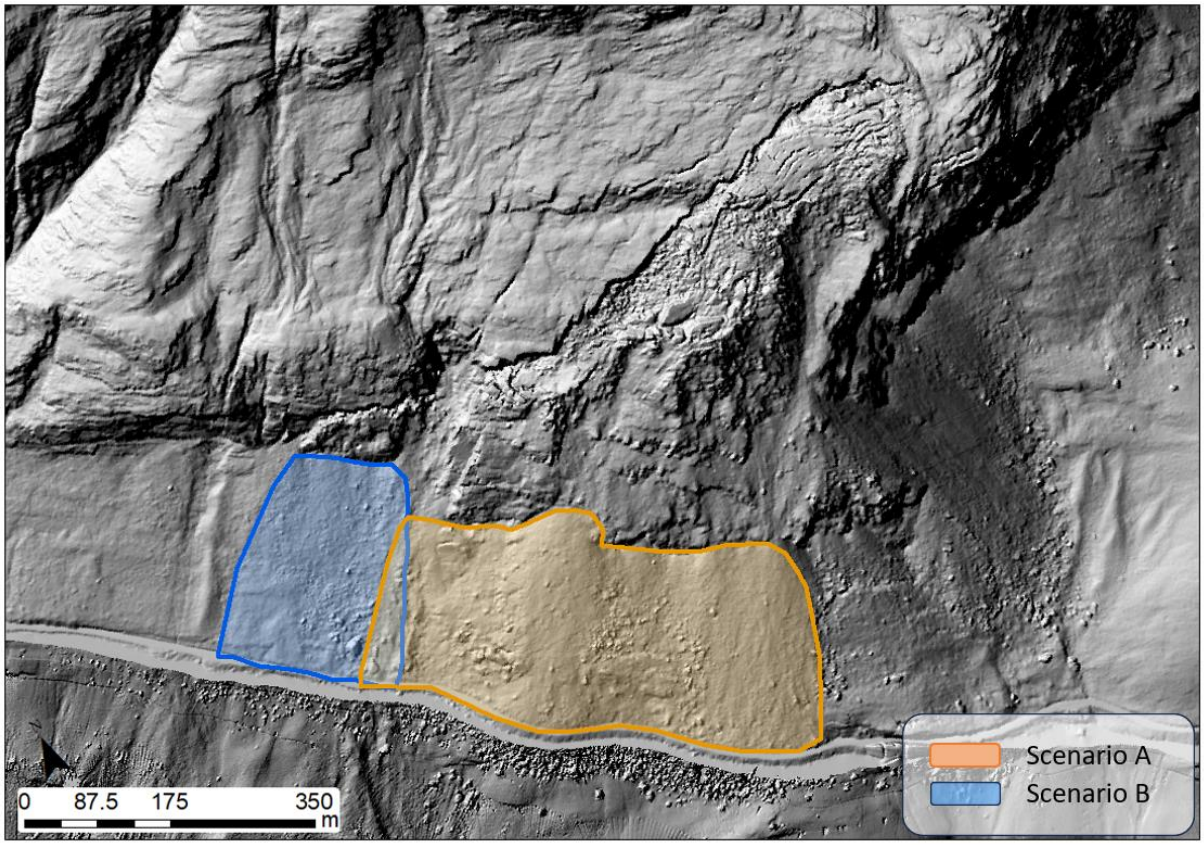

Figure 44) Area in the scree deposit that can be eroded by a rock slope failure for each scenario.

Table 10) Volume eroded by a rock slope failure for each scenario as modelled in Dan3D.

Scenario	Eroded volume	Maximum thickness	Modelled average thickness	Tolerance	Stop criterium
	[10^6 m^3]	[m]	[m]		
A	0.25	5	2.5	0	0.0001
B	0.07	5	1.4	0	0.0001

4.7 ^{10}Be surface exposure ages

The ^{10}Be ages of 17 boulders sampled from the scree slopes below Skutshorn are reported in Figure 45. These ages were calculated with CRONUS-Earth online calculators (Online cosmogenic-nuclide calculators (washington.edu)), global ^{10}Be production rate and and LSDn scaling (Balco et al., 2008). The focus here is to compare boulder ages on this particular slope only, thus only the internal uncertainties based on the uncertainties of laboratory measurements are relevant. External uncertainties include the ^{10}Be production rate uncertainty which is identical for all sample results. Including external uncertainty, the total uncertainty margins would be ~10 % larger.

The ages of boulders in the scree slopes are widely spread, with exposure ages between 240 ± 140 and 1870 ± 170 and show no clustering or spatial zoning (e.g. younger ages higher on the slope). This suggests that the deposit was not the result of a single failure event, but rather has built up through continuous rock fall activity, similar to historical observations. ^{10}Be exposure ages from the “Kviture” scree deposit (see also Figure 6), which lies in the SW extension of the niche where the 2018 rock fall was sourced, are on average younger than other ages. This suggests that this area is the most active scree. Pre-exposure of the boulders prior to rock fall cannot be ruled out, as the slope is very active and a sampled surface might have been at the surface or close to the surface prior to the rock fall event that transported the boulder into the sample position.

4.8 Hazard analysis of the unstable slope Skutshon

The hazard analysis for Skutshorn was carried out for scenario A and B. As the bounding structures for both scenarios are very well developed, and the basal failure plane not visible, both scenarios score similarly high for the structural and morphologic criteria. However, scenario A gets a somehow lower score for kinematic feasibility than scenario B. This is because scenario A has a higher variability of structures resulting in kinematic feasibility for failure in most part of the scenario but no kinematic feasibility in others (along the foot). Scenario B has a simpler structural set up resulting in feasibility for failure over the entire scenario. Besides this are the velocity of rock slope deformation and earlier events the criteria distinguishing both scenarios most. Scenario A has the highest velocity measured, which is a factor of ~8 higher in the GB InSAR velocities than for scenario B. There is a previous failure from Skutshorn of a similar volume to scenario B. This is of unknown age. Scenario A being by a factor of 46 also significantly larger than scenario B is therefore clearly most critical scenario. This will result in the most restrictive hazard zones. It falls within the high hazard class using Hermanns et al. (2012) and has a yearly probability higher than

1/1000 years after Blikra et al., (2016). Scenario B falls in the medium hazard class and has a yearly probability lower than 1/5000 years respectively (see Figure 54).

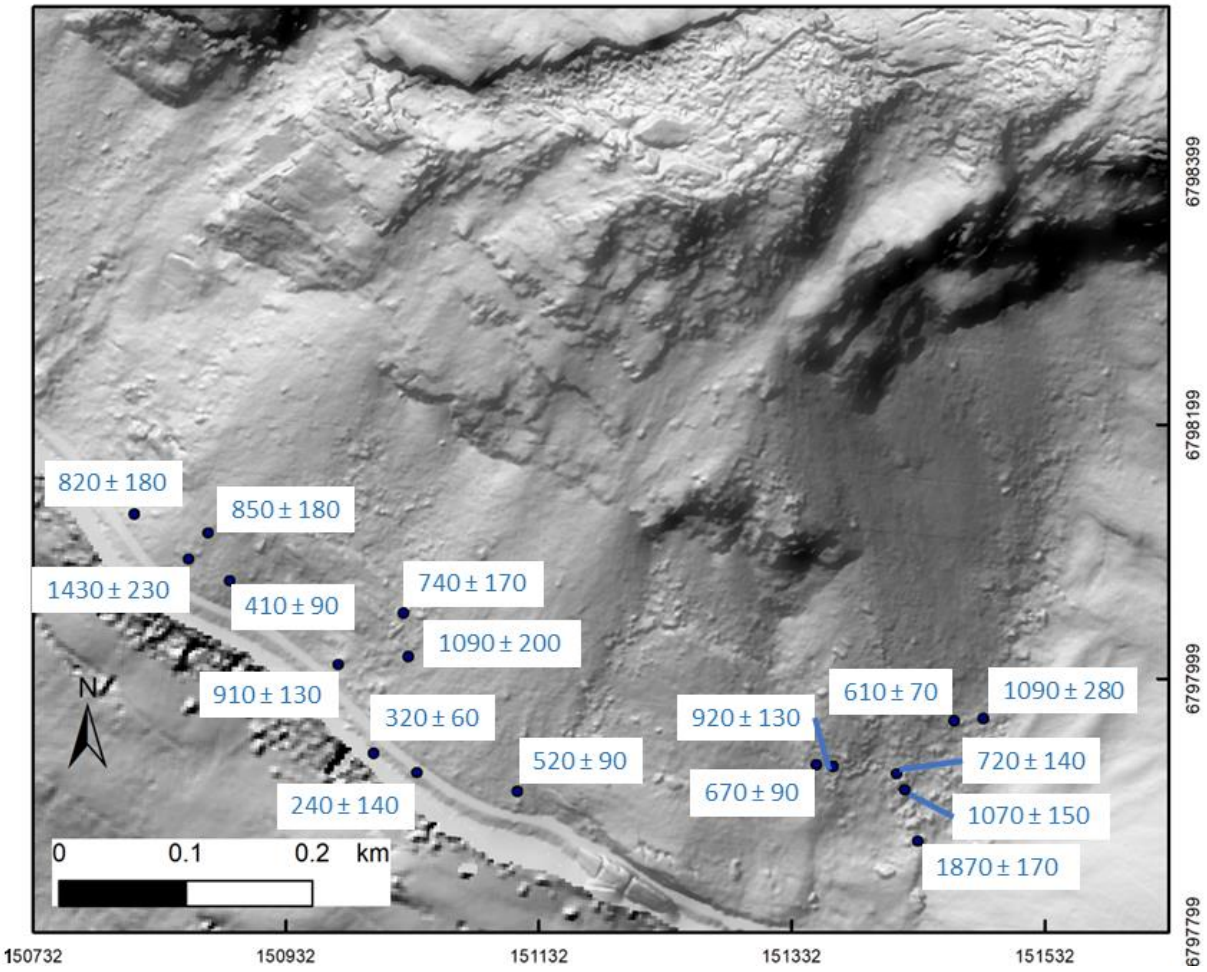

Figure 45) Boulder position with respective ^{10}Be ages (years) of the boulder surface with internal uncertainties (see text).

Below we present a short evaluation for each criterion used for the hazard ranking for both scenarios. The exact weighting of criteria are given in Appendix A:

Scenario A:

1) **Backscarp:** The back scarp is fully developed over the entire length, has a vertical offset, and has an opening everywhere except at the top section where it is filled with coarse scree deposited on a high angle.
2) **Potential sliding surface:** In the upper part the foliation is in most domains an ideal sliding surface. In the lower part the foliation is often too steep to allow for sliding. In the foot area the foliation vertical and does not allow for sliding.
3) **Flanks:** The NW flank coincides with the back scarp and is fully developed. The SE flank is open over its entire length.

4) **Kinematic feasibility:** Wedge and planar sliding are feasible in most structural domains in the upper and central parts of the deformed mass, but not in the foot.
5) **Morphologic evidence on the lower limit:** A daylighting structure cannot be found in the foot area but some bulging and opening along vertical cracks is visible.
6) **Displacement rates:** The measured displacement rates are consistent across several methods. Movement rates vary over the rock slide mass but generally fall between 1 and 4 cm/yr, with an exception along some sectors of the foot where displacement was not detected.
7) **Acceleration:** Based on the short time series of deformation data acceleration is not detectable and no dateable sliding surface exists. Therefore, standard values were used.
8) **Increase in rock fall activity:** A very intense rock fall activity can be mapped in comparison with adjacent slope sections that are not deforming. This rock fall activity has been observed through historic times. An increase or decrease over the past century cannot be documented.
9) **Earlier events:** Only one rock avalanche could be mapped within lake Vangsmjøse and neighbouring valleys to Skutshorn. The rock avalanche deposit mapped in Vangsmjøse sourced from a different nappe than the instability at Skutshorn and the volume is about a magnitude smaller. Thus, we conclude that no comparable mappable post-glacial deposit could be detected.

Scenario B:

1) **Backscarp:** The back scarp is fully developed and open over the entire length. The scarp seems to have a vertical offset, however, this could also reflect differential erosion inside the slide mass when compared to the stable mass behind.
2) **Potential sliding surface:** The foliation is too steep in the front, however, in this sector there are exfoliation joints with persistence that represent likely sliding surfaces.
3) **Flanks:** Both flanks are fully open.
4) **Kinematic feasibility:** Planar and wedge sliding are feasible.
5) **Morphologic evidence on the lower limit:** A daylighting structure cannot be found in the foot area.
6) **Displacement rates:** The displacement rates are more uncertain for scenario B than for scenario A, as no dGNSS bolts are installed on the rock mass. GB InSAR shows only a few points over scenario B, and these move away from the scanner (thus upslope). Satellite based InSAR suggests a mean velocity of 2.5 mm/year for the entire block and a velocity of 4.5 mm/yr for the upper parts. The direction of the LOS is approximately parallel to the slope meaning the measured velocity is therefore likely close to the true movement velocity. The velocity is measured over a period of five

years with interpolations over the years. However, velocities in the summer month when actual data are required are lower than the average over five years.

7) **Acceleration:** Based on the short time series of deformation data an acceleration is not detectable and no dateable sliding surface exists. Therefore, standard values were used.
8) **Increase in rock fall activity:** A very intense rock fall activity can be mapped in comparison with adjacent slope sections that are not deforming. This rock fall activity has been observed through historic times. An increase or decrease over the past century cannot be documented.
9) **Earlier events:** Just beside this scenario there is a niche of failure, and corresponding deposits can be mapped on the lake bottom. The age of this event is unknown.

4.9 Run-out analysis for the unstable slope of Skutshorn

The dynamic modelling was performed with Dan3D (Hungr, O., & McDougall, S. (2009)) for both scenarios mentioned in section 4.6, using a 1 m DEM down sampled to 10 m resolution and containing the bathymetry. The mass travels a short distance on land, around 300 m before reaching the Vangmjose lake. The runout path is over talus with angular and large range of block sizes, which we interpret to be rough and thus having a relatively high friction angle. It is unlikely that porewater would be added to the moving mass, and the short distance to the lake is unlikely to allow a flow-like behaviour. Therefore, we used a frictional rheology for all the simulations rather than Voellmy rheology. The talus may add volume to the moving mass but also absorb some of the energy. All the simulations reached the lake, however, the volume entering water changes significantly with modifications in the friction angle. For each scenario, we performed 6 models using the following parameters (Table 11).

Table 11) Parametrisation of the Dan3D simulations.

Rheology	Unit Weight [KN/m^3]	Friction Angle [deg]	Pore-Pressure [-]	Internal Friction angle [deg]
Frictional	27.5	25	0	35
Frictional	27.5	26	0	35
Frictional	27.5	27	0	35
Frictional	27.5	28	0	35
Frictional	27.5	29	0	35
Frictional	27.5	30	0	35

4.9.1 Run-out analysis Scenario A

As mentioned in section 4.6, scenario A has a volume of 9.5 $\times 10^6$ m^3 without bulking and 11.4 $\times 10^6$ m^3 with bulking. In all Dan3D simulations a large percentage of the start material that enters the lake. This varies with the friction angle, with 62% of the total mass entering the lake with a friction angle of 25 degrees and 35% entering the lake for a friction angle of 30 degrees (Figure 46, 47). We judge that a friction angle of 27 degrees is the most representative for the site. This lies within

the range of friction angles (20 – 30 degrees) empirically determined by Aaron et al. (2022) for the mobilized volume of ca. 10 million cubic meters and is slightly higher than that of a rock avalanche at a comparable site in Western Canada that entered Chehalis lake (a friction angle of 25 degrees was determined (Aaron et al., 2022)). However, the slope at Chehalis lake is steeper and no coarse scree deposits occur there. It follows also empirical data by McKinnon (2010).

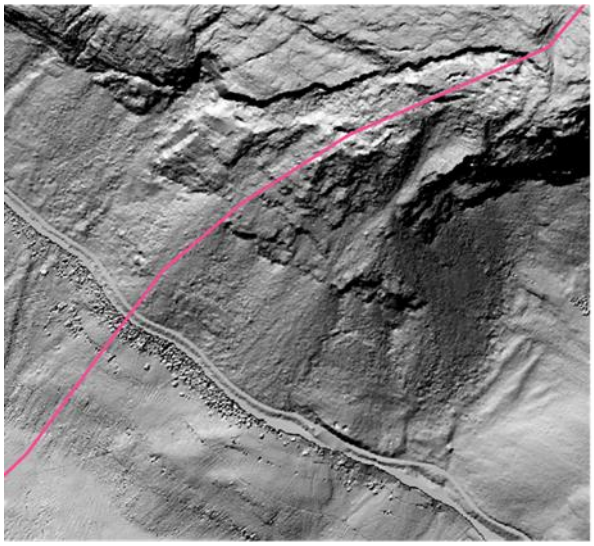

Friction angle	Vol : 9.5 millions m^3
25	3554177
	5936283
26	3938541
	5551919
27	4451026
	5039434
28	5181791
	4308669
29	5665805
	3824655
30	6054913
	3435547

Figure 46) (Left) Profile NE-SW going through scenario A to the lake. (Right) table showing the rock mass entering the lake (blue) and the mass remaining on land (brown).

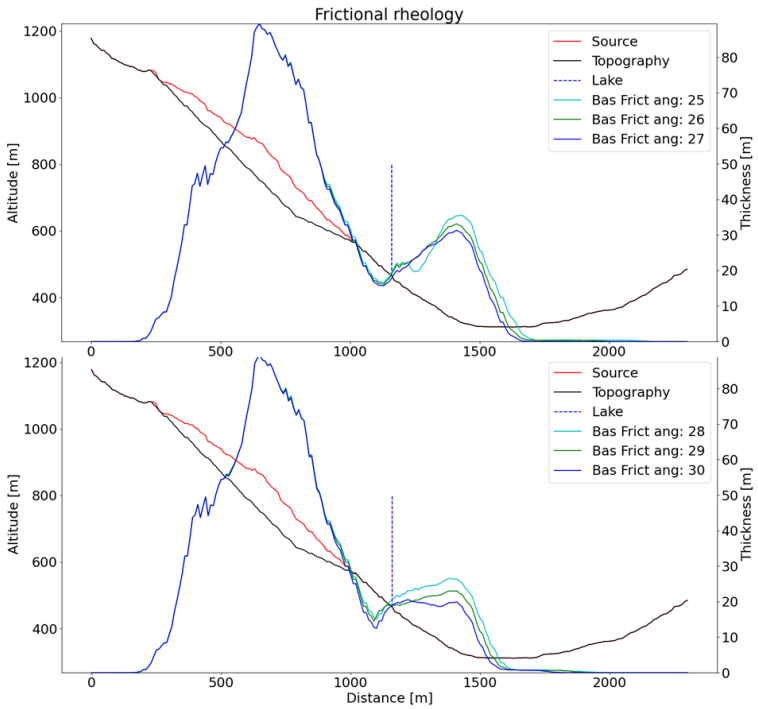

Figure 47) Run-out profiles output from Dan3D for Scenario A showing the deposition on land and in the lake on the topography for varying friction angles.

All models have a maximum velocity ranging between 17 and 24 m/s in the main mass on entry into the lake. The maximum velocity for a friction angle of 27 degree is ~35 m/s, however, this is for a small volume. The main volume enters the lake at approximately 21 m/s (Figure 48).

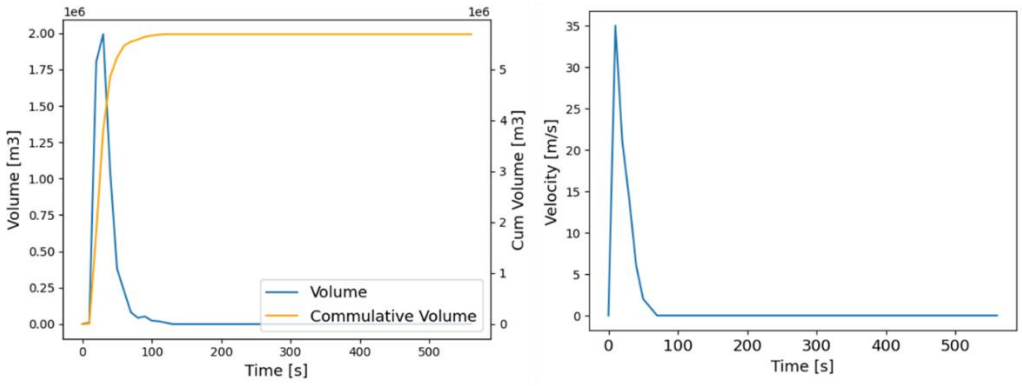

Figure 48) Rock mass entering in the lake for simulation with a friction angle of 27 degrees for scenario A. Left shows the volume entering the lake versus time and right shows the velocity of the rock mass on impact into the lake versus time. After 30 seconds, 3'805'674 m^3 enters the lake with the average velocity of 14 m/s but a large volume already enters with a velocity of 21 m/s. The final volume (5'694'276 m^3) enters the lake after 120 seconds with a velocity of 3 m/s.

4.9.2 Run-out analysis Scenario B

The characteristics of the runout path are comparable for scenario A and B and, thus, we use the same parameters as for scenario A (Figures 49. 50). Note, however, that a slightly higher friction angle of 30 degrees is suggested by the empirical data by Aaron et al. (2022). However, these empirical data is a single data point within the corresponding magnitude class. The simulations suggest that 80% of the total mass would enter the lake for a friction angle of 25 degrees, while only 50% would reach the lake using a friction angle of 30 degrees. With a friction angle of 27 degrees, 75% of the rock mass would enter the lake.

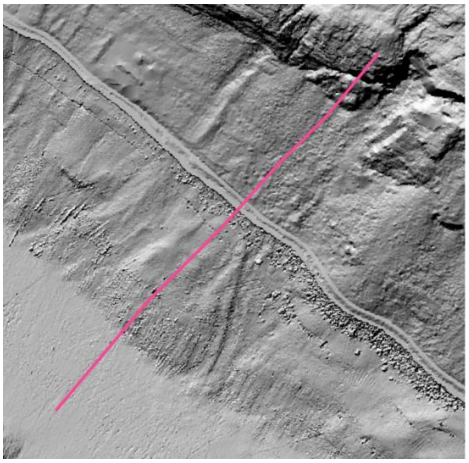

25	33275
	131455
26	36652
	128078
27	38712
	126018
28	44148
	120582
29	64245
	100485
30	81871
	82859

Figure 49) (Left) Profile NE-SW going through scenario C to the lake. (Right) table showing the rock mass entering the lake (blue) and the mass remaining on land (brown).

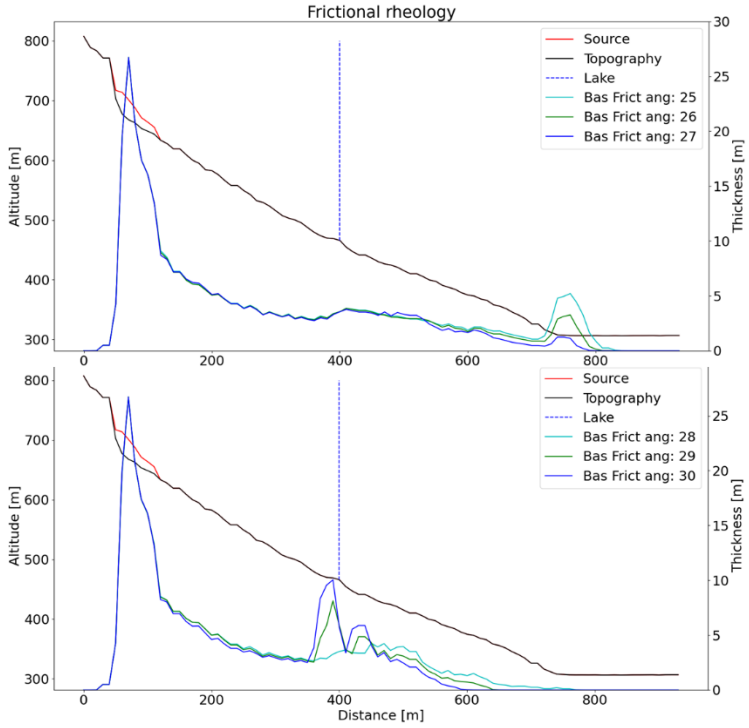

Figure 50) Run-out profiles output from Dan3D for Scenario A showing the deposition on land and in the lake on the topography for varying friction angles.

All models have a maximum velocity range at impact between 22 and 27 m/s. For a friction angle of 27 degrees the maximum velocity is 25 m/s (Figure 51).

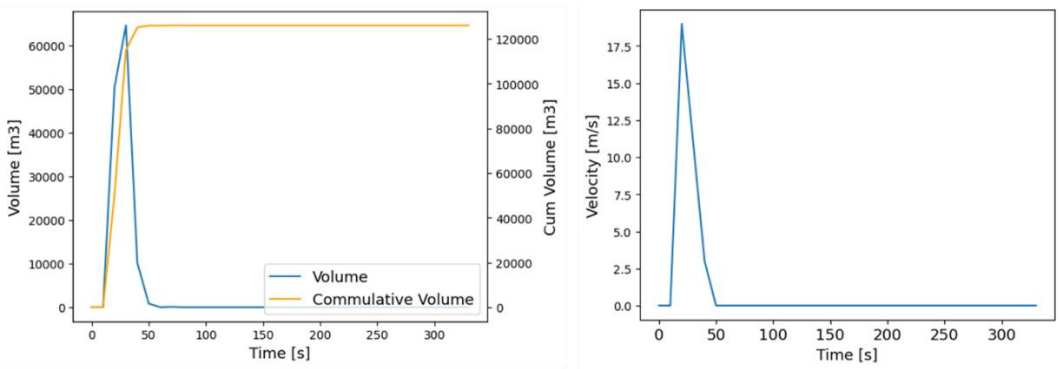

Figure 51) Rock mass entering in the lake for simulation with a friction angle of 27 degrees for scenario B. Left shows the volume entering the lake versus time and right shows the velocity of the rock mass on impact into the lake versus time. After 20 seconds, 50'407 m^3 enters the lake with at 25 m/s (average 19 m/s). The final volume (126'018 m^3) enters the lake after 50 seconds with a velocity of 3 m/s.

4.10 Displacement wave analysis

Table 12 summarizes the volumes considered in the wave displacement using the SPLASH formula. These volumes are the volumes of failed rock mass, corrected with a bulking factor, that

enter the lake based on runout modelling analysis (27 degree friction angle). In addition, the final volume entering the lake includes material eroded from the scree deposits below the unstable rock mass (see Table 10), which is summarized for both scenarios in Table 12. The wave run-up heights were calculated at impact locations around the lake selected close to settlements, and indicate higher run-up heights for scenario A than scenario B (Figure 52).

Table 12) Summary of volume for each scenario. Parametrisation of the Dan3D simulations.

Scenario	Initial Volume [m^3]	Bulking [%]	Volume incl. bulking [m^3]	Erosion [m^3]	Percentage entering lake [%]	Volume reaching lake [m^3]
A	9,490,460	20	11,388,552	250,000	51.9	6,040,408
B	164,730	10	181,203	75,000	73.2	187,541

The SPLASH formula is not developed to consider probabilities of run-up. However, those probabilities are required for the Norwegian building codes (TEK 17). In addition, a full 3D model has large advantage over an empirical assessment depending on selected profiles in an area with settlement and large infrastructure as it gives a wave run-up for the entire lake shore. Therefore, NVE commissioned a full 3D model of the run-up including maximum run-up and different yearly probabilities of run-up that was provided in NGI report 20200665-01-R (Glimsdal, 2022). In the following the calculated run-ups heights from this report are used in the consequence analysis.

4.11 Risk analysis Skutshorn

4.11.1 Proposed hazard zones

The hazard zones have been drawn for Skutshorn based on the runout analyses described in section 4.9, the full 3D displacement wave (tsunami) analyses carried out by Glimsdal (2022) for scenario A, and the SPLASH displacement wave analysis from this report for scenario B. They are shown in Figure 53 and described in detail in the respective reports.

4.11.2 Consequence analysis

The risk analysis only considers the potential loss of life within the propagation area of the modelled tsunami, as there are no permanent residents or buildings directly within the landslide runout zone.

The number of people located within the hazard zone of scenario A is given in Table 13. In the 1/5000 tsunami hazard zone, there are a total of 462 exposed buildings, including 2 kindergarten buildings, 1 school building, 58 residential buildings, 20 holiday homes, 33 camping/rental cabins, 1 town hall, 3 church buildings, 3 cultural buildings, 25 commercial buildings, 93 agricultural buildings and 52 garages. Notably, there are 129 buildings for which the use is not registered in the available dataset. These buildings are not included in further analysis.

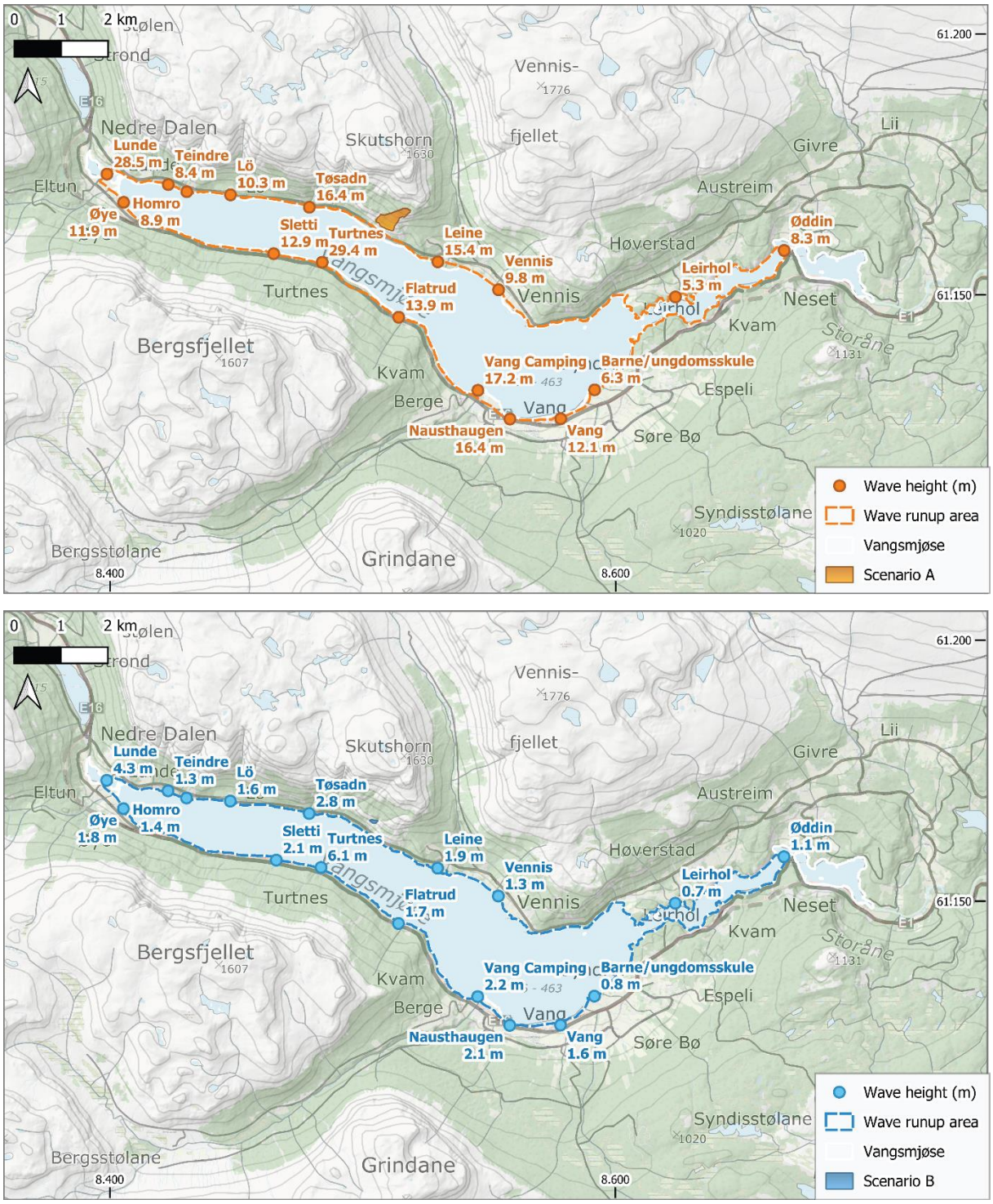

Figure 52) Wave displacement for scenario A above and scenario B below. The points of interest are marked, and the wave run-up height is given in parenthesis.

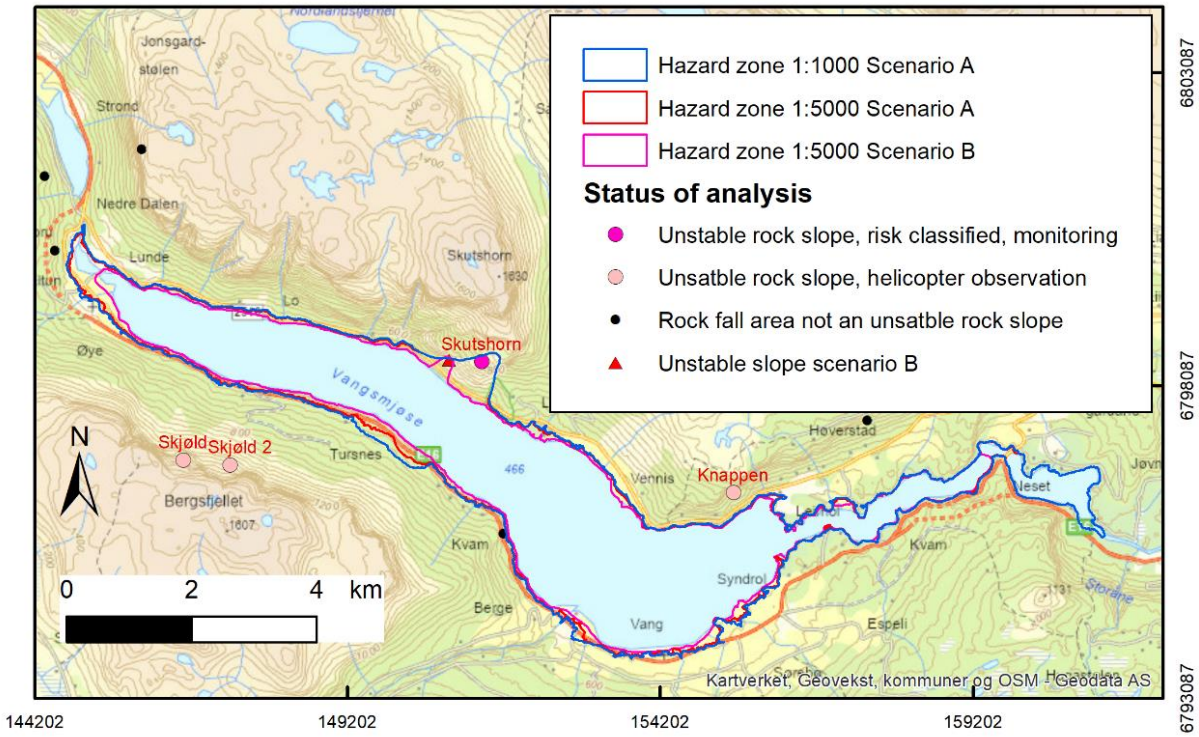

Figure 53) Hazard zones for the unstable rock slope of Skutshon and other rock slopes that have been investigated in the area.

The analysis considers exposure which is assumed to be 70% for people within tsunami hazard zones. The number of tourists staying overnight within the hazard zones are included using standard values related to building types. Day-visiting tourists/travellers are not included.

Table 13: Number of exposed persons in the hazard zones of scenario A

			Exposed people (including estimates from buildings)		
Hazard zone	Permanent residents	Attendees kindergartens/schools	**Min**	**Average**	**Max**
Direct hit	0	0	0	0	0
Tsunami 1/1000	85	0	104	160	296
Tsunami 1/5000	101	226	169	241	442

The number of people located within the hazard zone of scenario B is given in Table 14. In the 1/5000 tsunami hazard zone, there are a few cabins and commercial buildings and agricultural buildings. The maximum number of persons that are calculated to be in this building are shown and the number is corrected for exposure and potential live loss in table 14.

Table 14: Number of exposed persons in the hazard zones of scenario b

			Exposed people (including estimates from buildings)		
Hazard zone	Permanent residents (max)	Attendees kindergartens/schools (max)	**Min**	**Average**	**Max**
Direct hit	0	0	0	0	0
Tsunami ~1/2000	12	0	19	34	61

4.11.3 Risk analysis

The consequences are combined with the corresponding probabilities for scenario A to calculate risk of deaths per year (Table 15). For Skutshorn scenario A, it is expected an average risk (R) of 0.412 deaths per year within the hazard zones. This corresponds to one death every 2.4 years on average. In practice, the average has little meaning, as we are considering an event that has a small annual probability compared to other types of events (e.g. rock fall from Skutshorn). Therefore, combined consequences (C′) are calculated, which consider all hazard zones, and which give an expected risk when multiplied by the landslide probability. The combined consequences are calculated to 116.2 deaths (avg) and are plotted in the risk matrix with corresponding uncertainty (Figure 54). The risk analysis shows that Skutshorn qualifies as a high-risk object.

Table 15: Results from the risk analysis for Skutshorn Scenario A

	Consequences [deaths]			**Probability [/yr]**		**Risk [deaths/yr]**		
	min	**avg (C)**	**max**	**original (p)**	**combined (p')**	**min**	**avg (R)**	**max**
Direct impact	0	0	0	0,00355	0,00127	0,00000	0,00000	0,00000
Displacement wave with 1/1000	104	160	296	0,00227	0,00167	0,17410	0,26785	0,49552
Displacement wave with 1/5000	169	241	442	0,00060	0,00060	0,10140	0,14460	0,26520
					0,00355	0,27550	0,41245	0,76072
					(C')			
Combined consequences	77,6	116,2	214,4					

(Corresponding to number of deaths with the original probability)

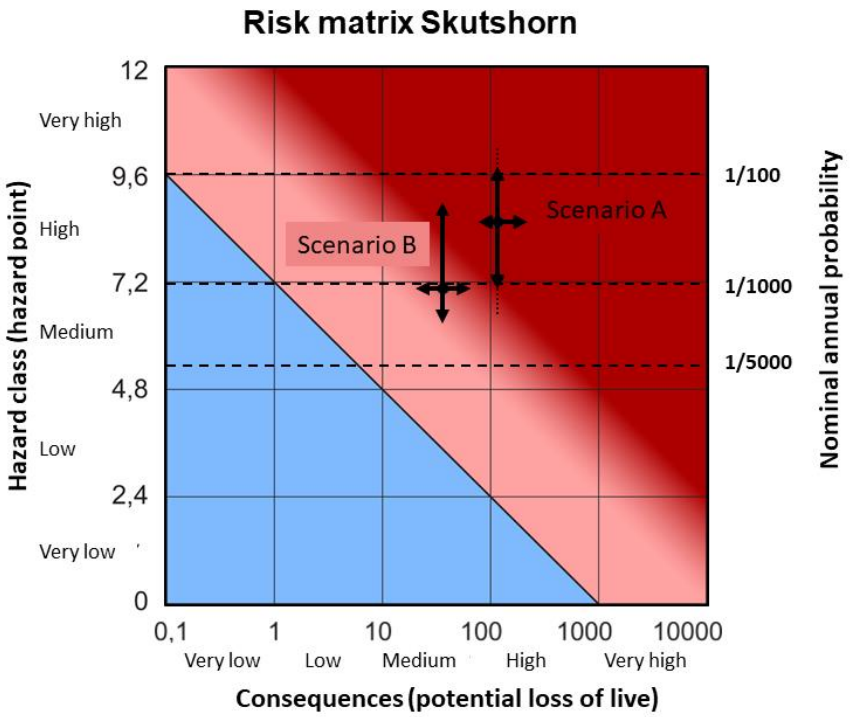

Figure 54) Risk matrix for Skutshorn Scenario A and B. Scenario A has high hazard and high consequences and fall into the high risk. Scenario B has medium hazard and medium consequences and is thus medium risk.

5. DISCUSSION AND CONCLUSIONS

This report describes the geological conditions of the slope instability at Skutshorn today based on data collected in between 2018 and 2022. Our work includes a wide variety of data types and observations, including structural and morphological measurements from the field and elevation models, helicopter observations in inaccessible (e.g., steep) terrain, displacement data from dGNSS, GB InSAR and satellite based InSAR, bathymetric data from Vangsmjøse, geophysical (ERT) data along the base of the instability, and cosmogenic nuclide dates of boulder deposits. Together, these data were combined to generate a geological model of the rockslide that, in turn, was used to calculate the volumes, simulate the run-outs, and compute displacement waves runup heights for two failure scenarios

The rock slope instability lies along a tectonic nappe boundary that caused complex deformation of the rocks. This tectonic deformation pushed rigid massive lithologies over fragile tightly foliated rocks. Rock deformations occur in both nappes with the rock deformation clearer developed in the upper nappe. The lower unit is strongly covered by coarse scree derived from the upper slide mass. We have divided the unstable rock mass in two scenarios within the upper nappe. Those are independent of each other and separated in space by a prehistoric rock slope failure. It is evident that there is an extremely high rock fall activity on that mountain that likely gave the mountain its name: Skutshorn (translated to “Shooting horn” in English). This rock fall activity has retrogressively eroded into the unstable rock mass along the most of SE flank and in the lower parts of the NW

flank. This rock fall activity is ongoing and has exposed part of the sliding surface. It is eroding into the central part of the rock mass where displacement velocity is highest.

Displacement rates are spatially variable across the instability, as suggested by dGNSS. These are constant in azimuth but change in dip, with shallower vectors in the upper part and steeper vectors towards the centre. The highest rates occur in the upper and central part. Displacement rates are lowest along the foot of the slide mass.

Our data are sufficient to robustly characterise the deformation observed at the surface, but not strong enough to fully describe the deformation at depth. Our geological model thus relies on extrapolation of our surface observations into depth. Nonetheless, geophysical data collected along the lake shoreline and bathymetric data for Vangsmjøse do suggest that deformation is absent or minimal in the lower slope and beneath the lake. The highest uncertainty in our model, besides the uncertain depth of deformation, is whether deformation in the upper nappe is connected to deformation in the lower nappe, whether they are deforming independently of each other, or whether the deformation in the lower nappe is caused by loading of the slope with scree by the constant rock fall activity. We extrapolated the deformation in the upper nappe following visible surface structure into depth. This suggests a basal sliding surface up to 117-m deep. The deformation does not have to be that deep especially in the lower part of the slope where ideal structures for sliding were not observed and we thus took the nappe boundary as basal detachment surface. This results in an overestimation of the rock volume in the upper part, which is conservative. Thus, we decided not to include the deformation in the lower nappe into the rock mass of our scenarios, as we have no indication whether they are indeed connected and how deep a sliding surface would be. This interpretation is not conservative, but we think that being more conservative in the upper slope justifies a less conservative approach in the lower slope to prevent exaggerated related hazard zones.

The fact that the central part of the slope has a depression where deformation rates are highest suggest that the slope has not deformed evenly in the past. Changing deformation patterns in time (and potentially the future) are thus a reasonable possibility. In the event of such changes, new models of failure scenarios should be developed, and our present geological model adjusted. Skutshorn shows a very high rate of constant rock fall activity which is ongoing for more than a millenia as suggested by our cosmogenic nuclide ages of rock fall boulders. This activity will reduce the volume of the unstable rock mass in future. Thus, a catastrophic failure in the dimension of today is not a “must” at least not in the scenarios as discussed here. Our assessment is the best we could do for today’s conditions and existing observations.

A collapse of the unstable rock mass would be highly likely to cause a rock avalanche due to the very persistent structures in the upper part that are unfavourably oriented. A rock avalanche would not reach any houses but a large mass would reach lake Vangsmjøse with extremely rapid velocity, using the velocity classes in Hungr et al. (2014). Such an impact into lake Vangsmjøse would cause

a displacement wave that would be a threat to the population around the lake. Life losses for a failure of scenario A would be high. The high hazard and the high consequences result in a high risk for society in the case of a sudden event on the unstable rock slope of Skutshorn for scenario A, and a medium risk for scenario B.

ACKNOWLEDGEMENT

This has been a collaborative project between the Geological Survey of Norway (NGU) and the Norwegian Water Resources and energy directorate (NVE) financed through the landslide program of NVE. Multiple colleagues within both organizations contributed with good idea during the multiple meetings we had in the course of the years. The collaboration with Vang municipality over the years was fluent and very helpful. Lars Evje (UiB) performed the sample preparation for ^{10}Be dating, and Jesper Olsen (AARAMS) performed the analysis.

REFERENCES

Aaron, J., S. McDougall, J. Kowalski, A. Mitchell and N. Nolde (2022). "Probabilistic prediction of rock avalanche runout using a numerical model." Landslides **19**(12): 2853-2869.

ABEM, 2012. ABEM Terrameter LS. Instruction Manual, release 1.11, Sundbyberg: ABEM Instrument AB, Sweden.

Ballantyne, C. K., J. O. Stone and L. K. Fifield (1998). "Cosmogenic Cl-36 dating of postglacial landsliding at the Storr, Isle of Skye, Scotland." The Holocene **8**(3): 347-351.

Blikra, L. H., E. Anda and O. Longva (1999). FJellskredprosjektet i Møre og Romsdal: Status og planer. NGU report **1999/120:** 21.

Blikra, L. H., O. Longva, A. Braathen, E. Anda, J. F. Dehls and K. Stalsberg (2006a). Rock Slope Failures in Norwegian Fjord Areas: Examples, Spatial Distribution and Temporal Pattern. Landslides from Massive Rock Slope Failure; NATO Science Series, IV. Earth and Environmental Sciences, Vol 49. S. G. Evans, G. Scarascia Mugnozza, A. Strom and R. L. Hermanns. Dodrecht, Netherlands, Springer**:** 475-496.

Blikra, L. H., E. Anda, J. Høst and O. Longva (2006b). Åknes/Tafjord-prosjektet: Sannsynlighet og risiko knyttet til fjellskred og flodbølger fra Åknes og Hegguraksla. NGU report **2006.039:** 20.

Blikra, L. H. and L. Kristensen (2013). Monitoring Concepts and Requirements for Large Rockslides in Norway. Landslide Science and Practice, Springer**:** 193-200.

Blikra, L., M. Böhme, J. Dehls, R. Hermanns, T. Oppikofer, T. Redfield, J. Rønning, F. Yugsi Molina, U. Domaas and A. Pfaffhuber (2013). "The unstable phyllitic rocks in Stampa–Flåm, western Norway: compilation, scenarios, risk and recommendations." NVE rapport **35-2013**: 22.

Blikra, L. H., G. Majala, E. Anda, B. Hallvard, O. Eikenæs, G. Helgås, T. Oppikofer, R. L. Hermanns and M. Böhme (2016). Fare- og risikoklassifisering av ustabile fjellparti. NVE-Rapport. **77-2016:** 47.

Böhme, M., H. Bunkholt, J. Dehls, T. Oppikofer, R. L. Hermanns, E. Dalsegg, L. Kristensen, T. R. Lauknes, H. Ø. Eriksen and T. R. Lauknes (2016). Geologisk modell og fare-og risikoklassifisering av det ustabile fjellpartiet Gamanjunni 3 i Manndalen, Troms. NGU report. **2016.031:** 63.

Byggeteknisk forskrift, TEK 17, 2017, Byggteknisk forskrift (TEK17) med veiledning - Direktoratet for byggkvalitet (dibk.no).

Dahle, H., E. Anda, A. Saintot and S. Sætre (2008). Faren for fjellskred fra fjellet Mannen i Romsdalen. NGU report. **2008.087:** 21.

Dahlin, T. (1993). On the automation of 2D resistivity surveying for engineering and environmental applications, Université de Lund, Suède, Thèse de 3ème cycle.

Dahlin, T. and B. Zhou (2006). "Multiple-gradient array measurements for multichannel 2D resistivity imaging." Near Surface Geophysics **4**(2): 113-123.

Dehls, J. F., Y. Larsen, P. Marinkovic, T. R. Lauknes, D. Stødle and D. A. Moldestad (2019). INSAR. No: A National Insar Deformation Mapping/Monitoring Service In Norway-From Concept To Operations. IGARSS 2019-2019 IEEE International Geoscience and Remote Sensing Symposium, IEEE.

Devoli, G., O. Eikenæs, A. Taurisano, R. L. Hermanns, L. Fischer, T. Oppikofer and H. S. S. Bunkholt (2011). Plan for skredfarekartlegging – Delrapport steinsprang, steinskred og fjellskred. NVE rapport. **15/2011:** 66.

Frodella, W., A. Ciampalini, F. Bardi, T. Salvatici, F. Di Traglia, G. Basile and N. Casagli (2018). "A method for assessing and managing landslide residual hazard in urban areas." Landslides **15**(2): 183-197.

Furseth, A. (2006). Skredulykker i Norge. Oslo, Norway, Tun Forlag.

Geertsema, M., B. Menounos, G. Bullard, J. L. Carrivick, J. Clague, C. Dai, D. Donati, G. Ekstrom, J. M. Jackson and P. Lynett (2022). "The 28 November 2020 landslide, tsunami, and outburst flood–A hazard cascade associated with rapid deglaciation at Elliot Creek, British Columbia, Canada." Geophysical research letters **49**(6): e2021GL096716.

Glimsdal, S. (2022). Flodbølger etter skred fra Skutshorn ved Vangsmjøse, Vang kommune. NGI rapport. **20200665-01-R:** 22.

Gosse, J. C. and F. M. Phillips (2001). "Terrestrial in situ cosmogenic nuclides: theory and application." Quaternary Science Reviews **20**(14): 1475-1560.

Heim, M., U. Schärer and M. A.G. (1977). "The nappe complex in the Tyin-Bygdin-Vang region, Central Southern Norway." Norsk Geologisk Tidskrift **57**: 171-178.

Heim, M. (1979). Struktur und Petrographie des Jotun-Valdres-Deckenkomplexes und der ihn unterlagernden kaledonischen Deformationszone im Gebiet des östlichen Vangsmjøsi (zentrales Südnorwegen), ETH Zurich.

Heim, M. (2003). Vangsmjøsi 1617 III. Berggrunnskart 1:50.000. Trondheim, Norges geologise undersøkelse.

Hendron A.J, J. and F. D. Patton (1987). The Vaiont Slide; a geotechnical analysis based on new geologic observations of the failure surface. Dam failures. Amsterdam, Netherlands, Elsevier. **24**(1-4)**:** 475-491.

Hermanns, R. L., S. Niedermann, A. V. Garcia, J. S. Gomez and M. R. Strecker (2001). "Neotectonics and catastrophic failure of mountain fronts in the southern intra-Andean Puna Plateau, Argentina." Geology **29**(7): 619-622.

Hermanns, R. L., L. Hansen, K. Sletten, M. Böhme, H. S. S. Bunkholt, J. F. Dehls, R. S. Eilertsen, L. Fischer, J. S. L'Heureux, F. Høgaas, B. Nordahl, T. Oppikofer, L. Rubensdotter, I. L. Solberg, K. Stalsberg and F. X. Yugsi Molina (2012a). Systematic geological mapping for landslide understanding in the Norwegian context. Landslides and Engineered Slopes. Protecting Society through Improved Understanding: Proceedings of the 11th International & 2nd North American Symposium on Landslides, Banff, Canada, 3-8 June 2012, CRC Press.

Hermanns, R., T. Oppikofer, E. Anda, L. Blikra, M. Böhme, H. Bunkholt, G. Crosta, H. Dahle, G. Devoli, L. Fischer, M. Jaboyedoff, S. Loew, S. Sætre and F. X. Yugsi Molina (2012b). "Recommended hazard and risk classification system for large unstable rock slopes in Norway." NGU rapport: **2012.029:** 53.

Hermanns, R. L., T. Oppikofer, M. Böhme, I. M. Penna, P. Nicolet and M. Bredal (2021). "Mapping, hazard and consequence analyses for unstable rock slopes in Norway." Understanding and Reducing Landslide Disaster Risk: Volume 6 Specific Topics in Landslide Science and Applications 5th: 317-323.

Hermanns, R. L., T. F. Redfield and I. M. Penna (2021). Rockslides in the arctic: Why do we care? Fram Forum. Tromsø, Framsenteret Drift AS. **10:** 102-105.

Hermanns, R. L., I. M. Penna, T. Oppikofer, F. Noël and G. Velardi (2022). 5.06 - Rock Avalanche. Treatise on Geomorphology (Second Edition). J. F. Shroder. Oxford, Academic Press**:** 85-105.

Hilger, P., R. L. Hermanns, J. C. Gosse, B. Jacobs, B. Etzelmüller and M. Krautblatter (2018). "Multiple rock-slope failures from Mannen in Romsdal Valley, western Norway, revealed from Quaternary geological mapping and 10Be exposure dating." The Holocene **28**(12): 1841-1854.

Hughes, A. L., R. Gyllencreutz, Ø. S. Lohne, J. Mangerud and J. I. Svendsen (2016). "The last Eurasian ice sheets–a chronological database and time-slice reconstruction, DATED-1." Boreas **45**(1): 1-45.

Hungr, O. and S. G. Evans (1996). Rock avalanche runout prediction using a dynamic model. Landslides. K. Senneset, Balkema, Rotterdam**:** 233-238.

Hungr, O. and S. McDougall (2009). "Two numerical models for landslide dynamic analysis." Computers & Geosciences **35**(5): 978-992.

Hungr, O. and S. G. Evans (2004). "Entrainment of debris in rock avalanches: An analysis of a long run-out mechanism." Geological Society of America Bulletin **116**(9-10): 1240-1252.

Hungr, O., S. Leroueil and L. Picarelli (2014). "The Varnes classification of landslide types, an update." Landslides **11**(2): 167-194.

Jaboyedoff, M., M. Derron, B. Rudaz, T. Oppikofer, I. Penna and S. Daicz (2015). A review of geometrical methods for determination of landslide volume and failure surface geometry. Proceedings of the 68th Canadian Geotechnical Conference GEOQuébec 2015-Challenges from North to South.

Jansen, I. (1986). Kvartærgeologi: jord og landskap i Telemark gjennom 11000 år: beskrivelse til kvartærgeologisk kart i målestokk 1: 250000, Skien: Fylkeskontoret i Telemark.

Lauknes, T. R., J. Grahn, L. Royet, Y. Larsen, M. Böhme, J. F. Dehls and L. Kristiansen (2020). Mapping and characterization of unstable slopes with Sentinel-1 multi-geometry InSAR (activity line 2: public sector applications). NORCE Technology. N. Technology. Tromsø, Norway. **2-2020**.

Lilleøren, K. S., B. Etzelmüller, T. V. Schuler, K. Gisnås and O. Humlum (2012). "The relative age of mountain permafrost—estimation of Holocene permafrost limits in Norway." Global and Planetary Change **92**: 209-223.

Loew, S., D. Hantz and W. Gerber (2021). "Rockfall Causes and Transport Mechanisms-A Review." Reference Module in Earth Systems and Environmental Sciences.

Loke, M. H., 2018. Geoelectrical Imaging 2D & 3D. Instruction Manual. Res2DInv ver 4.08. http://www.geotomosoft.com/.

Mazzanti, P., F. Bozzano, M. Avolio, V. Lupiano and S. D. Gregorio (2010). "3D numerical modelling of submerged and coastal landslide propagation." Submarine Mass Movements and Their Consequences: 127-139.

McDougall, S. and O. Hungr (2004). "A model for the analysis of rapid landslide motion across three-dimensional terrain." Canadian Geotechnical Journal **41**(6): 1084-1097.

McKinnon, M. (2010). Landslide runout: statistical analysis of physical characteristics and model parameters, University of British Columbia.

Nichol, S. L., O. Hungr and S. G. Evans (2002). "Large-scale brittle and ductile toppling of rock slopes." Canadian Geotechnical Journal **39**: 773-788.

Nicolet, P., I. Gunleiksrud, G. Meyer, B. E. Larsen, G. Tassis, R. L. Hermanns, T. Eiken and L. Kristensen (2022). Geologisk modell og fare-og risikoklassifisering av det ustabile fjellpartiet Tussafoten i Eidfjord, Vestland. NGU report. **2022.026:** 96.

Olesen, O., V. C. Baranwal, A. Bjørlykke, M.-A. Dumals, H. Elvebakk, J. Gellein, L. Gernigon, S. Gradmann, C. Haase, B. E. Larsen, T. Lauritsen, H. G. Van der Rueslätten, J. Schönenberger, T. Slagstad, M. Smelror and T. Solbakk (2020). Coop Phase 3 Crustal Onshore-Offshore Project. NGU-rapport. **2019.036:** 651.

Oppikofer, T., A. Saintot, S. Otterå, R. L. Hermanns, E. Anda, H. Dahle and T. Eiken (2013). Investigations on unstable or potential unstable rock slopes in Møre og Romsdal – status and plans after field surveys in 2012. NGU report. **2013.014**: 169.

Oppikofer, T., M. Böhme, P. Nicolet, I. Penna and R. Hermanns (2016). Metodikk for konsekvensanalyse av fjellskred. NGU Report. **2016:** 67.

Oppikofer, T., A. Saintot, R. Hermanns, M. Böhme, T. Scheiber, J. Gosse and G. Dreiås (2017). "From incipient slope instability through slope deformation to catastrophic failure—Different stages of failure development on the Ivasnasen and Vollan rock slopes (western Norway)." Geomorphology **289**: 96-116.

Oppikofer, T., R. L. Hermanns, N. J. Roberts and M. Böhme (2019). "SPLASH: semi-empirical prediction of landslide-generated displacement wave run-up heights." Geological Society, London, Special Publications **477**(1): 353-366.

Øydvin, E., G. Devoli, T. H. Bargel, T. Wiig, A. Taurisano, H. Berg, O. Eikenæs, E. Lyche, T. Fergus, M. R. LKvakland, J. Wasrud, T. E. Helle, K. Ovredal, I. O. OPeerebom, Ø. Anderson, R. L. Hermanns, J. JHøst, L. Hansen, H. Bunkholt, R. Eilertsen, L. Fischer, J.-S. LHeuraux, T. Oppikofer, L. Rubensdotter, K. Sletten, I. L. Solberg and K. Stalsberg (2011). Plan for skredfarekartlegging. Status og prioriteringer innen oversiktskartlegging og detaljert skredfarekartlegging i NVEs regi. NVE rapport **14/2011:** 63.

Penna, I., M. Böhme and R. Hermanns (2017). Dynamic modelling with DAN3D of Stampa scenario 3A. NGU report. **2017:** 16.

Penna, I., P. Nicolet, M. Bredal, M. Böhme, L. Kristensen, G. Pless and T. Eiken (2022). Hazard and risk assessment of the Stiksmoen unstable rock slope in Aurlandfjord (Flåm, Vestland). NGU rapport: **2021.035:** 44.

Pullarello, J. S., M.-H. Derron, M. Jaboyedoff and M. Sturzenegger (2019). Two Matlab routines for rock material propagation modelling: PLANOS, a volume assessment by infinite planar discontinuities, and PrePostDAN3D, a data treatment tool for before and after DAN3D processing. Geophysical Research Abstracts.

Reusch, H. (1907). Skredet i Loen 15de januar 1905. Norges Geologiske Undersøkelse, Aarbok. Oslo. **III:** 3-20.

Reynolds, J. M. (2011). An introduction to applied and environmental geophysics, John Wiley & Sons.

Scheidegger, A. E. (1973). "On the prediction of the reach and velocity of catastrophic landslides." Rock mechanics **5**(4): 231-236.

Schleier, M., R. Hermanns, J. Rohn and J. C. Gosse (2015). "Diagnostic characteristics and paleodynamics of supraglacial rock avalanches, Innerdalen, Western Norway." Geomorphology **245**: 23-39.

Solberg, I., L. Hansen, J. Rønning and E. Dalsegg (2011). Veileder for bruk av resistivitetsmålinger i potensielle kvikkleireområder. NGU rapport. **2010:** 93.

Sollid, J. L. and J. A. Trollvik (1991). Opplandsfylke, kvartærgeologi geomorfologi 1:250 000. Oslo, Universitet av Oslo.

Sosio, R., G. B. Crosta and O. Hungr (2008). "Complete dynamic modeling calibration for the Thurwieser rock avalanche (Italian Central Alps)." Engineering Geology **100**(1-2): 11-26.

Svennevig, K., M. J. Owen, M. Citterio, T. Nielsen, S. Rosing, J. Harff, R. Endler, M. Morlighem and E. Rignot (2023). "Holocene gigascale rock avalanches in Vaigat strait, West Greenland—Implications for geohazard." Geology **52**(2): 147-152.

Tassis, G. and B. E. Larsen (2021). ERT and GPR survey at the Stiksmoen unstable rock slope, Aurland municipality, Vestland. NGU report. **2021.025**: 26.

Vorren, T. and J. Mangerud (2008). "Glaciations come and go." The making of a land-Geology of Norway, Norsk Geologisk Forening, Trondheim: 480-533.

Wyllie, D. C. and C. W. Mah (2004). Rock Slope Engineering: Civil and Mining, Spon Press/Taylor & Francis Group, London and New York.

Lorem et ipsum

6. APPENDIX

6.1 Appendix 1 Plots of dGNSS deformations for each measurement point showing vertical versus horizontal deformation.

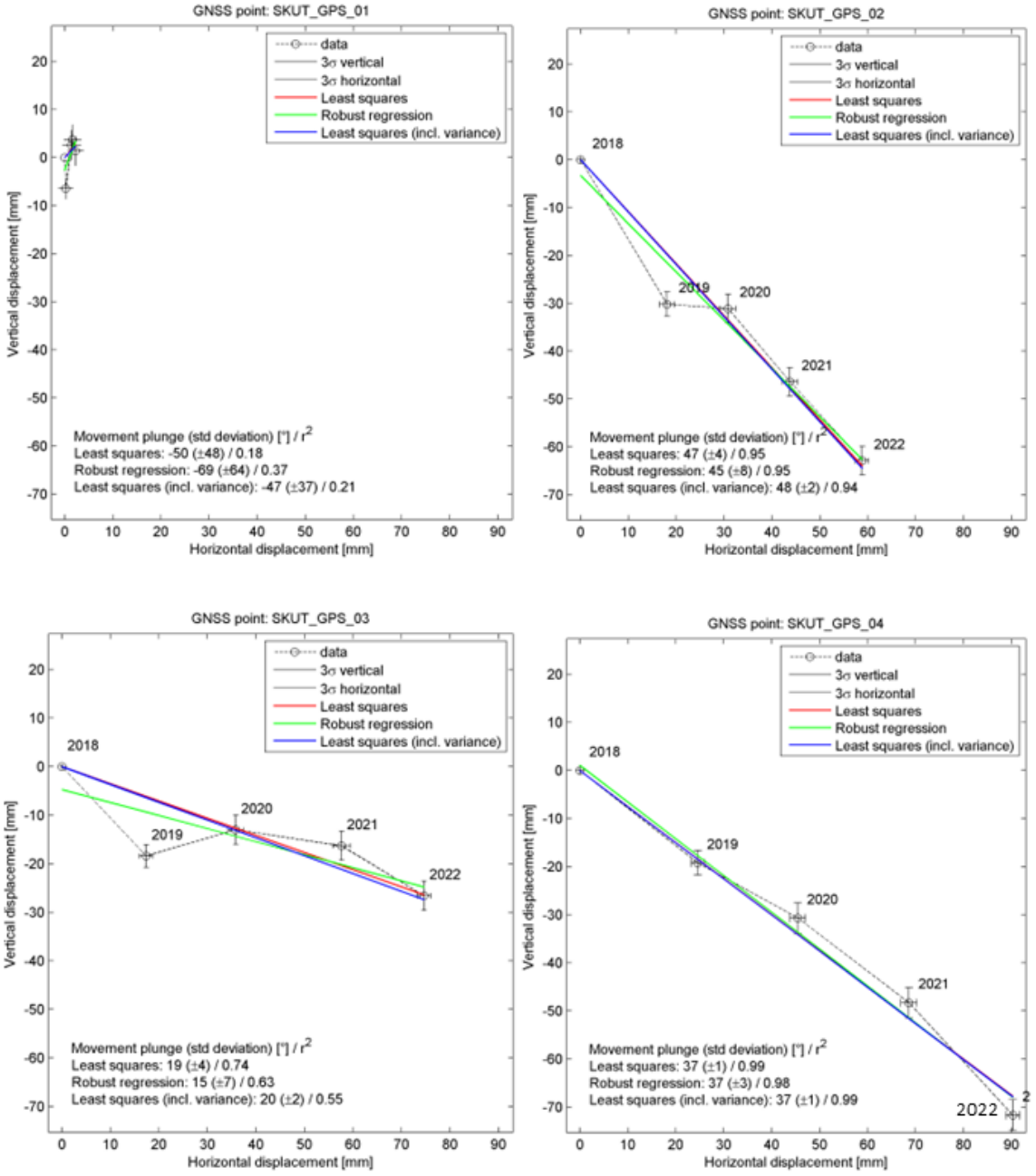

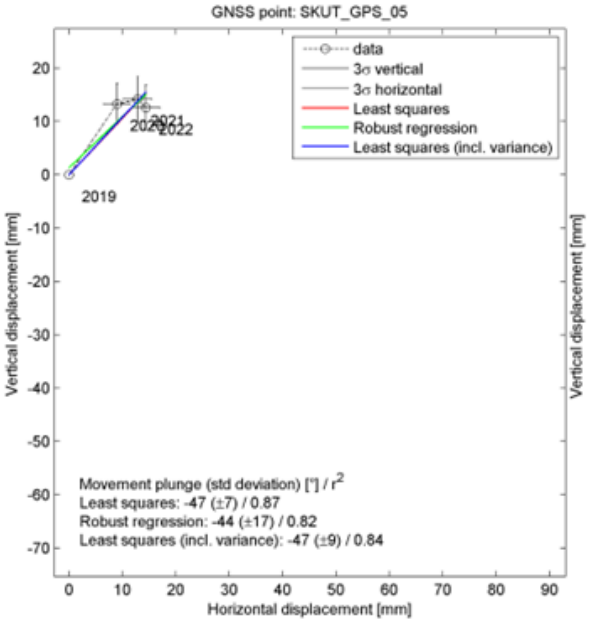
GNSS point: SKUT_GPS_05
data
3σ vertical
3σ horizontal
Least squares
Robust regression
Least squares (incl. variance)
2019
2020
2021
2022
Vertical displacement [mm]
Horizontal displacement [mm]
Movement plunge (std deviation) [°] / r2
Least squares: -47 (±7) / 0.87
Robust regression: -44 (±17) / 0.82
Least squares (incl. variance): -47 (±9) / 0.84

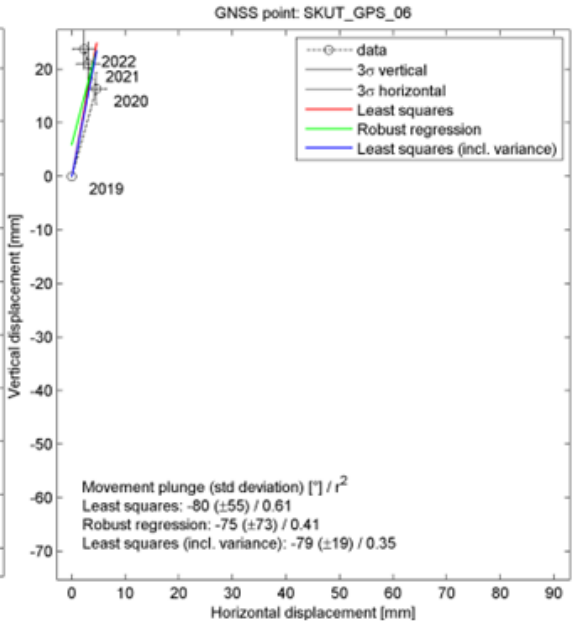
GNSS point: SKUT_GPS_06
data
3σ vertical
3σ horizontal
Least squares
Robust regression
Least squares (incl. variance)
2019
2020
2021
2022
Vertical displacement [mm]
Horizontal displacement [mm]
Movement plunge (std deviation) [°] / r2
Least squares: -80 (±55) / 0.61
Robust regression: -75 (±73) / 0.41
Least squares (incl. variance): -79 (±19) / 0.35

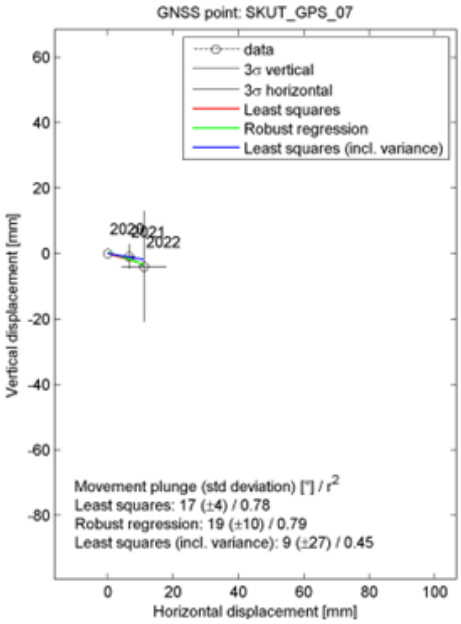
GNSS point: SKUT_GPS_07
data
3σ vertical
3σ horizontal
Least squares
Robust regression
Least squares (incl. variance)
2020
2021
2022
Vertical displacement [mm]
Horizontal displacement [mm]
Movement plunge (std deviation) [°] / r2
Least squares: 17 (±4) / 0.78
Robust regression: 19 (±10) / 0.79
Least squares (incl. variance): 9 (±27) / 0.45

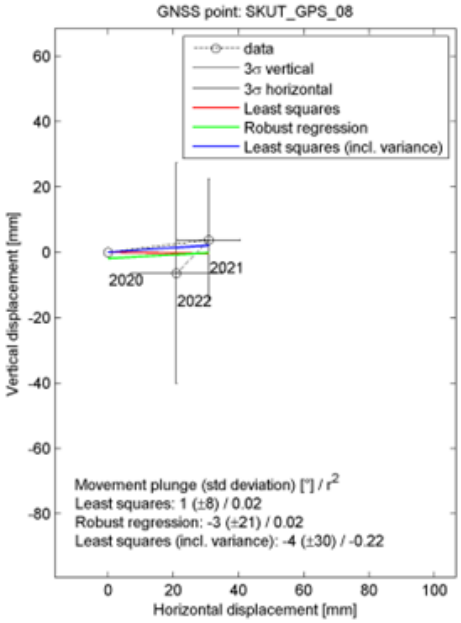
GNSS point: SKUT_GPS_08
data
3σ vertical
3σ horizontal
Least squares
Robust regression
Least squares (incl. variance)
2020
2021
2022
Vertical displacement [mm]
Horizontal displacement [mm]
Movement plunge (std deviation) [°] / r2
Least squares: 1 (±8) / 0.02
Robust regression: -3 (±21) / 0.02
Least squares (incl. variance): -4 (±30) / -0.22

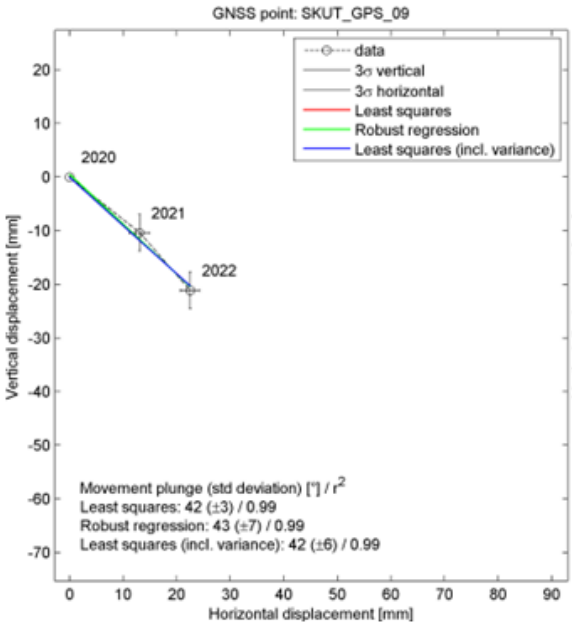
GNSS point: SKUT_GPS_09
data
3σ vertical
3σ horizontal
Least squares
Robust regression
Least squares (incl. variance)
2020
2021
2022
Vertical displacement [mm]
Horizontal displacement [mm]
Movement plunge (std deviation) [°] / r2
Least squares: 42 (±3) / 0.99
Robust regression: 43 (±7) / 0.99
Least squares (incl. variance): 42 (±6) / 0.99

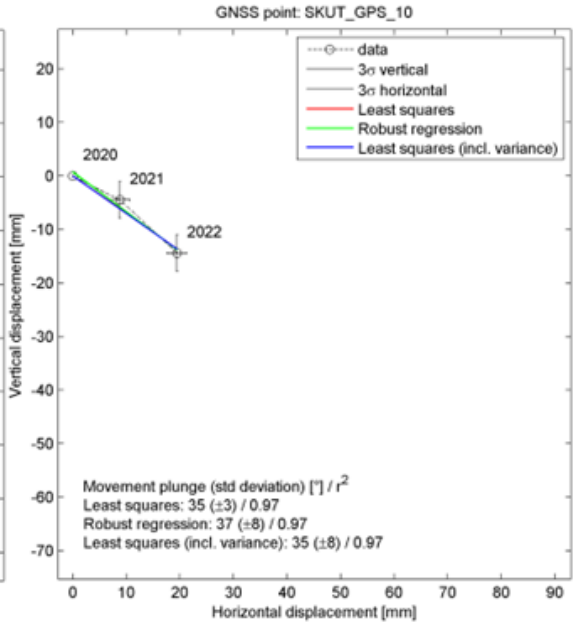
GNSS point: SKUT_GPS_10
data
3σ vertical
3σ horizontal
Least squares
Robust regression
Least squares (incl. variance)
2020
2021
2022
Vertical displacement [mm]
Horizontal displacement [mm]
Movement plunge (std deviation) [°] / r2
Least squares: 35 (±3) / 0.97
Robust regression: 37 (±8) / 0.97
Least squares (incl. variance): 35 (±8) / 0.97

6.2 Appendix 2 Hazard analysis and ranking of parameters considered for the classification.

Scenario A

Fareklasser	Sannsynlighet	Kum. sannsyn.
Meget lav	0.0 %	0.0 %
Lav	0.0 %	0.0 %
Medium	3.8 %	3.8 %
Høy	83.7 %	87.5 %
Meget høy	12.5 %	100.0 %

Farepoeng	
Minimum	6.50
Maksimum	10.25
Modus	8.25
Gjennomsnitt	8.52
5% persentil	7.05
95% persentil	9.75

Tilpasset normalfordeling	
Gjennomsnitt	5.05
Standardavvik	0.93
μ - 2σ	3.19
μ + 2σ	6.90
Korr.-koeff.	0.6869
K-S-test	94.6 %

Criteria (points)	Relative likelyhood					
1. Back scarp (0 / 0.5 / 1)	0	0	1			
2. Potential sliding structure (0 / 0.5 / 1)	1	0	2			
3. Lateral flanks (0 / 0.25 / 0.5 / 0.75 / 1)	0	0	0	0	1	
4. Kinematic analysis (0 / 0.5 / 0.75 / 0.75 / 1)	1	0	0	3	0	
5. Morfological sign of basal failure surface (0 / 0.5 / 1)	0	2	1			
6. Slide velocity (0 / 1 / 2 / 3 / 4 / 5)	0	0	0	1	0	0
7. Acceleartion of velocity (0 / 1)	1	1				
8. Increase in rock fall activity (0 / 1)	0	1				
9. Earlier events (0 / 0.5 / 1)	3	1	0			

Scenario B

Fareklasser	Sannsynlighet	Kum. sannsyn.
Meget lav	0.0 %	0.0 %
Lav	0.0 %	0.0 %
Medium	75.0 %	75.0 %
Høy	25.0 %	100.0 %
Meget høy	0.0 %	100.0 %

Farepoeng	
Minimum	6.50
Maksimum	9.00
Modus	6.50
Gjennomsnitt	7.13
5% persentil	6.50
95% persentil	9.00

Tilpasset normalfordeling	
Gjennomsnitt	5.05
Standardavvik	0.93
μ - 2σ	3.19
μ + 2σ	6.90
Korr.-koeff.	0.8473
K-S-test	90.2 %

Criteria (points)	Relative likelyhood					
1. Back scarp (0 / 0.5 / 1)	0	0	1			
2. Potential sliding structure (0 / 0.5 / 1)	0	0	1			
3. Lateral flanks (0 / 0.25 / 0.5 / 0.75 / 1)	0	0	0	0	1	
4. Kinematic analysis (0 / 0.5 / 0.75 / 0.75 / 1)	0	0	0	0	1	
5. Morfological sign of basal failure surface (0 / 0.5 / 1)	1	0	0			
6. Slide velocity (0 / 1 / 2 / 3 / 4 / 5)	0	3	1	0	0	0
7. Acceleartion of velocity (0 / 1)	1	1				
8. Increase in rock fall activity (0 / 1)	0	1				
9. Earlier events (0 / 0.5 / 1)	0	1	1			

GEOLOGICAL
SURVEY OF
NORWAY

· NGU ·

Geological Survey of Norway
PO Box 6315, Sluppen
N-7491 Trondheim, Norway

Visitor address
Leiv Eirikssons vei 39
7040 Trondheim

Tel (+ 47) 73 90 40 00
E-mail ngu@ngu.no
Web www.ngu.no/en-gb/